AD733752

USAAMRDL TECHNICAL REPORT 71-62

DYNAMIC RESPONSE OF THE OV-1A AIRCRAFT TO SOFT FIELD LANDINGS

By

William T. Alexander

October 1971

EUSTIS DIRECTORATE
U. S. ARMY AIR MOBILITY RESEARCH AND DEVELOPMENT LABORATORY
FORT EUSTIS, VIRGINIA

147

DISCLAIMERS

DISPOSITION INSTRUCTIONS

Unclassified
Security Classification

DOCUMENT CONTROL DATA - R & D

(Security classification of title, body of abstract and indexing annotation must be entered when the overall report is classified)

1. ORIGINATING ACTIVITY *(Corporate author)*	2a. REPORT SECURITY CLASSIFICATION
Eustis Directorate	Unclassified
U.S. Army Air Mobility R&D Laboratory	2b. GROUP
Fort Eustis, Virginia	

3. REPORT TITLE

DYNAMIC RESPONSE OF THE OV-1A AIRCRAFT TO
SOFT FIELD LANDINGS

4. DESCRIPTIVE NOTES *(Type of report and inclusive dates)*
Final Report

5. AUTHOR(S) *(First name, middle initial, last name)*
William T. Alexander

6. REPORT DATE	7a. TOTAL NO. OF PAGES	7b. NO. OF REFS
October 1971	~~146~~ /47	8

8a. CONTRACT OR GRANT NO.	9a. ORIGINATOR'S REPORT NUMBER(S)
b. PROJECT NO.	USAAMRDL Technical Report 71-62
c. Task 1F162204A14602	9b. OTHER REPORT NO(S) *(Any other numbers that may be assigned this report)*
d. House Task 65-28	

10. DISTRIBUTION STATEMENT

Approved for public release; distribution unlimited.

11. SUPPLEMENTARY NOTES	12. SPONSORING MILITARY ACTIVITY
	Eustis Directorate
	U.S. Army Air Mobility R&D Laboratory
	Fort Eustis, Virginia

13. ABSTRACT

This report describes part of a continuing project directed toward the establishment of aircraft design criteria for rough-terrain landing operations.

The report presents the ground loads measured on an instrumented OV-1 airplane during landings on smooth and rough fields. Test results for three landings are compared with the results of dynamic loads computations performed on a digital computer.

The computing program is also used to calculate the loads which would have been obtained by landings and rollouts on the roughest portions of two fields whose contours were measured as part of this project. Failing loads were obtained on one field only.

The equations of motion for the computer program are presented in an appendix. Recommendations are made for future investigations that will improve the analytical procedures.

DD FORM **1473** REPLACES DD FORM 1473, 1 JAN 64, WHICH IS OBSOLETE FOR ARMY USE.

Unclassified
Security Classification

14. KEY WORDS	LINK A		LINK B		LINK C	
	ROLE	WT	ROLE	WT	ROLE	WT
Aircraft						
Loads						
Landing Gear						
Rough Terrain						
Experimental Data						
Theoretical Analysis						

Task 1F162204A14602
House Task 65-28
USAAMRDL Technical Report 71-62
October 1971

DYNAMIC RESPONSE
OF THE OV-1A AIRCRAFT TO
SOFT FIELD LANDINGS

Final Report

By

William T. Alexander

EUSTIS DIRECTORATE
U.S. ARMY AIR MOBILITY
RESEARCH AND DEVELOPMENT LABORATORY
FORT EUSTIS, VIRGINIA

ABSTRACT

A U.S. Army OV-1A Mohawk aircraft was instrumented to measure the loads and attendant stresses incurred during landing and taxiing on unprepared (sod) fields typical of Army operations. Reported herein are the test results and analytical correlation of three landings, one of which resulted in failure of the nose gear and strike damage to the aircraft.

The field effort described is an extension to an earlier investigation conducted in 1964 at the Landing Loads Test Track Facility, Langley Field, Virginia, in which a single OV-1A main gear was subjected to simulated landings. The basis for these investigations has been the refinement of a computerized mathematical model for landing gear developed by the McDonnell-Douglas Aircraft Company of Long Beach, California, which can be used in the establishment of design criteria for aircraft whose mission requires operations in and out of unprepared areas. Results of these efforts have established that the landing gear loads induced by ground roughness can be quite severe and could result in undesirable restrictions and attrition if not properly recognized in the aircraft design.

FOREWORD

The program reported in this document was conducted under the Department of the Army Research and Development Task 1F162204A14602, Rough Terrain Landing Loads. The program was conducted by the Aeromechanics Division of the Eustis Directorate, U.S. Army Air Mobility Research and Development Laboratory. The field tests reported herein were performed during July and August 1967 at Franklin, Virginia.

TABLE OF CONTENTS

LIST OF ILLUSTRATIONS

x

LIST OF TABLES

LIST OF SYMBOLS

A	planform area of rut formed during horizontal movement ΔX, in.^{2}
D	drag load (resistance to forward motion imposed on aircraft by soil), lb
D	drag load on gear (normal to strut), lb
D_B	drag load which exists at full tire deflection, lb
DL	drag load, left main gear, lb
DR	drag load, right main gear, lb
E_A	horizontal kinetic energy subtracted from airplane resulting from application of force D, lb-in.
E_S	energy imparted to soil as a result of soil deformation, lb-in.
F	force, lb
$K_1\ldots, K_n$	proportionality constants
p	footprint pressure of tire on ground, psi
P_o	tire inflation pressure, psi
P_T	force exerted by ground on tire, lb
P_{TB}	force on tire at full tire deflection, lb
$P_{T(FAILURE)}$	force on tire when soil fails, lb
S	strut stroke from fully extended position, in.
S	side load, lb
SL	side load, left gear, lb
SR	side load, right gear, lb

V	vertical load (parallel to strut axis), lb
VL	vertical load, left gear, lb
VR	vertical load, right gear, lb
w	tire width, in.
X	horizontal distance in direction of airplane motion, in.
δ	deflection of oscillograph trace obtained during a test run, in.
δ_S	soil deformation, in.
δ_{SB}	soil deformation under load P_{TB}, in.
Δ	deflection of oscillograph trace during calibration run, in.
μ	coefficient of friction
μ_R	rolling coefficient of friction
μ_S	sliding coefficient of friction

SUBSCRIPTS

A	aft
D	drag
F	forward
S	side
V	vertical

NOTE:	Symbols used in computer program are given in Tables VIII through XIII and in Appendix I.

INTRODUCTION

This report presents the actual measured responses of the OV-1A landing gear and airframe when performing landings on an unprepared soil strip. These data are then compared to analytical findings based on the roughness measured for the particular landing site. Although the program was planned for several landings on a minimum of three different fields, it could not be completed because of the test aircraft crash on the first landing attempt. The study, therefore, had to be limited to the crash landing and two practice landings made prior to the crash.

The report is divided into three sections plus appendixes. Section I, "Instrumentation Report", describes the procedures used in instrumenting, calibrating, and deriving the load equations for the landing gear. Section II, "Field Tests", describes the field measurements and total aircraft instrumentation. Section III, "Computed Loads and Comparison With Test Results", presents the method used in calculating the dynamic loads, discusses correlation of the analytical and measured results, and gives conclusions and results of the findings. The appendixes contain the equations of motions and forces used for the analytical effort and other supporting documents pertinent to the program.

SECTION I. INSTRUMENTATION REPORT

CALIBRATION PROCEDURE FOR STRAIN GAGE LOCATIONS

Stress-cote data and photographs of strain gage locations on the Grumman AO-1 main gear lower piston were used to locate the bonded resistance strain gages on the two main gears of the YOV-1 airplane (Figure 1). The axle area contains twelve strain gages in groups of three oriented in 45-degree rosettes with the center gage parallel with the center line of the axle. Gages were located from stress-cote patterns that indicate a minimum interaction response for a given direction of loading. Rosette gages were located at theoretical positions of maximum shear and maximum bending. All gages on the main gears were connected as one quarter active gages so that individual strain responses could be recorded at every gage location. A typical bridge circuit is illustrated in Figure 2. Gage installation and locations are outlined on Douglas drawing Z7890978.

Strain gages were located on the nose gear axle at the planes of maximum bending moment and configured to provide a four-active-arm bridge that minimizes interactions from loads applied in directions other than the principal direction. Two full bridges for vertical load and two full bridges for drag load were installed. The axle installation is shown in Figure 3.

Selection of Strain Gage Combinations for Main Gears

The two main gears were individually loaded to various single-direction and combined-direction loads. The responses from all of the strain gages were recorded as punch card data and entered with a special computing program. The program selects full or partial bridge channels from various strain gage combinations such that a given channel will give a maximum response to a given load condition. Interaction responses on any channel were considered at a minimum when they were less than 5 percent of the maximized values.

The vertical, drag, and side load channels were identified as LV-1, LV-2, LV-3, LD-1, LD-2, LD-3, LS-1, LS-2 for the left main gear and RV-1, RV-2, RV-3, RD-1, RD-2, RD-3, RS-1, RS-2 for the right main gear. A sample channel wiring diagram is shown in Figure 4. The left main gear miniature cannon connector pin and gage lead are identified in Figure 5.

Static Calibration

The gears were individually loaded again in a static test jig to various single-load and combined-load conditions. A static calibration photograph appears in Figure 6. The responses from each strain gage channel were recorded. These values and input load values were introduced into a second computer program that provided sets of equations for each combination of vertical, drag, and side channels. Eighteen sets of equations were obtained from the eight channels of strain gages. Equations are shown in Tables I and II. Equations for the nose gear were calculated for vertical and drag directions for four strain gage bridges. Four sets of equations are shown in Table III.

Dynamic Calibration

The main landing gears were serviced and instrumented as shown in Figure 7. The transducers were mounted and set up to measure strut position; lower mass vertical, drag, and side accelerations; upper mass vertical acceleration; wheel rpm; and oil and air pressure. Strain gages, transducers, and vertical load and drag load from the reaction platform were recorded on oscillographs during a succession of drops ranging from 6 feet to 27 feet. The data obtained were analyzed and the final gage combinations that were to be read during flight test were selected. A typical drop record is shown in Figure 8.

The nose gear was serviced in the prescribed manner, placed in the drop test jig, and dropped in a succession of drops. Instrumentation recorded during these drops included vertical and drag accelerations, vertical and drag strain gage channels, and vertical and drag reaction platform channels. The data obtained were recorded on oscillographs and analyzed. Figure 9 shows the nose gear drop test setup.

Equations derived from the static calibration were reviewed by applying data from the drop tests. Those bridge combinations showing the best correlation between static calibrations and drop tests were selected as primary and spare combinations to be recorded in the flight test program. The bridge numbers and combinations for the left main gear in order of preference are LV-2, LD-2, LS-2; LV-1, LD-2, LS-2; LV-2, LD-1, LS-2; and LV-2, LD-2, LS-1. The bridge numbers and combinations for the right gear are RV-1, RD-1, RS-1; RV-3, RD-1, RS-1; RV-1, RD-2, RS-1; and RV-1, RD-1, RS-2. The bridge numbers and combinations for the nose gear are NV-1, ND-1; NV-1, ND-2; NV-2, ND-1; and NV-2, ND-2. Load channel curves and final equations are discussed on pages 12 through 15.

INSTRUMENTATION RÉSUMÉ

Strain Gages

Installation - DAC Drawing Z7890978

Calibration equations for main gears are shown in Tables I and II.
Calibration equations for nose gear are shown in Table III. Best sets
are listed in Table VI.

Air Pressure Transducers

Installation - Shown in Figure 10 for right main gear.

Type - CEC 4-313 Pressure Pickup

Serial No. - Left Main Gear - 21222
             Right Main Gear - 20750

Calibration - [shunt type across (+) input and (+) output]
              LMG: 100KΩ = 1054 psi
              RMG: 100KΩ = 1024 psi

Accelerometers

Installation - DAC Sketch #41417, Drawings Z7892350 and Z7892245

Types - Lower Vertical and Drag, All Gears
        Statham A6-100-350 Accelerometer
        Upper Vertical and Lower Side Main Gears
        Statham A5-50-350 Accelerometer

Serial No. - Lower Vertical LMG   - 11455, I-10979
             Lower Vertical RMG   - 11459, I-10982
             Lower Vertical NG   - 11458, I-10981
             Lower Drag LMG   - 11454, I-10978
             Lower Drag RMG   - 11153, I-10977
             Lower Drag NG   - 11452, I-10976
             Lower Side LMG   - 13774, I-10984
             Lower Side RMG   - 13771, I-10987
             Upper Vertical LMG   - 13776, I-10986
             Upper Vertical RMG   - 13775, I-10985

4

Calibration - [100KΩ shunt across (+) input and (+) output]

Lower Vertical LMG	- 20.23 g	(+ Down)
Lower Vertical RMG	- 20.82 g	(+ Down)
Lower Vertical NG	- 19.58 g	(+ Down)
Lower Drag LMG	- 21.15 g	(+ Aft)
Lower Drag RMG	- 20.12 g	(+ Aft)
Lower Drag NG	- 20.14 g	(+ Aft)
Lower Side LMG	- 11.19 g	(+ Outboard)
Lower Side RMG	- 10.81 g	(+ Outboard)
Upper Vertical LMG	- 10.74 g	(+ Down)
Upper Vertical RMG	- 10.22 g	(+ Down)

Oil Pressure Transducers

Installation - DAC Sketch #22888

Type - CEC 4-313 Pressure Pickup

Serial No. - Left Main Gear - 21638
Right Main Gear - 22118

Calibration - [100KΩ shunt across (+) input and (+) output]
LMG - 1064 psi
RMG - 996 psi

RPM Transducer

Installation - Drawing Z7892245

Type - Electro #3055 Magnetic Pickup

Output - Varies depending on distance from pip plate (1 pip/rev)

Strut Deflection (Stroke)

Installation - Drawing Z7892350

Type - Douglas Design Z7892350

Identification - LMG - DI #1
RMG - DI #2
NG - DI #3

Calibration - [100KΩ shunt across (+) input and (+) output] (Figure 11)
         DI #1 - 44. 8 deg = 100K
         DI #2 - 45. 9 deg = 100K
         DI #3 - 44. 9 deg = 100K,

TABLE I. MOHAWK MAIN GEAR CALIBRATION
(LOAD EQUATIONS – RIGHT MAIN GEAR)

Channel Combinations			VR			DR			SR		
RV	RD	RS	K_1	K_2	K_3	K_4	K_5	K_6	K_7	K_8	K_9
1	1	1	16135	-669	-6044	-62	4247	-515	423	-284	5408
1	1	2	14923	-1751	-7519	-166	4154	-653	1478	664	6468
1	2	1	16169	-852	-6148	-315	5981	117	438	-371	5364
1	2	2	14974	-2403	-7791	-297	6002	97	1458	946	6584
1	3	1	16000	-1741	-5269	1259	18612	-9427	366	-728	573
1	3	2	15047	-5233	-4410	-464	12504	-8072	1397	3112	4742
2	1	1	10384	943	-2647	-27	4242	-526	277	-241	5497
2	1	2	10047	405	-3309	-97	4133	-685	977	874	6865
2	2	1	10347	1323	-2520	-197	5939	47	287	-312	-5463
2	2	2	10039	610	-3230	-197	5942	10	955	1235	7003
2	3	1	10607	5050	-5030	785	19029	-9353	259	-534	5718
2	3	2	10023	1188	-4029	-342	12299	-8114	936	3710	4783
3	1	1	-38798	-356	-1310	121	4246	-531	-940	-275	5227
3	1	2	-3804	-630	-1965	383	4142	-702	-3486	768	6929
3	2	1	-38835	-406	-1363	721	5971	26	-974	-355	5489
3	2	2	-38098	-813	-2034	728	5971	-8	-342	1096	7053
3	3	1	-38959	1092	-1946	-3262	18941	-9209	-807	-709	5826
3	3	2	-38136	-431	-1522	910	12360	-808	-3401	3556	4968

Load Equations Based Upon: V- Cal @ 100K-Ohms; D- Cal @ 100K-Ohms; S- Cal @ 100K-Ohms; $(\delta/\Delta)_V$ = Ratio Run/Cal Pip for Gage V-; $(\delta/\Delta)_D$ = Ratio Run/Cal Pip for Gage D-; $(\delta/\Delta)_S$ = Ratio Run/Cal Pip for Gage S-; VR = Vert Load on Wheel lb + Up; DR = Drag Load on Wheel lb + Aft; and SR = Side Load on Wheel lb + Outb'd.

$$VR = K_1(\tfrac{\delta}{\Delta})_V + K_2(\tfrac{\delta}{\Delta})_D + K_3(\tfrac{\delta}{\Delta})_S$$

$$DR = K_4(\tfrac{\delta}{\Delta})_V + K_5(\tfrac{\delta}{\Delta})_D + K_6(\tfrac{\delta}{\Delta})_S$$

$$SR = K_7(\tfrac{\delta}{\Delta})_V + K_8(\tfrac{\delta}{\Delta})_D + K_9(\tfrac{\delta}{\Delta})_S$$

Channel Combinations			VL			DL			SL		
LV	LD	LS	K_1	K_2	K_3	K_4	K_5	K_6	K_7	K_8	K_9
1	1	1	13490	275	-2509	-6024	4729	-1870	11	-158	5506
1	1	2	14112	342	-3136	-5560	4785	-2363	-1351	-278	6742
1	2	1	13854	74	-2378	276	-5166	34	-200	268	5447
1	2	2	14511	-21	-2906	253	-5161	86	-1698	485	6629
1	3	1	13509	1501	-2900	-4637	21237	-7016	-4	-847	5725
1	3	2	14362	1184	-3439	-2596	20765	-8507	-1739	510	6322
2	1	1	16480	-553	364	-7252	5050	-3118	94	-196	5534
2	1	2	16331	-494	218	-6267	5037	-3653	-1668	-150	6402
2	2	1	15643	525	11	377	-5155	83	-201	262	5413
2	2	2	15681	517	-148	353	-5153	91	-1868	422	6325
2	3	1	16945	-4888	1862	-5772	23313	-8606	85	-1084	5816
2	3	2	16203	-3585	1477	-2756	21166	-9237	-2056	1336	5641
3	1	1	24809	488	-2287	-10876	4581	-1948	63	-169	5511
3	1	2	25869	580	-2982	-9975	4636	-2425	-2485	-299	6728
3	2	1	26015	-295	-2061	561	-5174	38	-363	273	5442
3	2	2	27151	-401	-2627	529	-5170	69	-3188	530	6601
3	3	1	25522	1113	-2435	-9107	21904	-7355	54	-941	5757
3	3	2	26812	1231	-3119	-5041	21035	-8640	-3230	479	6290

TABLE II. MOHAWK MAIN GEAR CALIBRATION (LOAD EQUATIONS – LEFT MAIN GEAR)

Load Equations Based Upon: V- Cal @ 100K-Ohms; D- Cal @ 100K-Ohms; S- Cal @ 100K-Ohms; $(\delta/\Delta)_V$ = Ratio Run/Cal Pip for Gage V-; $(\delta/\Delta)_D$ = Ratio Run/Cal Pip for Gage D-; $(\delta/\Delta)_S$ = Ratio Run/Cal Pip for Gage S-; VL = Vert Load on Wheel lb + Up; DL = Drag Load on Wheel lb + Aft; and SL = Side Load on Wheel lb + Outb'd.

$$VL = K_1\left(\frac{\delta}{\Delta}\right)_V + K_2\left(\frac{\delta}{\Delta}\right)_D + K_3\left(\frac{\delta}{\Delta}\right)_S$$

$$DL = K_4\left(\frac{\delta}{\Delta}\right)_V + K_5\left(\frac{\delta}{\Delta}\right)_D + K_6\left(\frac{\delta}{\Delta}\right)_S$$

$$SL = K_7\left(\frac{\delta}{\Delta}\right)_V + K_8\left(\frac{\delta}{\Delta}\right)_D + K_9\left(\frac{\delta}{\Delta}\right)_S$$

TABLE III.   EQUATIONS FOR YOV-1 MOHAWK NOSE GEAR

Gage NV1, ND1

Drag Fwd:

$$F_V = 1,612V - 537D$$
$$F_{DF} = -198.2V - 1,536D$$

Drag Aft:

$$F_V = 1,666V + 120.7D$$
$$F_{DA} = -137.4V - 1,073D$$

Gage NV1, ND2

Drag Fwd:

$$F_V = 1,609V - 399.5D_S$$
$$F_{DF} = -209.1V - 1,534D_S$$

Drag Aft:

$$F_V = 1,667V + 121.1D_S$$
$$F_{DA} = -145.6V - 1,076D_S$$

Gage NV2, ND1

Drag Fwd:

$$F_V = 1,620V_S - 422.3D$$
$$F_{DF} = -199.3V_S - 1,553D$$

Drag Aft:

$$F_V = 1,741V_S + 197.1D$$
$$F_{DA} = -143.6V_S - 1,079D$$

Gage NV2, ND2

Drag Fwd:

$$F_V = 1,617V_S - 421.8D_S$$
$$F_{DF} = -210.3V_S - 1,531D_S$$

Drag Aft:

$$F_V = 1,742V_S + 197.8D_S$$
$$F_{DA} = -152.2V_S - 1,083D_S$$

Use of the Gear Strut Position Transducers

These devices provide an output proportional to the scissors angle of the torque links. Three devices were installed on the landing gears of the YOV-1 Mohawk airplane used in the Rough Terrain Landing Loads Program. The extension of the landing gears is a sinusoidal function of the scissors angle. The equations defining these relationships are as follows:

$$X_i = 2h \sin \frac{\alpha_i}{2} \tag{1}$$

$$X_0 = 2h \sin \frac{\alpha_0}{2} \tag{2}$$

$$\alpha_i - \alpha_0 = \beta \tag{3}$$

$$RR = \frac{\delta_i - \delta_0}{\Delta}, \quad \delta_0 = 0 \text{ for } X_0 \tag{4}$$

$$\beta = K (RR) \tag{5}$$

where

X_i distance between torque link pivot points

X_0 referenced distance of X for zero record

h length of torque link apex to pivot point

α_i included angle between links (scissors angle)

α_0 included angle at distance X_0

β excursion angle from reference position

RR response ratio

δ_i o'graph deflection for galvo from zero reference position

Δ o'graph deflection for 100KΩ shunt

K degrees rotation for 100KΩ shunt

From (1),
$$\alpha_i = 2 \sin^{-1} \frac{X_i}{2h} \tag{1a}$$

9

From (2),
$$\alpha_0 = 2 \, \text{Sin}^{-1} \frac{X_0}{2h} \tag{2a}$$

From (1a), (2a), (3), and (5),

$$2 \left(\text{Sin}^{-1} \frac{X_i}{2h} - \text{Sin}^{-1} \frac{X_0}{2h} \right) = K(RR) \tag{6}$$

where   RR at α_0 and X_0 (from Zero record) = 0

Solving for X_i,

$$\text{Sin}^{-1} \frac{X_i}{2h} = \frac{K(RR)}{2} + \text{Sin}^{-1} \frac{X_0}{2h} \tag{7}$$

$$X_i = 2h \, \text{Sin} \left[\frac{K(RR)}{2} + \text{Sin}^{-1} \frac{X_0}{2h} \right] \tag{7a}$$

Therefore, any strut position can be determined from the output of these transducers.

Example (verification calibration made at Edwards Air Force Base)

$2h = 20.376$, $\frac{1}{2h} = 0.04908$, $100K\Omega = 96$ counts

K (LMG, DI #1) = 44.8 deg/100KΩ

Measure zero position of left main strut, $X_0 = 19.094$ in.

Calculate $\frac{\alpha_0}{2}$ for X_0, $\frac{\alpha_0}{2} = 69.6$ deg

Apply δ_i readings from oscillograph traces to equations.

					Calculated	Verification
δ_0	= 0					
δ_1	= -215	RR 1	= -2.23	X1 =	6.85 in.	6.900 in.
δ_2	= -133	RR 2	= -1.38	X2 =	12.73 in.	12.880 in.
δ_3	= -248	RR 3	= -2.58	X3 =	4.16 in.	4.18 in.

Constants

2h (main gears) = 20.376 in. K_1 (DI #1, LMG) = 44.8 deg/100K
2h (nose gears) = 16.376 in. K_2 (DI #2, RMG) = 45.9 deg/100K
                               K_3 (DI #3, NG) = 44.9 deg/100K

10

STRUT SERVICE

The landing gear was completely assembled and installed in the drop test jig. The strut was fully extended and filled with hydraulic oil (MIL-O-5606) through the strut upper port via a transparent tube leading from an oil container hung above the landing gear jig. The strut was then fully compressed by lowering the drop test jig, causing the excess oil to flow back into the oil container. This procedure was repeated until it was observed through the transparent tube that no air was trapped in the oil flow.

With the strut fully compressed, the oil line was disconnected and the air pressure fitting was installed in the strut upper port and closed. The drop test jig was then raised to allow the wheel to clear the ground by at least 15 inches. The strut was then inflated with nitrogen, causing the piston to fully extend.

Before each series of drops, both tire and strut pressures were checked for the following pressure readings. Similar servicing technique and pressures were applied to the gears in the static calibration jig.

Main Gear Strut Pressure - 100 psi
Main Gear Tire Pressure - 90 psi
Nose Gear Strut Pressure - 75 psi
Nose Gear Tire Pressure - 65 psi

Maximum Calibration Loads (Static Calibration), Main Gears

The maximum loads were obtained from the strength envelope and are listed in Table IV.

TABLE IV. MAXIMUM CALIBRATION LOADS, MAIN GEARS				
Load Direction	Load Sign	Ultimate Load (lb)	Limit Load (lb)	Static Calibration Load (Used) (lb)
Vertical	+	37,000	24,667	20,000
Drag Aft	+	8,000	5 333	5,000
Drag Fwd	-	19,500	1 ,000	5,000
Side Outbd	+	6,920	4,613	4,000
Side Inbd	-	10,200	6,800	4,000

11

Strut Extension (Static Calibration)

In all the static calibrations, the strut was extended 2 inches from the fully compressed position.

Maximum Calibration Loads (Static Calibration), Nose Gear

Loads were provided from the strength envelope and are listed in Table V.

TABLE V. MAXIMUM CALIBRATION LOADS, NOSE GEAR				
Load Direction	Load Sign	Ultimate Load (lb)	Limit Load (lb)	Static Calibration Load (Used) (lb)
Vertical	+	30,300	20,200	16,000
Drag Aft	+	12,600	8,400	4,000
Drag Fwd	-	7,000	4,670	4,000

Strut Extension (Static Calibration)

The strut was extended 2 inches from the fully compressed position.

LOAD CHANNEL CURVES (Figures 12, 13, and 14)

General

The curves show the axle loads obtained during drop tests of the landing gears. During these drops, the wheels were spun up to simulate landing speeds as follows:

    Right main gear, 47 kn
    Left main gear, 95 kn
    Nose gear, 50 kn

The accuracy of the gear instrumentation can be measured by comparing the loads obtained from separated gage combinations on the same gear, by comparing the loads obtained from gages on one main gear with the loads obtained on the other, and, for vertical loads, by comparing the

gear instrumentation with the drop test platform response. When comparing one main gear load to the other, allowance must be made for the differences in spin-up speed that will affect the drag load appreciably and the vertical and side loads to a minor extent.

Three channels were provided on each main gear for measuring predominantly vertical and drag loads. Two channels were provided on each main gear for measuring side load and two were provided on the nose gear for measuring both vertical and drag loads. Each channel, while responding predominantly to load in one direction, responds to loads in other directions to a lesser extent. Thus, each channel on the main gear has three calibration constants and each channel on the nose gear has two. The main gear loads are obtained from the matrix

$$V = K_1(\tfrac{\delta}{\Delta})_V + K_2(\tfrac{\delta}{\Delta})_D + K_3(\tfrac{\delta}{\Delta})_S$$

$$D = K_4(\tfrac{\delta}{\Delta})_V + K_5(\tfrac{\delta}{\Delta})_D + K_6(\tfrac{\delta}{\Delta})_S$$

$$S = K_7(\tfrac{\delta}{\Delta})_V + K_8(\tfrac{\delta}{\Delta})_D + K_9(\tfrac{\delta}{\Delta})_S$$

where $(\delta/\Delta)_V, \;_D, \;_S$ are the responses of channels measuring predominantly vertical, drag, and side loads and K_1 to K_9 are the aforementioned calibration constants. Since there are 3 channels each producing $(\delta/\Delta)_V$, 3 producing $(\delta/\Delta)_D$, and 2 producing $(\delta/\Delta)_S$, there are 18 ways of obtaining V, D, and S. The comparisons presented were made using the channels which had the least interaction. Other channels could be used in an emergency.

In the nose gear there is merely a 2x2 matrix; hence, four combinations are available, half of which are presented.

Right Main Gear (see Figure 12)

Vertical load: The four channel combinations show a variation of ±7-1/2% from the mean at the peak load. The waves in the platform load are considered platform dynamics and should be ignored. The mean load obtained from gear instrumentation is less than the platform load, but by comparison with the left gear, the gear instrumentation is considered to be more accurate.

Drag load: All combinations read nearly the same. This is considered to be excellent.

13

Side load: Combinations 1, 2, and 3 are in good agreement. Combination 4 is not bad until a vertical load of 12,500 pounds is reached (0.045 set), at which time it deviates considerably. Side load instrumentation in the past has been notably unreliable. In spite of the discrepancies shown here, this was the best side instrumentation obtained to date.

Left Main Gear (see Figure 13)

Vertical load: Accuracy is excellent.

Drag load: Combinations 1, 2, and 4 are good. Combination 3 gives good maximum load but poor shape. Comparison with the right gear indicates that the shape of 1, 2, and 4 is correct.

Side load: Combinations 1, 2, and 3 agree well. Combination 4 is no good. The comment on right gear side load instrumentation is applicable.

Generally, the side load instrumentation will go bad when the vertical load is high because the tire becomes fully compressed and the vertical load is carried largely by one wheel flange. This affects the side reading as noted in the matrix (page 13).

Nose Gear (see Figure 14)

Both vertical and drag instrumentation are considered excellent. The difference between platform reading and strain gage reading is considered to be caused by poor dynamic response of the platform (see Figure 9c). The quality of the nose gear instrumentation shows the advantage of instrumenting a gear with a symmetrical fork.

Table VI lists the best combinations of channels and the corresponding recommended calibration constants.

14

TABLE VI.	BEST CHANNEL COMBINATIONS AND RECOMMENDED CALIBRATION CONSTANTS		
LMG	V_2 D_2 S_2		+ up, aft, RIGHT
V =	$+ 15681. (\delta/\Delta)_V$	$+ 517. (\delta/\Delta)_D$	$- 148. (\delta/\Delta)_S$
D =	$+ 353. (\delta/\Delta)_V$	$- 5153. (\delta/\Delta)_D$	$+ 91. (\delta/\Delta)_S$
S =	$+ 1868. (\delta/\Delta)_V$	$- 422. (\delta/\Delta)_D$	$- 6325. (\delta/\Delta)_S$
RMG	V_1 D_1 S_1		
V =	$+ 16135. (\delta/\Delta)_V$	$- 669. (\delta/\Delta)_D$	$- 6044. (\delta/\Delta)_S$
D =	$- 62. (\delta/\Delta)_V$	$+ 4247. (\delta/\Delta)_D$	$- 515. (\delta/\Delta)_S$
S =	$+ 423. (\delta/\Delta)_V$	$- 284. (\delta/\Delta)_D$	$+ 5408. (\delta/\Delta)_S$
NG	V_1 D_1		
V =	$1666. (\delta/\Delta)_V$	$+ 121. (\delta/\Delta)_D$	
D =	$- 137. (\delta/\Delta)_V$	$- 1073. (\delta/\Delta)_D$	

The Douglas instrumentation drawings are listed in Table VII.

TABLE VII. DOUGLAS INSTRUMENTATION DRAWINGS	
Drawing Number	Title
14245	Oil Pressure Pick Up Housing Plug
14250	Oil Pressure Pick Up Plug Safety Strap
14255	Air Pressure Outlet Adapter
14257	Side Wheel Tire - Drop Carriage
14258	Center Wheel Tire - Drop Carriage
14264	Air Pressure Pick Up Adapter
14268	Wheel Spacer
14269	Wheel Grease Seal
14281	Air Pressure Pick Up Tee
14284	Air Bucket Plate Lugs - Spin Up
14285	Stroke Transducer Lower Attach Bracket - Drop Test
14286	Stroke Transducer Attach Bracket - Drop Test
14287	Stroke Transducer Attach Bracket - Drop Test
14288	Stroke Transducer Attach Bracket Spacers - Drop Test
14291	Dummy Brake Keys
22885	Strut Side Brace Support Jig
22886	Metering Pin Support - Oil Press. Pick Up Rework
22887	Oil Pressure Pick Up Housing
22888	Oil Pressure Pick Up Installation
22900	Side Brace - Upper End Fitting
22901	Side Brace - Lower End Fitting
22904	Dummy Tire
22908	Side Load Pull-Off Fixture
22909	Lower Mass -Vertical & Drag Accelerometer Housing
31393	Drop Test Column Installation
31431	Gear Installation in Drop Test Columns
31432	Main Strut Support Jig
41350	Drop Test Column Details
41361	Small Drop Test Carriage
41404	Dummy Side Brace Assembly
41417	Lower Mass Accelerometer Installation
41424	Drag Load Pull-Off Fixture
41431	Air Bucket Plate - Spin-Up
41432	Stroke Transducer Installation - Drop Test
Z7825491	YOV-1 Mohawk Landing Gear Calibration
Z7890978	Strain Gage Installations

TABLE VII. Continued	
Drawing Number	Title
Z7892345	Phase II - Static Calibration
Z7892350	Phase III - Drop Tests
Z5891061	YOV-1 Mohawk Landing Gear Calibration Jig
Z4891069	Grooved Aluminum Plate
Z4891070	Mounting Bracket
Z4892273	Dummy Tire - Main Gear
Z4891071	Support Jig
Z4891072	Rework of Support Jig
Z4892203	Dummy Drag Brace

The YOV-1 Mohawk landing gear drawings are listed in Table VIII.

TABLE VIII. YOV-1 MOHAWK LANDING GEAR DRAWINGS	
Drawing Number	Title
Bendix Co.	
MAIN GEAR	
172315	Shock Strut Assembly
172481	Piston (Machining)
172493	Adapter - Upper Bearing
172496	Bearing - Lower
172601	Valve - Snubber
172602	Bearing - Upper
172605	Tube - Orifice Support
172608	Fitting - Lower End
173487	Orifice
173545	Cylinder - Outer
NOSE GEAR	
172759	Tube - Orifice
172762	Fitting - Orifice
172763	Pin - Lock
172764	Ring - Piston
173483	Orifice
172768	Cam - Lower
172769	Key
172771	Bearing

TABLE VIII. Continued	
Drawing Number	Title
Bendix Co.	
NOSE GEAR (contd)	
172748	Piston
172757	Bearing - Upper
172752	Cam - Upper
172754	Valve - Snubber
172755	Adapter - Upper
Grumman Co.	
MAIN GEAR	
134L10001, Sheet 1	Main Gear Installation
134L10001, Sheet 2	Main Gear Installation
134PD10011	General Arrangement - Alighting Gear
134PD10014	Main Gear Geometry
NOSE GEAR	
134L10002, Sheet 1	Nose Gear Installation
134L10002, Sheet 2	Nose Gear Installation
134PD10013	Geometry (Proposed) Alighting Gear - Nose Gear
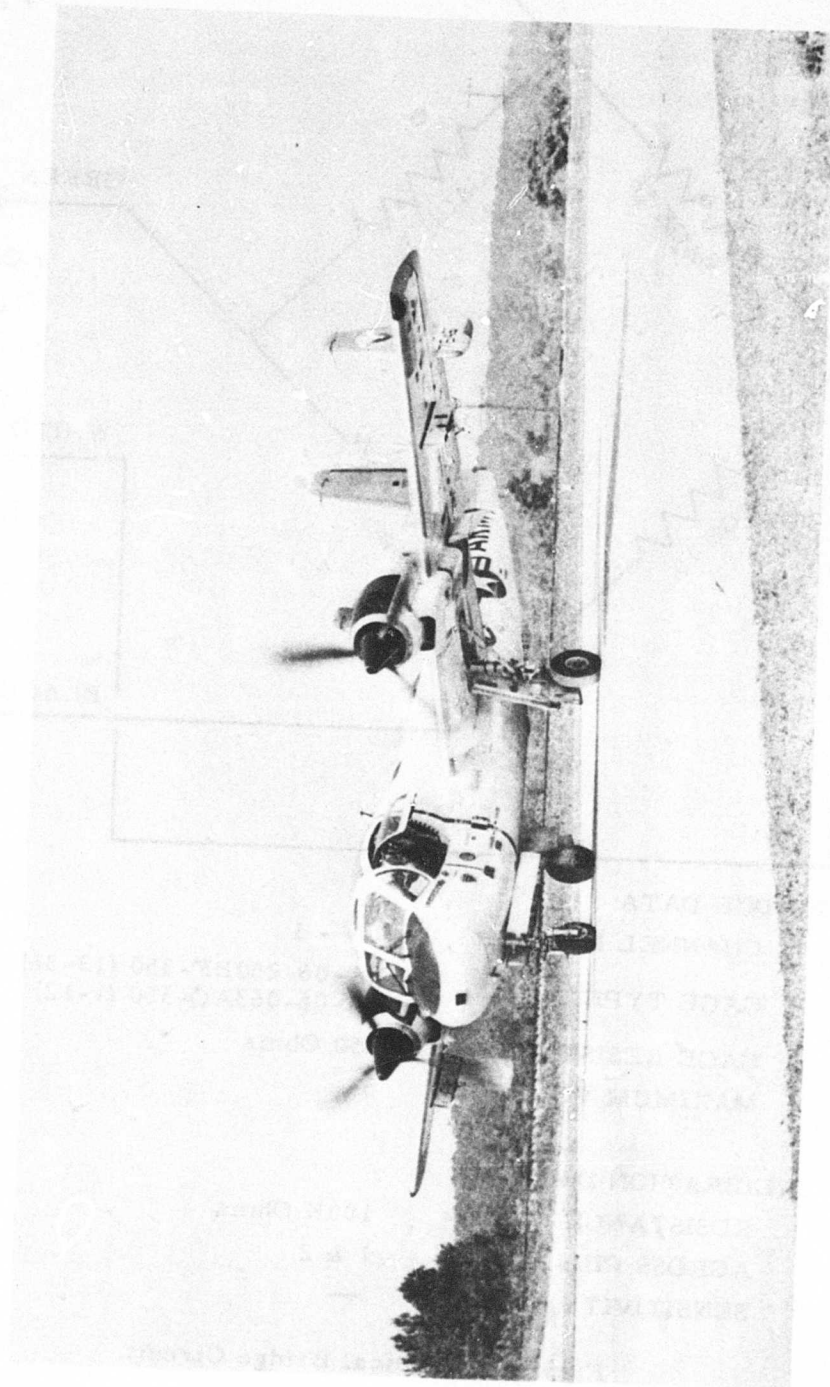
Figure 1. OV-1A Test Aircraft.

19

RED ① + INPUT

GAGE 16   GAGE 3

GREEN ② + OUTPUT

GAGE 10   GAGE 35

WHITE ③ - OUTPUT

BLACK ④ - INPUT
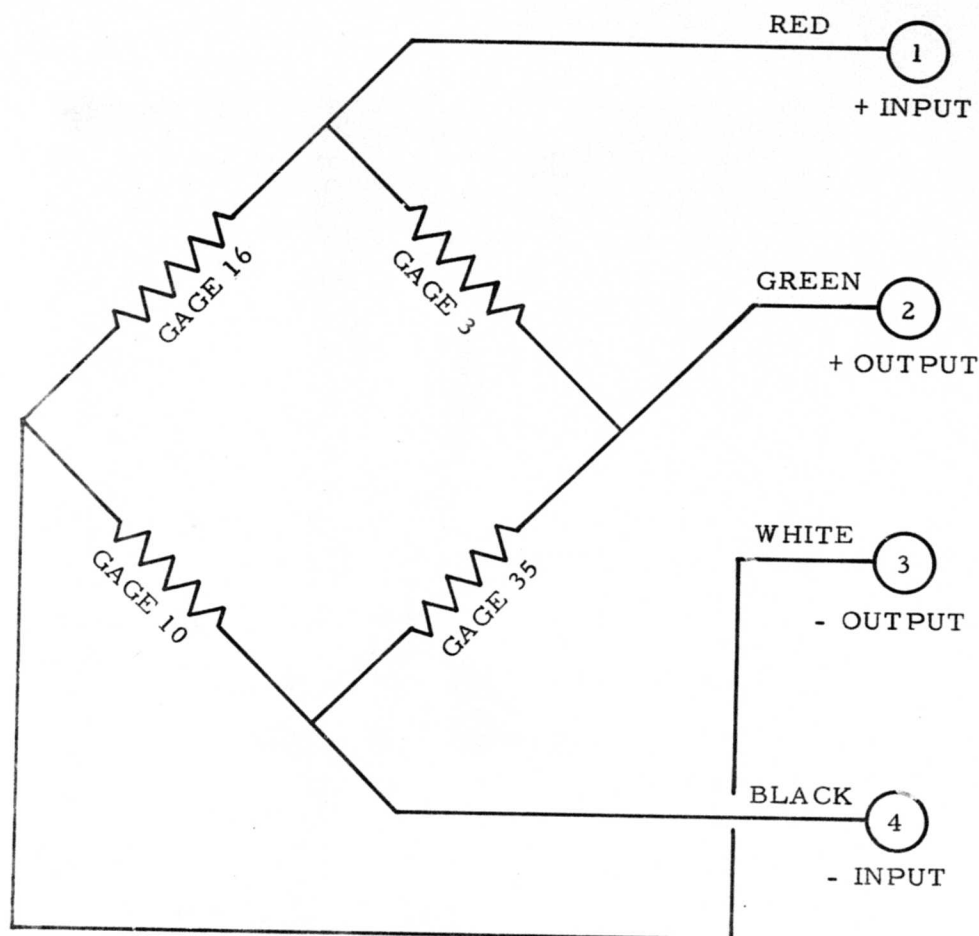
BRIDGE DATA

    CHANNEL NUMBER   LV - 1

    GAGE TYPE   SA-06-250BF-350 (13-36)
                               SA-06-063A⌀-350 (1-12)

    GAGE RESISTANCE   350 Ohms

    MAXIMUM VOLTAGE   5

CALIBRATION DATA

    RESISTANCE   =   100K Ohms

    ACROSS PINS   1 & 2

    SENSITIVITY   —

Figure 2. Typical Bridge Circuit.

20
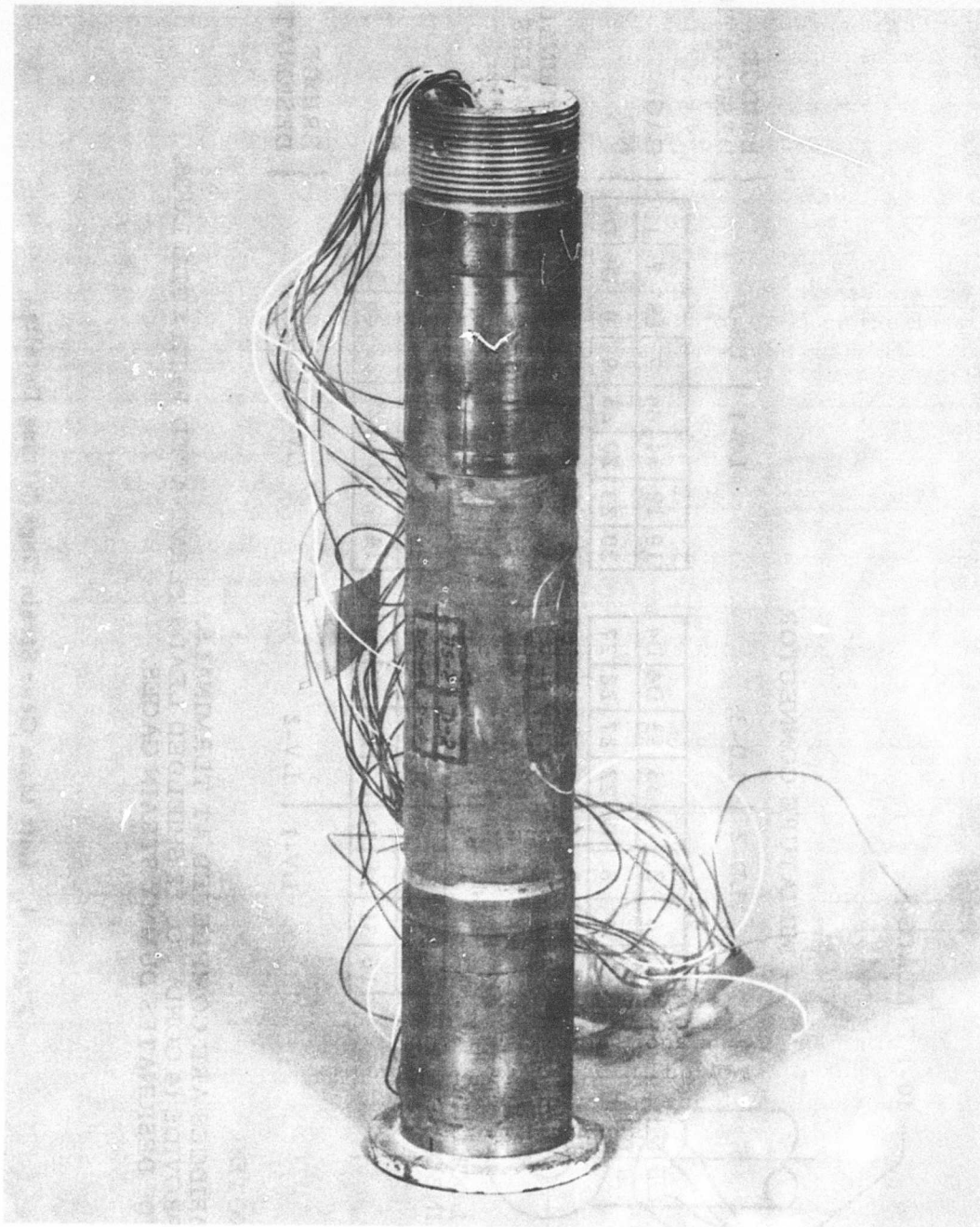
Figure 3. Strain Gage Installation - Nose Gear Axle.

LEADS

MINIATURE CONNECTOR

LOOKING INBOARD

Bridge wiring tables:

BRIDGE DESIGNATION	LS-1				LS-2			
GAGE NO.	19	19	34	34	7	18	7	18
	20	23	20	23	9	9	D5	D5
TERMINAL NUMBERS "T"	1	2	3	4	1	2	3	4

	LV-3				LD-1			
TERMINAL NUMBERS "T"	1	2	3	4	1	2	3	4
GAGE NO.	30	30	D3	D3	5	12	5	12
	14	29	14	29	26	26	25	25
BRIDGE DESIGNATION								

BRIDGE DESIGNATION	LD-2				LD-3			
GAGE NO.	2	6			33	33	D4	D4
	4	8			22	27	22	27
TERMINAL NUMBERS "T"	1	2	3	4	1	2	3	4

	LV-1				LV-2			
TERMINAL NUMBERS "T"	1	2	3	4	1	2	3	4
GAGE NO.	3	10	21	21	28	28		
	16	31	D2	D1	D2	D1		
BRIDGE DESIGNATION								

NOTE:

BRIDGES ARE COMPLETED AT TERMINALS.
PROVIDE (4 COND) NO. 22 SHIELDED LEADS TERMINATED WITH FULL LUGS.
"D" DESIGNATES DUMMY STRAIN GAGES.

Figure 4.   Left Main Gear Strain Gage Wiring Details.

22

WIRE TO TERMINALS
SHOWN ON PAGE 22

GAGES
FROM
AXLE
AREA

2
3
4
5
6
7
8
9
10

SPARES

1

11

12

LD2-T1
LD2-T3
LV1-T1
LV1-T2
LD2-T1
LD2-T2
LD1-T1
LD1-T3
LD2-T2
LD2-T4
LS2-T1
LS2-T3
LD2-T3
LD?-T4
LS2-T1
LS2-T2
LV1-T3
LV1-T4
LD1-T2
LD1-T4

2
3
4
5
6
7
8
9
10
12

FACE VIEWS OF
CONNECTOR
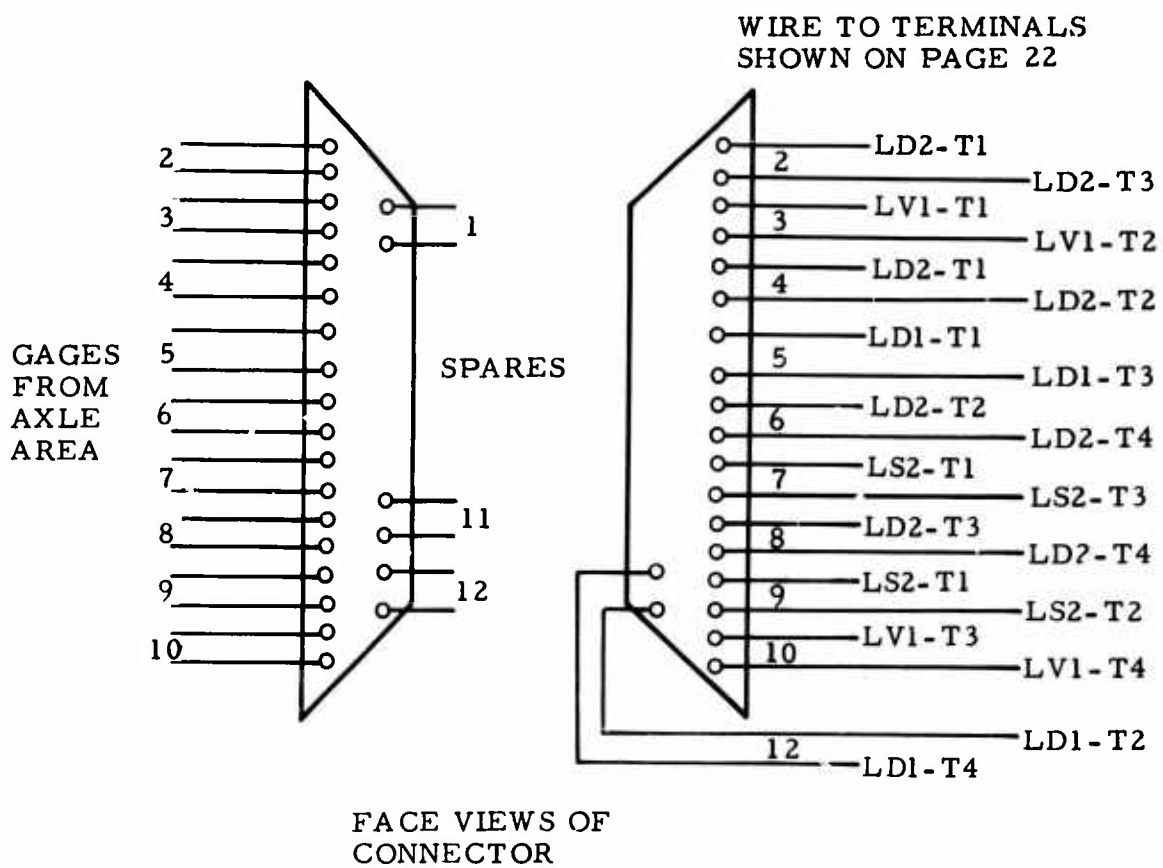
NOTE:

CONNECTOR IS REQUIRED TO PERMIT BRAKE CHANGES.

Figure 5.   Left Main Gear Miniature Cannon Connector Wiring.

23
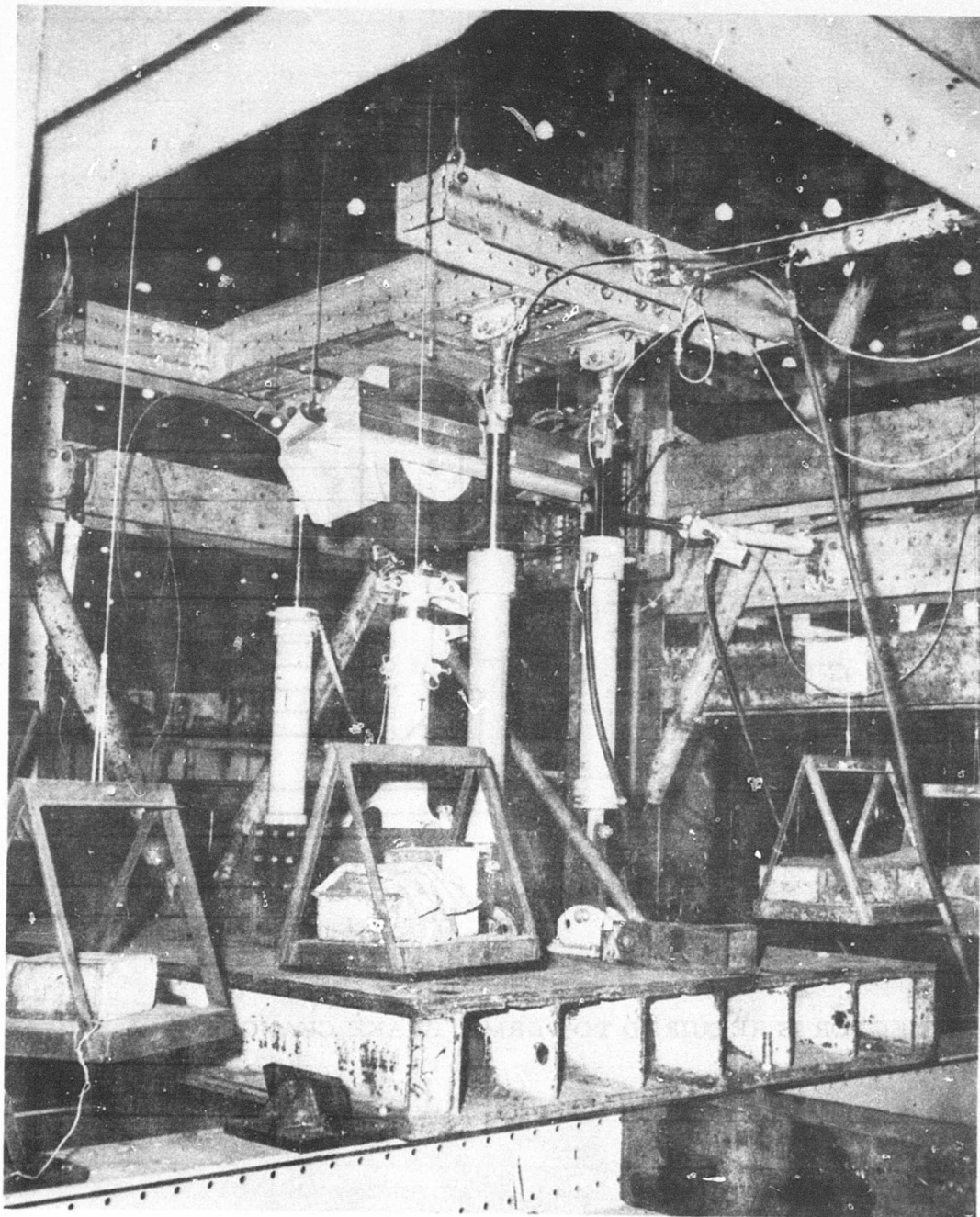
Figure 6.   Static Calibration - Main Gears.

24
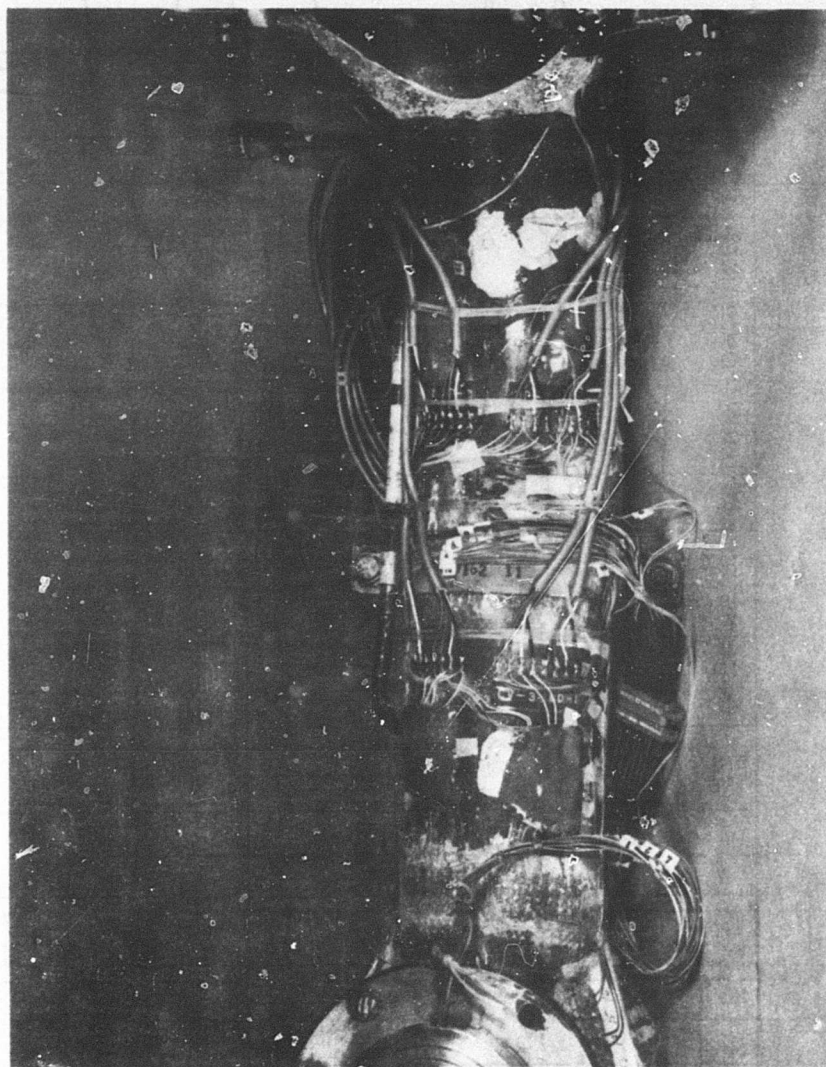
Figure 7. Strain Gage Installation - Main Gears.
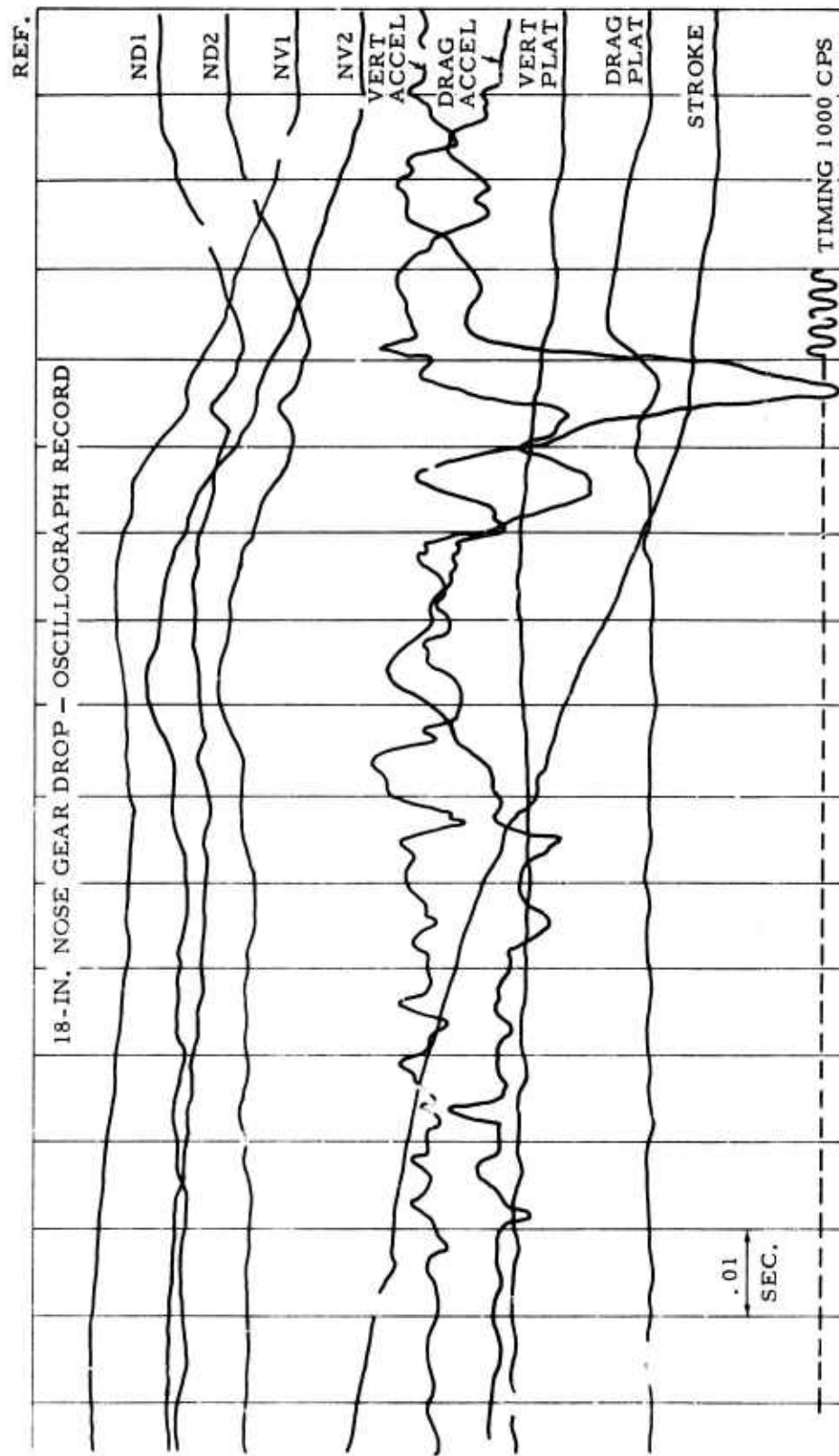
Figure 8. Typical Drop Record.

26
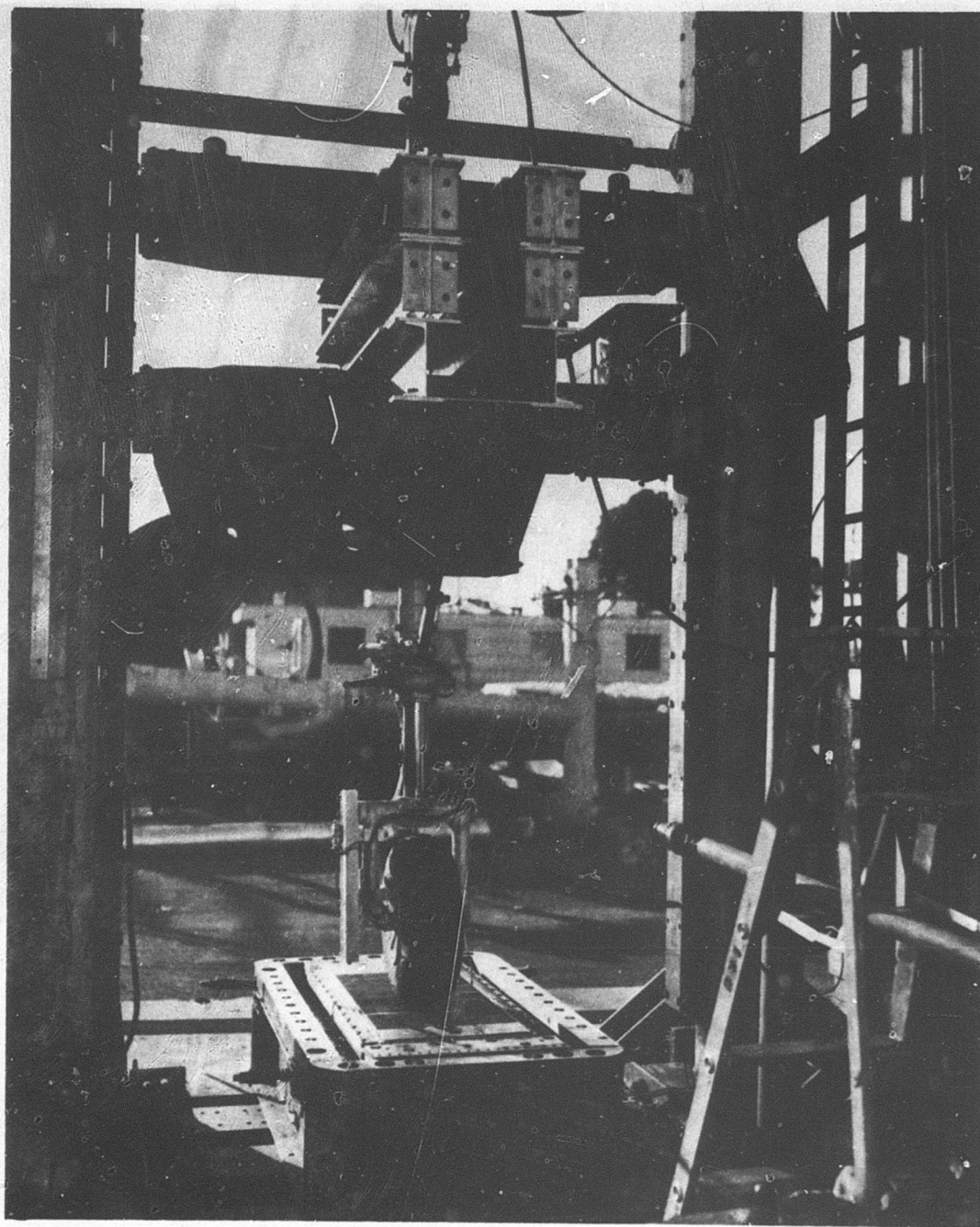
Figure 9.   Drop Test Setup - Nose Gear.

27
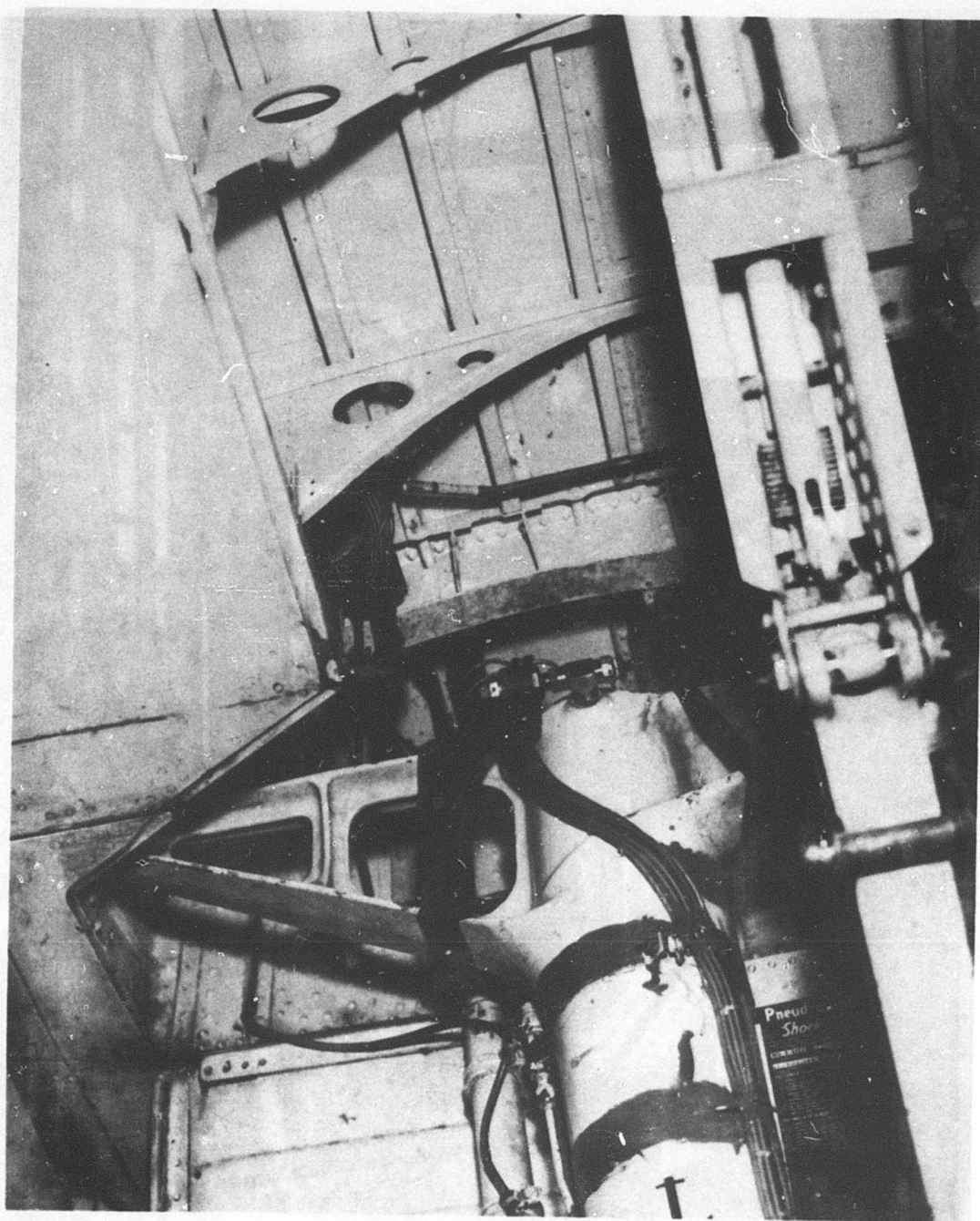
Figure 10. Air Pressure Pickup Installation.
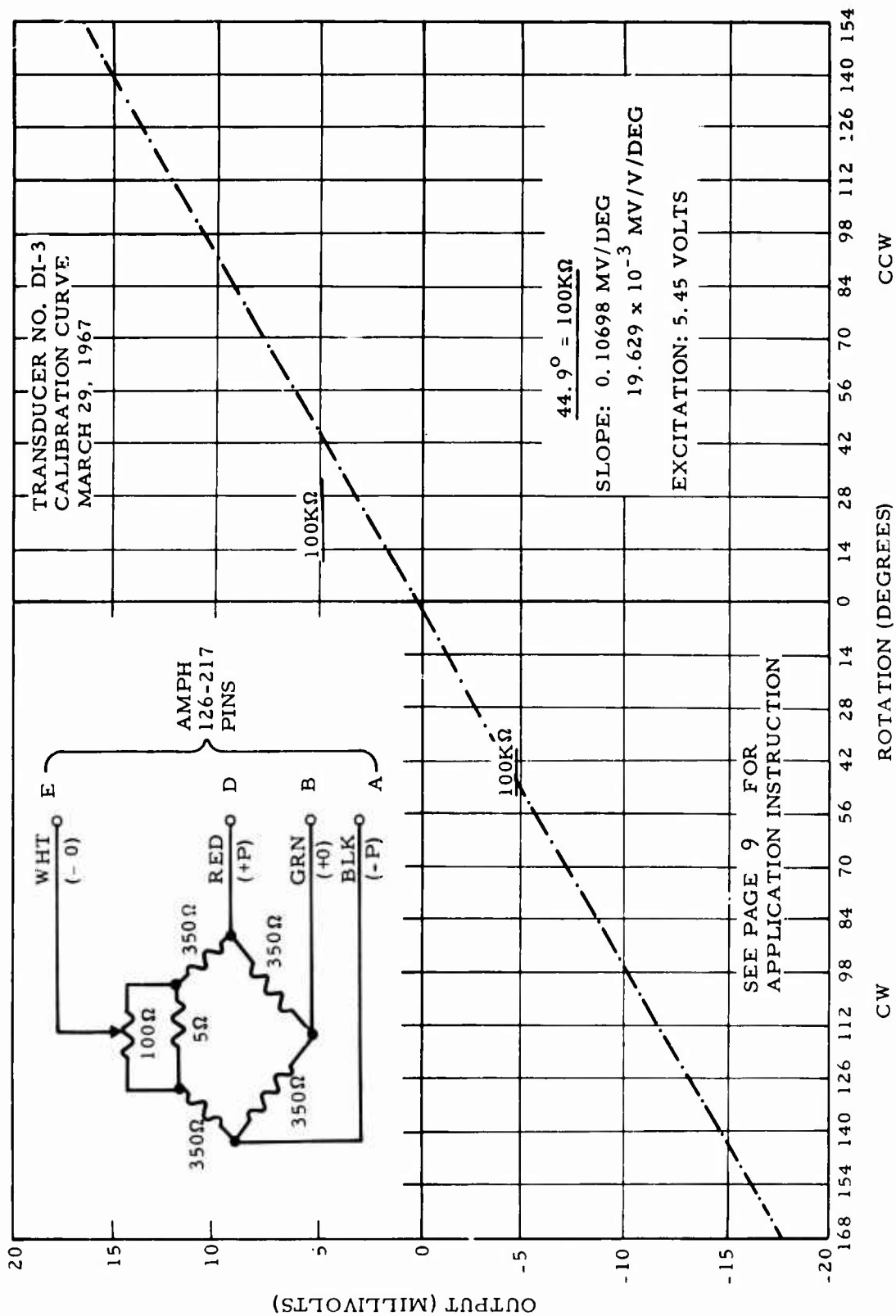
Figure 11. Strut Position Transducer Calibration Curve.

29
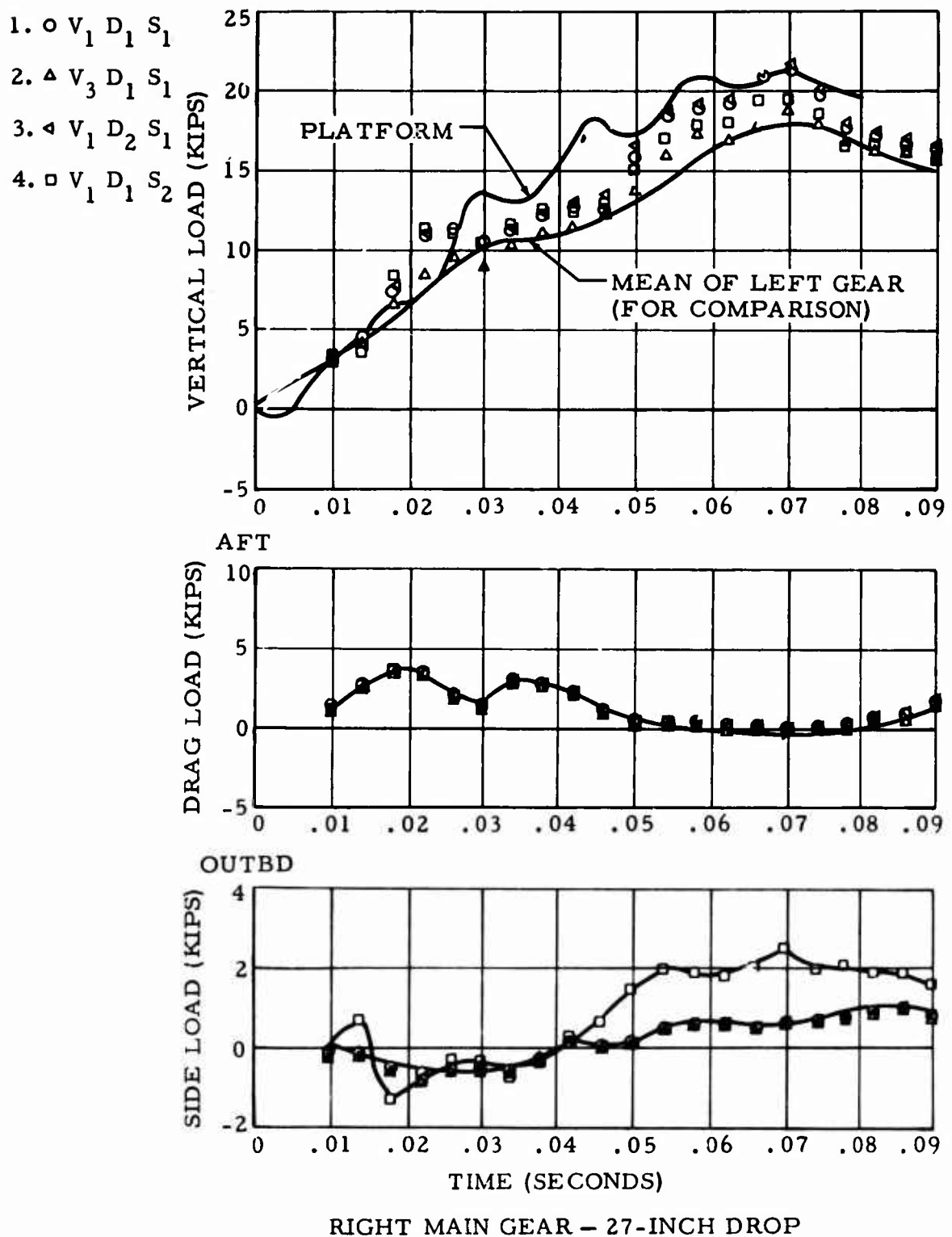
Figure 12. Load Response Curves - Right Main Gear.

30
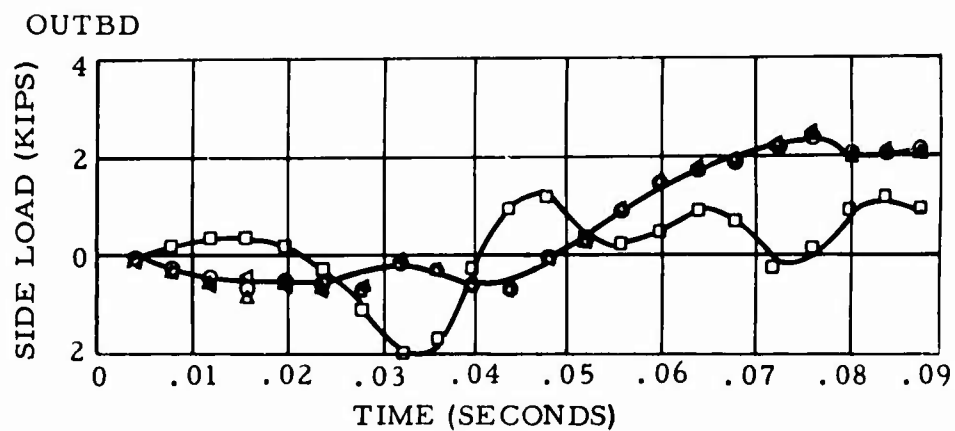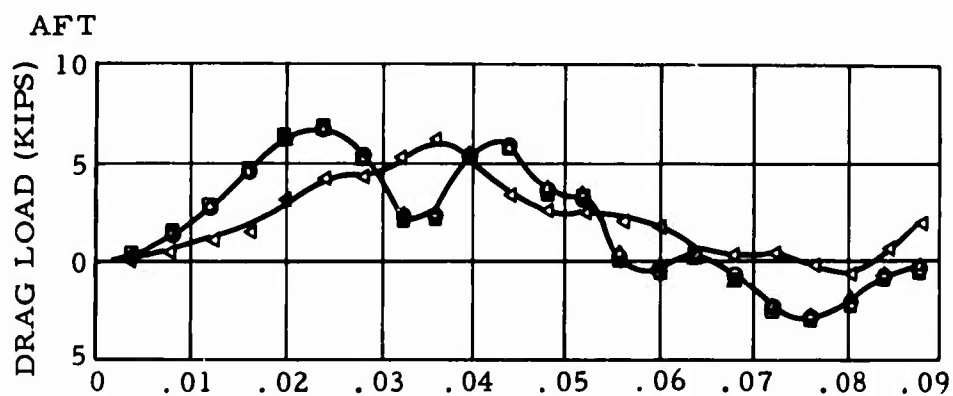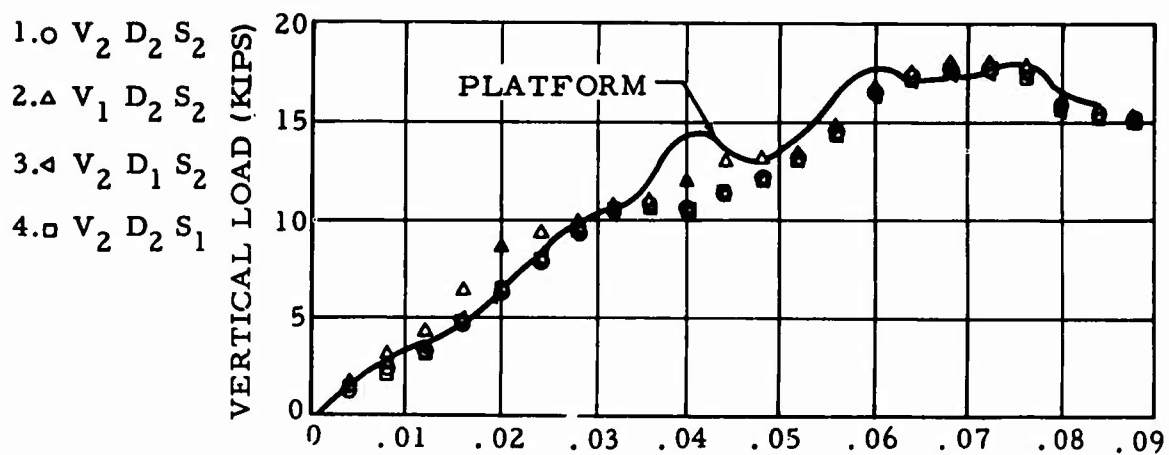
Figure 13. Load Response Curves - Left Main Gear.

31

1. O V_1 D_1
2. △ V_2 D_2
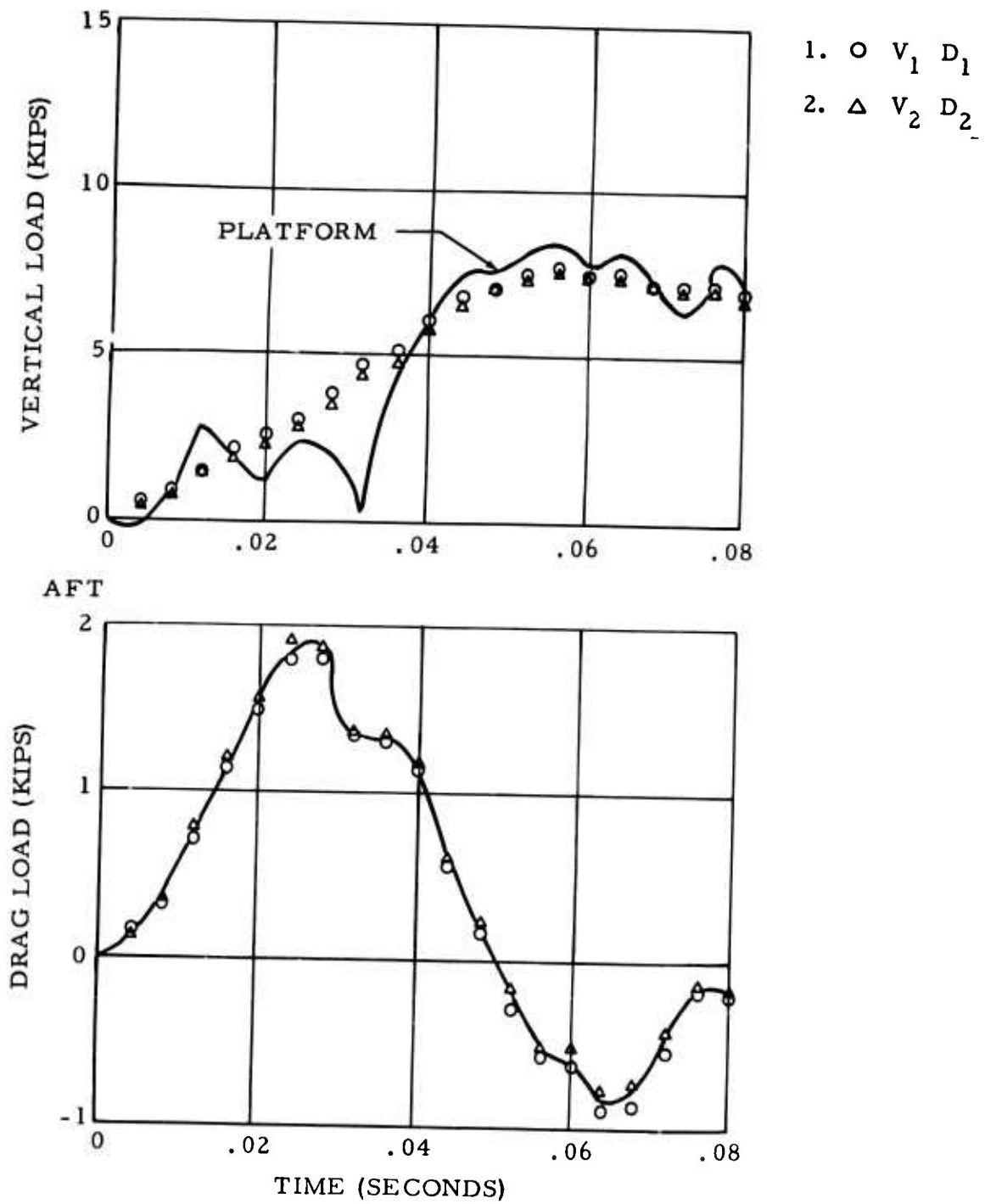
NOSE GEAR - 18-INCH DROP

Figure 14. Load Response Curves · Nose Gear.

32

SECTION II. FIELD TESTS

ROUGH FIELD MEASUREMENTS

Contour measurements of selected sod field landing sites at Camp
Pickett, Franklin, and Petersburg, Virginia, were performed to obtain
actual roughness data for correlating the mathematical expressions re-
lated to the gear dynamics during landings and rollouts. These data
were used to modify those portions of the computer program where
correlation was not obtained for each analytical printout. That is, for
each particular landing, the aircraft was mathematically flown to a
landing. These results were then compared to and correlated with the
actual measured test data.

The profilometer system used in the field measurements has been well
documented in TRECOM Technical Report 64-19 (Reference 1), and
consists of a collimated light source, contour tracker (including light
beam sensor), and both hydraulic and electrical power supply and
controls. The surface roughness sensed by the tracker was recorded
in digital form on paper tape which was then converted to IBM card
format for computer processing. A segment of one of the numerous
elevation plots of the Franklin field landing site is shown in Figure 15.

In order to provide further data on relative roughness, the Air Force
was requested to reduce the profile data to power spectral density
form. Appendix II is a report of the result of this analysis for the
Franklin and Camp Pickett, Virginia, test sites.

Soil penetration measurements were made throughout the 48-foot by 100-
foot target touchdown area and immediately adjacent to the aircraft's
touchdown and roll tracks within this area. A mobility cone penetrom-
eter having a 30-degree cone with a 0.5-square-inch base area was used
to measure the soil bearing strength. Readings obtained at the time
of the crash landing ranged from a low of 80 to a high of 121 psi.

AIRCRAFT INSTRUMENTATION

Three 18-channel oscillograph recorders were installed in the camera
and baggage compartment areas to record in-flight and landing dynamic
behavior of the airframe and landing gear. Except for the forward and
sink-speed radar velocimeters, the instrumentation system was typical
of general flight-test practice in that the various parameter measure-
ments were satisfied by the use of stock sensors and recorders. Appen-
dix III is a schematic of the test instrumentation circuitry reflecting the

33

parameters measured and the system components.

With respect to the special radar units, signal conditioners were designed to permit recording as well as indications to the pilot of his approach slant and sink speeds. Special cockpit panel meters were installed to aid the pilot in trimming the aircraft to satisfy the desired approach velocities. The functional theory for these devices is described in Appendix IV.

LANDINGS

Although three sod landing fields of increasing roughness were selected and contour measured at Franklin, Petersburg, and Camp Pickett, Virginia, only the former was used because of a landing accident. Since the accident occurred on the initial planned landing (on 3 August 1967), the two landings previously performed (on 18 July and 2 August) as pilot's proficiency and instrumentation qualification tests were necessarily used as sources for correlation and evaluation of the Douglas mathematical landing gear model. Certain parameter values, therefore, such as aircraft pitch and roll attitude, were intuitively determined to permit conduct of the mathematical analyses, since all measured data channels were not functional at these times. Table XV provides a summary of the adequacy of the measured parameters for analysis purposes.

Of the three landings evaluated, the 2 August landing was made on the concrete strip adjacent to the sod test area while the 18 July and 3 August landings were performed adjacent to and within the sod test area, respectively. Figure 16 depicts the physical relation of the three landing areas described, while Figure 17 shows the three simultaneous oscillograph records acquired for the crash landing of 3 August. Although 0.13 second of time elapsed from nose gear touchdown to loss of various signal traces, the separation of wheel strut caused severance of signal-carrying wires; therefore, the strut failure had to occur some time immediately prior to the wire failure. The mathematical simulation of this landing agrees with this reasoning in that gear failure was predicted to begin 0.06 second after contact of the nose wheel and ground. A close-up of the aircraft nose and the failed nose gear strut is shown in Figure 18.

(SOD LANDING STRIP)
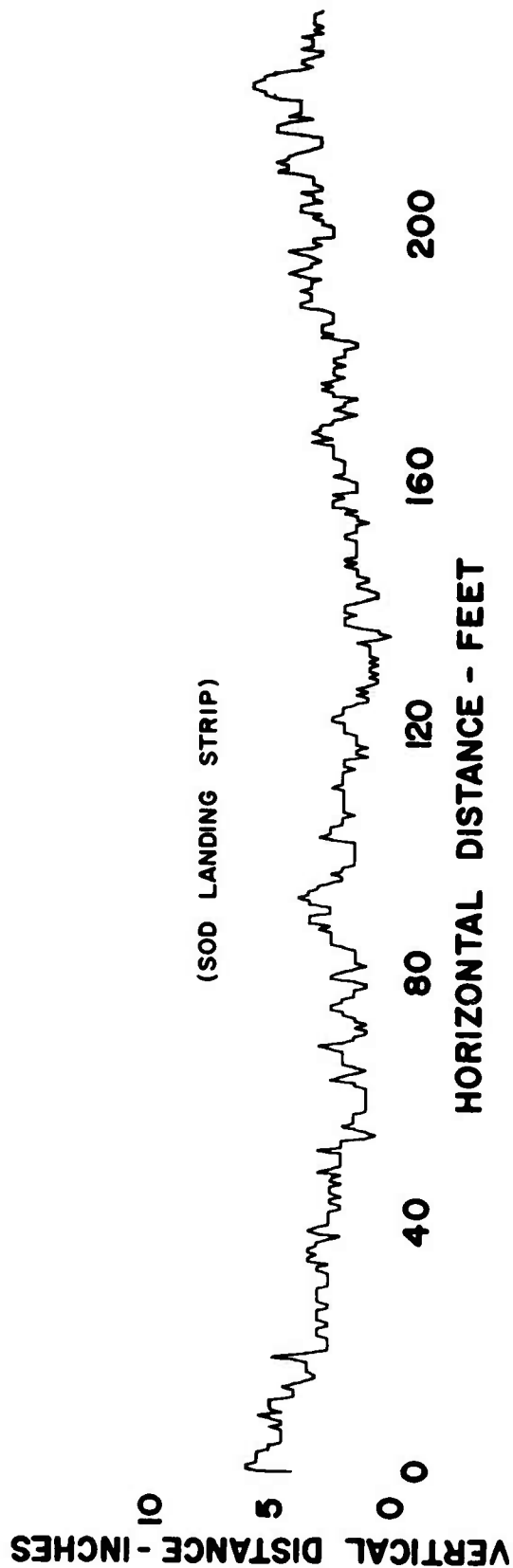
Figure 15. Roughness Plot of Franklin Field Landing Site.

35

1 - 18 JULY SOD LANDING
2 - 2 AUGUST CONCRETE LANDING
3 - 3 AUGUST SOD LANDING (CRASH)
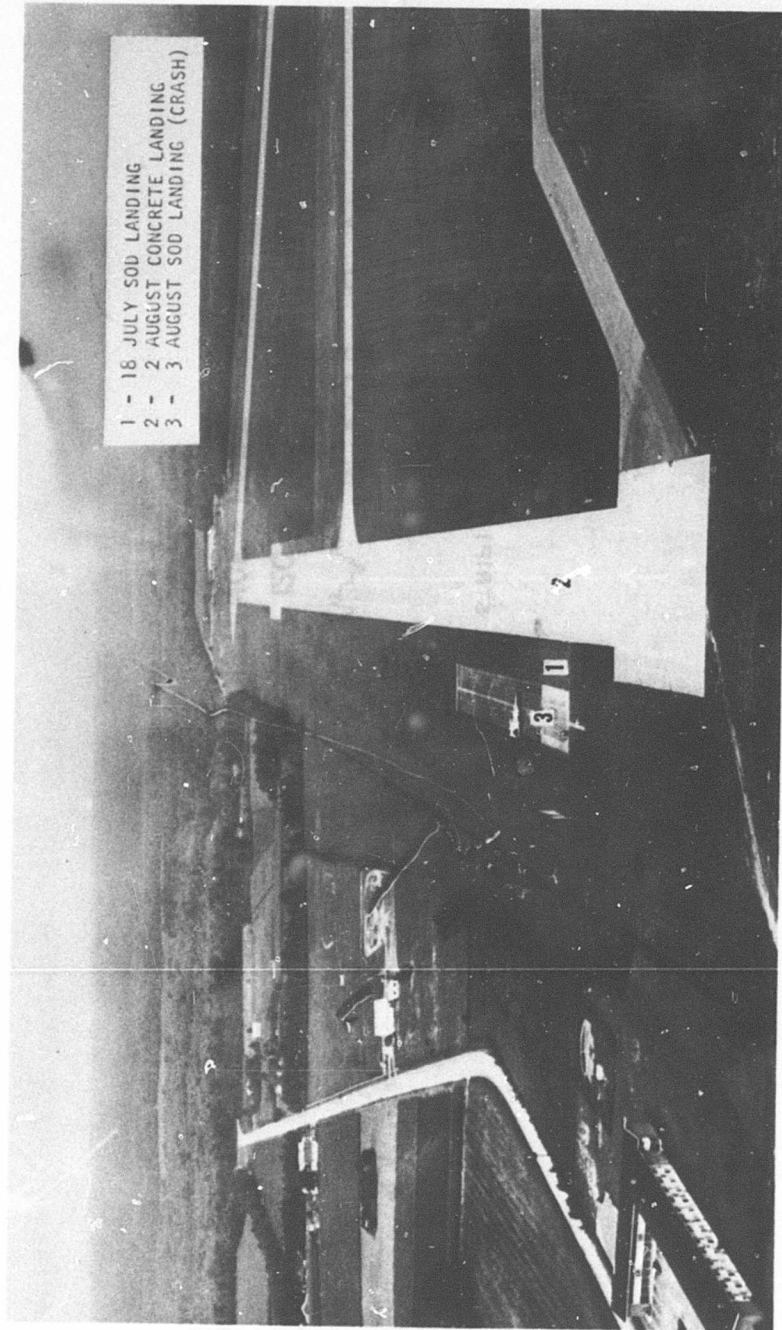
Figure 16. Landing Test Area at Franklin Field, Virginia.

36
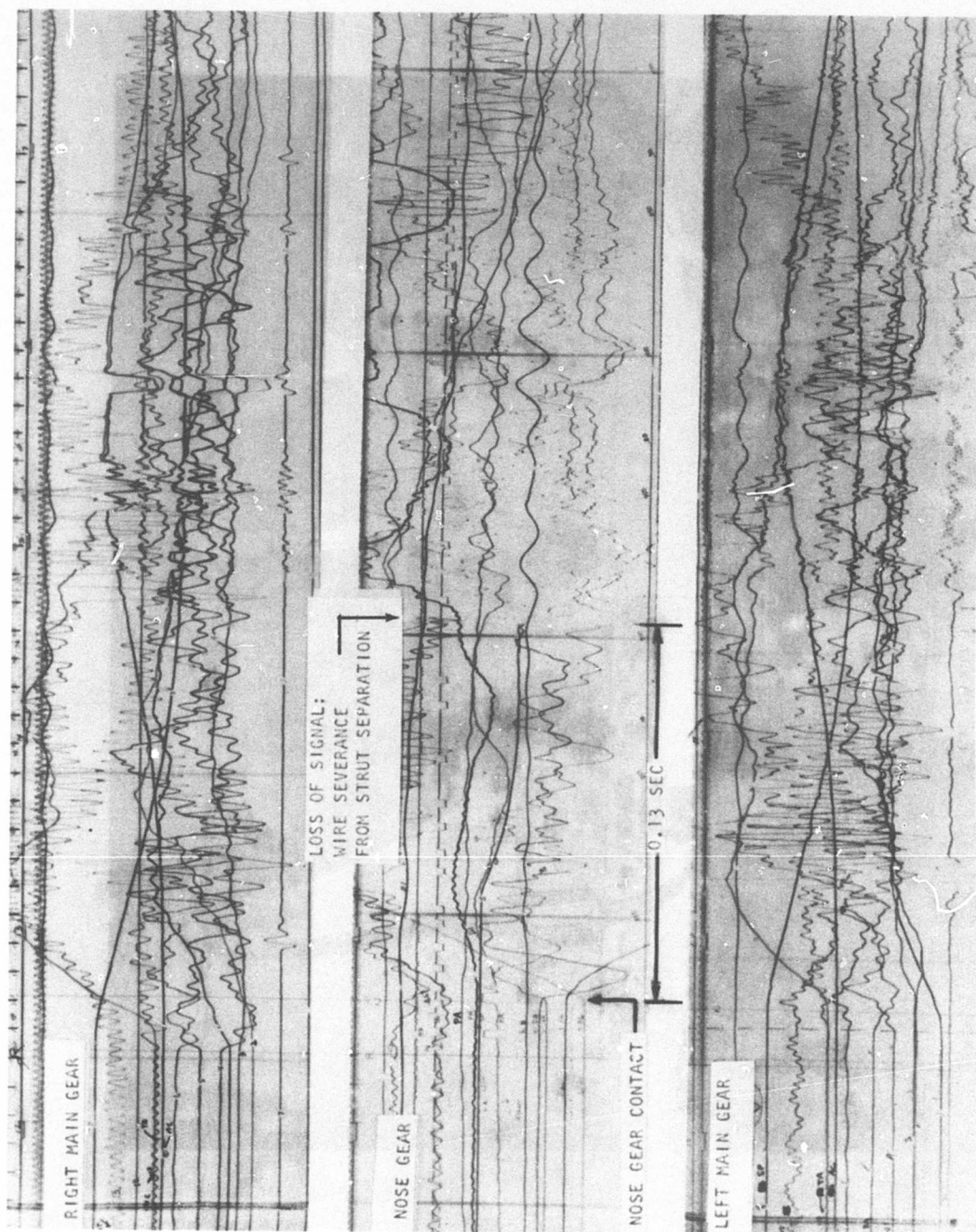
Figure 17. Oscillograph Record of OV-1A Landing Accident.

37
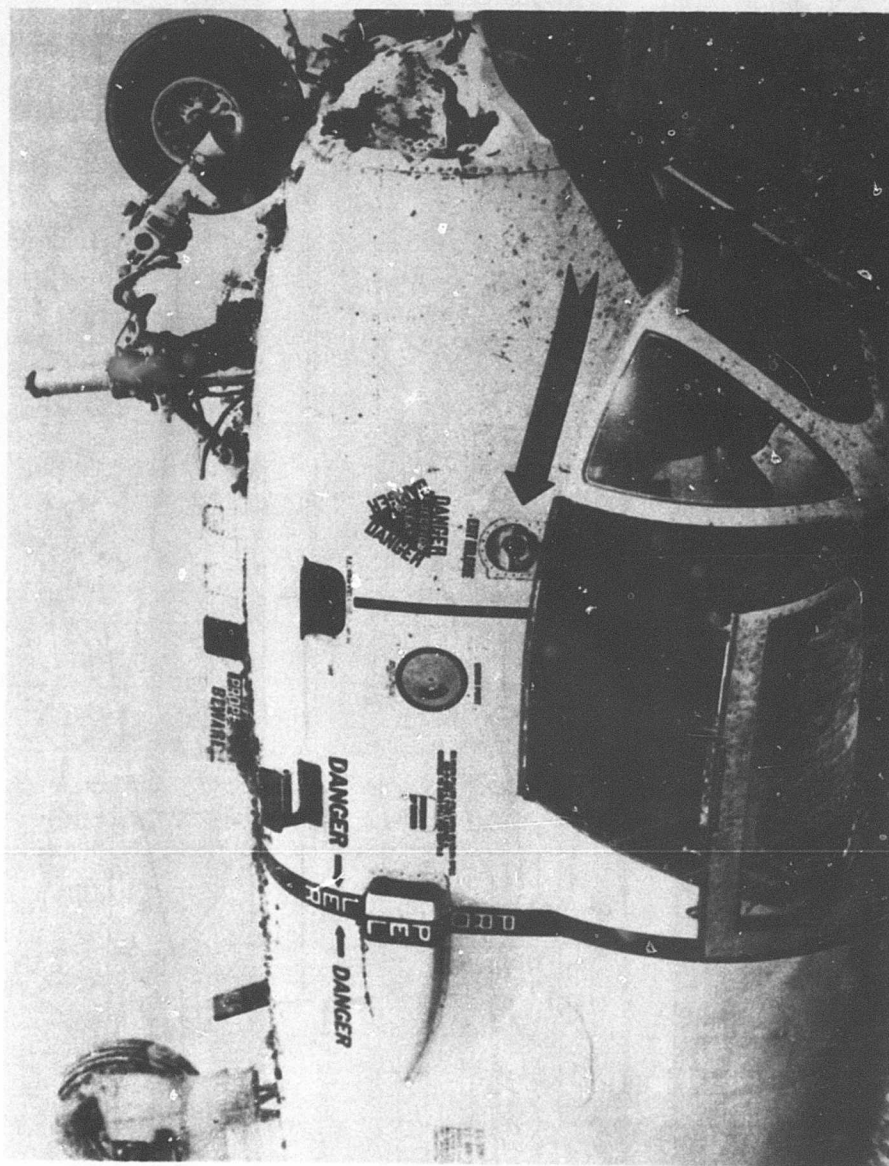
Figure 18. View of Failed Nose Gear Strut.

SECTION III. COMPUTED LOADS AND COMPARISON WITH TEST RESULTS

METHOD OF ANALYSIS

The calculated loads presented herein were obtained from a dynamic loads computing program in which the gear and airplane were considered as mutually interacting dynamic systems and in which the gear operating characteristics and airplane motion were simulated mathematically. The equations of motion in Appendix I were solved by means of numerical integration on the IBM 360 computer.

The computer program is based on those described in References 2 and 3; however, many extensions and refinements have been added, the most important of which are:

1. Pretouchdown calculations are included. The airplane is balanced in accordance with normal aerodynamic procedures and in conformance with the initial conditions established by the test data. Mathematically, the airplane is then "flown" in for the landing.

2. Pitch and roll degrees of freedom have been added to the airplane motion. These are in addition to the vertical and fore and aft translational degrees incorporated previously in References 2 and 3.

3. Provision has been made for inserting the contour of the ground into the program by a series of coordinates, thus making it possible to use any contour rather than only those that can be easily described mathematically.

4. The program uses a variable integration interval that is chosen automatically to give the required accuracy considering the rapidity of the motion. The interval is permitted to vary between 0.002 and 0.000008 second.

5. Refined equations have been incorporated for side and drag loads on the gear as well as for strut torsion.

6. New concepts of sliding and rolling coefficients of friction of the tire on the ground have been incorporated (see page 56).

39

7. Changes were made, as necessary, to adapt the program
    to the IBM 360 computer (was IBM 7094).

The computer was directed to print out significant items of information
every 0.002 second. The input required is shown in Tables IX through
XII. Items of output obtained from the program are listed in Table
XIII.

Computing time averaged 3 minutes for a landing impact involving 0.3
second of real time and 25 minutes for a landing impact plus rollout
covering 150 feet of rough runway (approximately 1.2 seconds of real
time).

LANDINGS SIMULATED

Loads were computed for three landings (see Figures 19 through 32):

1. 18 July 1967 - landing on sod at the airfield in Franklin,
    Virginia.

2. 2 August 1967 - landing on concrete at the airfield in
    Franklin, Virginia.

3. 3 August 1967 - landing on sod at the airfield in Franklin,
    Virginia (the nose gear failed, resulting in strike damage
    to the aircraft).

Initial conditions for these landings are provided in Table XIV. Most
of the data in this table was obtained directly from measurements. The
rest was deduced from measurements, either with or without the aid of
supplementary calculations as described in the following section.

In addition to the above three landings, calculations are provided for the
following:

1. An 8-foot-per-second landing and subsequent rollout for 150
    feet on a rough part of the Franklin field sod strip (contour
    shown in Figure 33).

2. An 8-foot-per-second landing and subsequent rollout for 150
    feet on a rough portion of the Camp Pickett field sod strip
    (Site I) (contour shown in Figure 33).

Comparison of the load time-histories of these landings and rollouts
shows the effect on landing gear loads of terrain of varying degrees of

SECTION III.   COMPUTED LOADS AND COMPARISON WITH TEST RESULTS

METHOD OF ANALYSIS

The calculated loads presented herein were obtained from a dynamic loads computing program in which the gear and airplane were considered as mutually interacting dynamic systems and in which the gear operating characteristics and airplane motion were simulated mathematically.   The equations of motion in Appendix I were solved by means of numerical integration on the IBM 360 computer.

The computer program is based on those described in References 2 and 3; however, many extensions and refinements have been added, the most important of which are:

1. Pretouchdown calculations are included.   The airplane is balanced in accordance with normal aerodynamic procedures and in conformance with the initial conditions established by the test data.   Mathematically, the airplane is then "flown" in for the landing.

2. Pitch and roll degrees of freedom have been added to the airplane motion.   These are in addition to the vertical and fore and aft translational degrees incorporated previously in References 2 and 3.

3. Provision has been made for inserting the contour of the ground into the program by a series of coordinates, thus making it possible to use any contour rather than only those that can be easily described mathematically.

4. The program uses a variable integration interval that is chosen automatically to give the required accuracy considering the rapidity of the motion.   The interval is permitted to vary between 0.002 and 0.000008 second.

5. Refined equations have been incorporated for side and drag loads on the gear as well as for strut torsion.

6. New concepts of sliding and rolling coefficients of friction of the tire on the ground have been incorporated (see page 56).

7.   Changes were made, as necessary, to adapt the program to the IBM 360 computer (was IBM 7094).

The computer was directed to print out significant items of information every 0.002 second. The input required is shown in Tables IX through XII. Items of output obtained from the program are listed in Table XIII.

Computing time averaged 3 minutes for a landing impact involving 0.3 second of real time and 25 minutes for a landing impact plus rollout covering 150 feet of rough runway (approximately 1.2 seconds of real time).

LANDINGS SIMULATED

Loads were computed for three landings (see Figures 19 through 32):

1.   18 July 1967 - landing on sod at the airfield in Franklin, Virginia.

2.   2 August 1967 - landing on concrete at the airfield in Franklin, Virginia.

3.   3 August 1967 - landing on sod at the airfield in Franklin, Virginia (the nose gear failed, resulting in strike damage to the aircraft).

Initial conditions for these landings are provided in Table XIV. Most of the data in this table was obtained directly from measurements. The rest was deduced from measurements, either with or without the aid of supplementary calculations as described in the following section.

In addition to the above three landings, calculations are provided for the following:

1.   An 8-foot-per-second landing and subsequent rollout for 150 feet on a rough part of the Franklin field sod strip (contour shown in Figure 33).

2.   An 8-foot-per-second landing and subsequent rollout for 150 feet on a rough portion of the Camp Pickett field sod strip (Site I) (contour shown in Figure 33).

Comparison of the load time-histories of these landings and rollouts shows the effect on landing gear loads of terrain of varying degrees of

roughness as predicted by the computer. The calculations for these two landings were made for an ideally "hard" surface; i. e., no deformation of the contour was considered.

LIMITATIONS IMPOSED BY AVAILABLE DATA

Since the instrumentation was still in the process of being debugged when the crash landing occurred, several channels were not working consistently or were not adequately zeroed during the three landings under investigation. Table XV lists the various channels and classifies the data as being satisfactory, not available, lacking a zero, or questionable.

For the 18 July and 2 August landings, lack of knowledge concerning the exact point of touchdown was most serious. This void in the data made it impossible to insert the terrain contour in the calculations, and it was questionable whether some of the load discrepancies were caused by surface irregularities or inappropriate assumptions in the calculations. Comparisons of calculated and measured loads will show, however, that the differences are no greater than those obtained in the test program of Reference 3, in which the terrain was known precisely.

Also, the zeros for the roll and pitch attitude were not known precisely. This deficiency was overcome by noting the time relationships for touchdown of the left and right gears in the case of roll and between the main and nose gears in the case of pitch.

No nose gear vertical load was reported for the 18 July landing, and since the drag load is dependent to a certain extent upon the vertical channel reading (see Table III), the accuracy of the drag load is questionable.

The nose gear load traces on the 3 August landing quickly went beyond the boundary of the record, so that the time of touchdown of the nose gear and the initial slopes of the load curves are the only data salvaged from the nose gear traces. The exact time of failure was somewhat difficult to determine. In fact, with a bending-type failure there is probably a substantial interval between the onset of permanent deformation and the separation of the part. From study of the records and the calculations, it is estimated that failure began at 0.06 second after initial touchdown and was complete at 0.15 second. The piston fracture came at a point corresponding to a stroke of 9 inches from fully extended; however, failing loads probably occurred several inches sooner.

41

TABLE IX. INPUT TO COMPUTER PROGRAM

Airplane Constants

Item	Symbol	FORTRAN Notation	Input Value	Units
Location of airplane center of gravity				
Fuselage station	Y_{cg}	YCG	166.5	in.
Waterline	Z_{cg}	ZCG	79.6	in.
Location of aerodynamic center				
Fuselage station	Y_{ac}	YAC	159.4	in.
Waterline	Z_{ac}	ZAC	79.6	in.
Location of thrust application				
Fuselage station	Y_{em}	YEM	97.0	in.
Waterline	Z_{em}	ZEM	95.5	in.
Angle of engine thrust with respect to airplane FRL	Ω_T	OMEGAT	1.58	deg
Ratio of elevator angle to horizontal stabilizer angle		EK	8.0	-
Engine thrust	T	THRUST	0.0	lb
Horizontal location of airplane center of gravity with respect to runway at touchdown	U_o	UZERO	0.0	in.

42

TABLE IX. Continued

Airplane Constants (Continued)

Item	Symbol	FORTRAN Notation	Input Value	Units
Airplane moments of inertia about center of gravity				
Pitch	I_{Ao}	PMOM	252000.	lb-in.-sec^2
Roll	$I_{\theta o}$	RMOM	181500.	lb-in.-sec^2
Largest time increment used in integration	Δt	DELT	0.002	sec
Accuracy required of integration routine	$\left\{ \epsilon \right\} \leq .2 \left\{ \dfrac{\lvert X_p - X_c \rvert}{\lvert X_p \rvert + \lvert X_c \rvert} \right\}$	EPSILON	0.01	-

Gear Constants

Item	Symbol	FORTRAN Notation	Input Value Left Main Gear	Right Main Gear	Nose Gear	Units
Location of strut attach point to airplane						
Lateral location	X	X	52.918	-52.918	0.0	in.
Fuselage station	Y	Y	186.25	186.25	40.75	in.
Vertical location	Z	Z	72.218	72.218	38.188	in.

43

TABLE IX. Continued

Gear Constants (Continued)

Item	Symbol	FORTRAN Notation	Input Value Left Main Gear	Input Value Right Main Gear	Input Value Nose Gear	Units
Weight of unsprung portion of strut (wheel, brakes, piston, etc.)	W_u	WU	140.0	140.0	54.0	lb
Angle of strut perpendicular to FRL (forward)	ϕ	PHI	1.5	1.5	-5.208	deg
Angle of strut perpendicular to FRL (clockwise looking forward)	σ	SIGMA	2.2	-2.2	0.0	deg
Distance from strut attach point to axle, strut fully extended	e_L	EL	65.0	65.0	44.2	in.
Axle forward offset from strut center line	e_d	ED	0.0	0.0	-2.75	in.
Axle offset to left side of strut center line	e_b	EB	0.0	0.0	0.0	in.
Distance between lower bearing and axle (strut extended)	A_{BRG}	ABRG	37.06	37.06	26.73	in.
Distance between upper and lower bearings (strut extended)	B_{BRG}	BBRG	10.5	10.5	7.05	in.
Aft deflection of strut for a unit load parallel to strut	K_1	K1	0.0	0.0	1.01×10^{-5}	in./lb
Stiffness of strut in aft direction due to an aft deflection	K_{32}	K32	2860.0	2860.0	2400.0	lb/in.
	K_{33}	K33	119.0	119.0	327.0	lb/in.^{2}

$F = (K_{32} + S K_{33})\delta$

TABLE IX. Continued

Gear Constants (Continued)

Item	Symbol	FORTRAN Notation	Input Value Left Main Gear	Right Main Gear	Nose Gear	Units
Side deflection of strut for a unit load parallel to strut	K_4	K4	0.00001	0.00001	0.0	in./lb
Stiffness of strut in side direction due to a side deflection	K_{22}	K22	5500.0	5500.0	0.0	lb/in.
$F = (K_{22} + S K_{23})\delta$	K_{23}	K23	921.0	921.0	0.0	lb/in.^{2}
Torsional stiffness of strut	K_β	KBETA	4.7×10^6	4.7×10^6	0.0	in.-lb/rad
Torsional inertia of strut about strut center line	I_β	IBETA	20.0	20.0	0.0	lb-in.-sec^2
Strut damping coefficients Aft direction	$\bar{C}$	CBAR	4.0	4.0	5.5	lb-sec/in.
Side direction	C_S	CS	20.0	20.0	0.0	lb-sec/in.
Torsional direction	C_β	CBETA	160.0	160.0	0.0	in.-lb/sec
Ground side coefficient of friction	μ_ψ	MUPSI	0.5	0.5	0.5	-
Lateral stiffness of tire	B	B	10000.0	10000.0	10000.0	lb/in.
Undeflected radius of tire	r_T	RT	13.06	13.06	9.92	in.
Maximum tire deflection	C_{Tmax}	CTN	9.0	9.0	8.0	in.
Mass inertia of rolling assembly	I_R	IR	7.55	7.55	1.5	lb-in.-sec^2

TABLE IX. Concluded

Gear Constants (Continued)

Item	Symbol	FORTRAN Notation	Input Value			Units
			Left Main Gear	Right Main Gear	Nose Gear	
Factor for effective rolling radius	e_r	ER	3.0	3.0	3.0	-
Maximum strut stroke	S_{max}	SN	15.0	15.0	11.0	in.
Density of hydraulic fluid in strut	ρ_o	RHO	0.777×10^{-4}	0.777×10^{-4}	0.777×10^{-4}	$\frac{lb\text{-}sec^2}{in.^4}$
Value of strut velocity for changing from static to sliding friction at bearings	S_S	SS	2.0	2.0	2.0	in./sec
Orifice area	A_o	AO	0.4418	0.4418	0.3068	in.^{2}
Internal area of oleo piston	A_1	A1	9.294	9.294	5.185	in.^{2}
Area of piston outer diameter	A_{pod}	APOD	12.566	12.566	7.139	in.^{2}
Air load in fully extended strut (pressure x A_{pod})	P_E	PE	1231.0	1231.0	330.0	lb
Volume of air in fully extended strut	V_{ea}	VEA	207.3	207.3	80.06	in.^{3}
Polytropic exponent for calculation of strut air load	n_1	N1	1.12	1.12	1.12	-
Distance from wheel center line to left of fork center line	e_x	EX	6.38	-6.38	0.0	in.

46

TABLE X. AERODYNAMIC DATA			
Airplane Angle of Attack (deg)	C_L *	C_D *	$C_{M_{ac}}$ *
-1.5	0.766	0.160	-0.0600
0.5	0.958	0.184	-0.0888
2.5	1.150	0.208	-0.1176
4.5	1.342	0.238	-0.1464
6.5	1.534	0.272	-0.1752
8.5	1.726	0.308	-0.2040
10.5	1.918	0.357	-0.2328
12.5	2.020	0.406	-0.2616
14.5	2.050	0.455	-0.2904

Mean aerodynamic chord	$\overline{C}$	=	98.0	in.
Wing area	S_W	=	330.75	ft^2
Change in airplane lift coefficient per unit elevator angle	$\dfrac{dC_L}{d\delta_e}$	=	0.0065/	deg
Change in airplane moment coefficient per unit elevator angle	$\dfrac{dC_{M_{ac}}}{d\delta_e}$	=	-0.018/	deg

* Parameters are assumed to vary linearly between points noted.

TABLE XI. TIRE LOAD DEFLECTION DATA

Main Gears		Nose Gear	
Deflection (in.)	Load* (lb)	Deflection (in.)	Load* (lb)
0.0	0.0	0.0	0.0
1.946	4600.0	0.910	1000.0
5.520	20000.0	2.200	3000.0
6.150	24300.0	3.710	6000.0
6.500	30000.0	4.026	7500.0
10.000	86000.0	4.320	10000.0
		4.550	14000.0
		6.550	48800.0

* A linear variation is assumed between points noted.

TABLE XII. METERING PIN DIAMETERS

Main Gears		Nose Gear	
Stroke (in.)	Diameter* (in.)	Stroke (in.)	Diameter* (in.)
0.00	0.640	0.00	0.510
2.80	0.640	1.44	0.510
5.80	0.520	3.94	0.484
12.88	0.687	7.94	0.580
15.40	0.687	12.00	0.580

* Diameter varies linearly between points noted.

48

TABLE XIII. COMPUTER PROGRAM DATA OUTPUT				
Airplane Data				
Item	Nomenclature			Unit
Center of gravity motion relative to airplane axes, from t=0:				
Vertical	H-DISP	H-VEL	H-ACC	in., sec
Fore and Aft	F-DISP	F-VEL	F-ACC	in., sec
Pitch	A-DISP	A-VEL	A-ACC	rad, sec
Roll	T-DISP	T-VEL	T-ACC	rad, sec
Aerodynamic loads at airplane center of gravity:				
Lift		AIR-1		lb
Pitch		AIR-2		in.-lb
Roll		AIR-3		in.-lb
Drag		AIR-4		lb
Aerodynamic loads at aerodynamic center:				
Lift		ALIFT		lb
Pitch		APITCH		in.-lb
Drag		ADRAG		lb
Engine thrust		THRUST		lb
Center of gravity locations relative to ground axes, from t=0:				
Vertical		DCG		in.
Horizontal		UCG		in.
Center of gravity velocities:				
Vertical		VZ		ft/sec
Horizontal		VE		ft/sec
Gear Data				
Axial strut load		FA		lb
Strut air load		PA		lb
Strut oil load		PO		lb
Strut friction load		PF		lb
Strut normal drag load		FD		lb
Strut normal side load		FB		lb
Strut torque		TBETA		in.-lb
Tire load normal to local ground		PV		lb
Tire load parallel to local ground (drag)		PD		lb

TABLE XIII. Continued		
Item	Nomenclature	Unit
Vertical tire load	PT	lb
Horizontal tire load (drag)	MUPT	lb
Horizontal tire load (side)	PS	lb
Tire deflection	CT	in.
Orifice coefficient	CD	-
Radial clearance between metering pin and orifice	ANN	in.
Oil velocity through orifice	VO	in./sec
Upper bearing normal load	F1TOT	lb

Upper bearing load:
  Drag direction
  Side direction
	
	F1
	F1S
		
		lb
		lb

Lower bearing normal load	F2TOT	lb

Lower bearing load:
  Drag direction
  Side direction
	
	F2
	F2S
		
		lb
		lb

Vertical deflection of top of strut due to airplane flexibility relative to center of gravity	STDF	in.

Wheel Motion:
  Yaw
  Rotation about axle
	
	DISP, VEL, ACC - BETA
	DISP, VEL, ACC - OMEGA
		
		rad, sec
		rad, sec

Slip ratio	SR	-
Sliding coefficient of friction(tire on ground)	MU	-
Axle acceleration parallel to strut (total)	ACC-AA	in./sec^2

Acceleration of axle normal to strut:
  Drag
  Side
	
	ACC-DD
	ACC-BB
		
		in./sec^2
		in./sec^2

Elastic motion of axle normal to strut relative to airplane:
  Drag
  Side
	
	DISP, VEL, ACC - DBAR
	DISP, VEL, ACC - BBAR
		
		in., sec
		in., sec

TABLE XIII. Concluded		
Item	Nomenclature	Units
Deflection of strut due to axial load:		
Fore and aft	DFA	in.
Side	SFA	in.
Strut telescoping motion	DISP, VEL, ACC - S	in., sec
Location of axle relative to runway origin:		
Vertical	D	in.
Horizontal	U	in.

TABLE XIV. INITIAL CONDITIONS FOR LANDINGS

Item	Symbol	FORTRAN Notation	Landing			Units
			18 Jul 67	2 Aug 67	3 Aug 67	
Airplane gross weight	W	W	11750.0	11926.0	11926.0	lb
Airplane airspeed parallel to horizontal	V_y	VY	125.0	123.0	124.0	ft/sec
Airplane sink speed perpendicular to horizontal	V_z	VZ	8.0	11.0	19.5	ft/sec
Velocity of head wind	V_w	VW	6.0	-5.0	1.8	ft/sec
Angle of FRL with respect to horizontal (pitch attitude) (+ nose up)	A	A	9.8	9.05	5.0	deg
Airplane pitching rate (+ nose up)	$\dot{A}$	A-VEL	0.0	0.0	-0.042	rad/sec
Roll attitude of airplane (+ left wing down)	θ	THETA	-0.50	-1.0	-1.25	deg
Roll rate of airplane (+ left wing down)	$\dot{\theta}$	T-VEL	-0.087	0.012	-0.175	rad/sec

	Landing		
Parameter	18 July	2 Aug	3 Aug
Left Gear Loads			
Vertical	S	S	S
Drag	S	S	S
Side	S	S	S
Right Gear Loads			
Vertical	Q	S	S
Drag	Q	S	S
Side	NA	S	S
Nose Gear Loads			
Vertical	NA	S	NA
Drag	Q	S	NA
Gear Accelerations	S	S	S
Gear Stroke			
Left	S	S	S
Right	S	S	S
Nose	S	S	Q
Main Gear Top Acceleration	S	S	S
Oil Pressure			
Left	S	S	S
Right	Q	S	S
Air Pressure			
Left	NA	S	S
Right	NA	NA	S
Wing Tip Acceleration			
Left	NA	S	S
Right	NA	S	S
Airplane Velocities			
Horizontal	S	Q	S
Vertical	S	S	S
Airplane Attitude			
Pitch	N-0	N-0	N-0
Roll	N-0	N-0	N-0
Airplane Rates			
Pitch	S	S	S
Roll	Q	Q	Q
Airplane Accelerations			
CG	NA	S	Q
Pilot Station	NA	S	Q
Wheel Position Pip	S	S	S
Elevator Position	S	S	S

S-Satisfactory; Q-Questionable; NA-Not Available; N-O, No Zero

Failure of the nose gear was duplicated on the computer by reducing the nose gear vertical load drastically at 0.07 second after touchdown. This was accomplished by arbitrarily reducing the ground elevation under the nose gear at that time. Main gear loads were then calculated for another 0.2 second. The measured stroke on the nose gear for the 3 August landing is considered to be questionable, since no stroke is recorded for 0.03 second after nose gear impact, as determined from load and accelerometer traces.

The sink-speed indicator (page 33) measured the relative vertical speed of the airplane and the ground. The device was quite accurate; however, when the airplane flew over rough terrain, the ground reference changed with airplane horizontal position, and an irregular record was produced. The irregular readings obtained from the 18 July and 3 August landings produced a source of possible error. Values used in the calculations were obtained by consideration of both the sink-speed indicator readings and the total energy in the measured load-stroke diagrams of the gears.

UNUSUAL PHENOMENA

On examination of the test data, several unusual phenomena were noted that required changes or additions to the computing program. This was to be expected with regard to the rough field landings; in fact, the discovery of such phenomena was one of the purposes of the test program. However, the first problem occurred with the concrete landing and consisted of a marked difference between the behavior of the right and left gears. This difference is illustrated by Figure 19, which compares the vertical loads obtained from the two gears.

The left gear behaved in what was considered to be a standard manner, and the loads could be predicted by the computer without difficulty. The right gear vertical load displayed a low average value combined with an extended stroke. Load pulses were superimposed on the average load curve at regular intervals, as though the gear were running over a series of small bumps. Examination of the oil chamber pressure and axle acceleration traces confirmed that the pulses were real and not a product of malfunctioning instrumentation. Examination of the right gear stroke-time curve showed an initial slope that was higher than expected for the measured airplane sinking speed. The right gear's behavior resembled that observed on a nose gear of another airplane. This behavior, which was caused by air in the chamber below the orifice at the time of impact, occurred when the gear was lowered immediately before touchdown. In other words, in the retracted position, oil flowed into the air chamber above the orifice and did not have sufficient time to flow back between the

time of gear extension and touchdown. Whether this was the problem with the Mohawk right gear during this particular landing is not known, but the average load curve could be predicted reasonably well if the fluid density in the orifice flow equation was reduced radically for the first 4.4 inches of stroke. Treating the right gear in this manner permitted a satisfactory calculation of the left gear loads, the airplane motion between main and nose gear touchdown, and the nose gear loads. The computing program was not able to predict all ramifications of the right main gear loads without major modification, and extended effort was not made to duplicate those loads in detail.

The "failure landing" of 3 August 1967 produced unusual main gear load records, as shown in Figure 28. The flat spots at "A" and "B" are considered to be associated with failure of the soil underneath the gears. Static and dynamic tests of soils have shown that they have load deflection curves similar to those in Figure 34, obtained from Reference 4. The ultimate strength undoubtedly varies with moisture content; on an unprepared field recently subjected to a rainfall, the moisture content could vary from point to point. This theory is offered as an explanation of the difference in strength between the left and right gears as noted in the load-time curves of Figure 28. The method of accounting for soil deformation and its effect on gear loads is described in the following section.

EFFECT OF SOIL DEFORMATION ON GEAR LOADS

Calculation of Soil Deformation for the 3 August Landing

The characteristics of soils depicted by Figure 34 can be duplicated qualitatively by a nonlinear spring-mass-damper mechanical system. Early attempts at duplicating the loads for the 3 August landing consisted of representing the soil by a nonlinear spring only. They were not successful because the calculated main gear drag loads tended to build up in phase with the vertical loads; whereas in the measured loads, the drag lagged considerably behind the vertical (see Figure 28).

The computer required a tire load versus soil deflection curve input rather than a soil pressure versus deflection curve input. It is pertinent to examine qualitatively the shape of this curve. To do this, it is necessary to know the nature of the soil pressure versus tire load curve. Up to the point of tire bottoming, the footprint pressure of a tire is approximately constant and equal to the inflation pressure, p_0. Loads in excess of the tire-bottoming load P_{TB} increase the footprint pressure so that

$$P = P_o + \frac{P_T - P_{TB}}{A}$$

The effective area, A, on which $P_T - P_{TB}$ operates is somewhat less than the normal footprint area because the loads tend to concentrate under the rim. Figure 31 shows the qualitative pressure-load relationship. The dotted line to the left indicates that the transition to p_o is something other than a step function. This occurs at small tire deflections, and its exact nature is not important to this problem.

Figure 36 shows the qualitative tire load versus soil deflection curves derived from the soil curves presented and the tire load/soil pressure curve of Figure 35. The relationship between P_{TB} and P_T at failure in these two curves is approximately the same as that observed in the records for the left and right gears. An approximation to the P_T versus δ_S curve is a rectangle in which $P_{T(FAILURE)}$ and δ_{SB} are the distinguishing features. This is obviously a better approximation for the left gear than the right. $P_{T(FAILURE)}$ is available from the records. The value of δ_{SB} and the damping constant were determined by trial. The curves that were used in the final correlation are shown in Figure 37.

Resistance to Forward Motion in Soft Soil

The total resistance to forward motion occurring at the contact area of the tire with the ground is considered to be made up of sliding and rolling friction, where sliding friction is defined as that which causes the wheel to accelerate its rotational motion about the axle, and rolling friction is the remainder. During a landing on concrete, the rolling friction is almost small enough to be neglected; the sliding friction coefficient is large, approaching a value of 1.0 at certain values of slip ratio. In contrast, a landing on soft soil produces a low sliding friction and a high rolling friction. The major portion of the rolling friction on soft soil is assumed to come from deformation of the soil.

The low sliding friction in the landing on sod makes the spin-up time longer than that for concrete. If the soil is soft, the higher rolling friction causes a total drag load which is high and apparently inconsistent with the spin-up time, and the springback is diminished or eliminated.

For the 18 July landing on sod, adequate correlation between calculated and measured loads was obtained by using a maximum sliding coefficient of friction of 0.3 and a rolling coefficient of 0.2. All evidence pointed to the fact that soil deformation in this landing remained elastic and was small. For the 3 August landing, the soil deformation was calculated by the computing program as described earlier, and the rolling resistance

56

was related to this deformation as described in the following paragraphs.

Assume that a wheel-mass-shock strut system with vertical velocity only is dropped on soft soil, as shown in Figure 38a. At any instant of time after gear contact, the tire will have penetrated the soil a distance δ_S. The kinetic energy loss of the mechanical system up to that point will have been absorbed partly by deflection of the shock strut damper, partly by the tire deflection, and partly by the soil. Now assume that the wheel is moved forward a distance ΔX. The soil energy as represented by the deflection of the soil springs in the shaded area (Figure 38b) is

$$E_S = K p A \delta_S \tag{8}$$

where K =   a proportionality constant

p =   the pressure at the tire-soil interface

A = $\Delta X. w$ = the planform area of the rut formed during horizontal motion

w =   trough width

The horizontal kinetic energy subtracted from the moving vehicle, resulting from the aft force imposed on the wheel by the soil, is

$$E_A = D . \Delta X \tag{9}$$

where D =   the resistance to forward motion.

Equating these energies and substituting for A,

$$D . \Delta X = K p w . \Delta X . \delta_S \tag{10}$$

$$D = K p w \delta_S \tag{11}$$

Thus, the drag load on the gear is proportional to the footprint pressure and the frontal area of the trough.

The soil springs are actually springs, masses, and dampers. However, under dynamic loads, the masses and dampers produce a nonlinear force deflection curve. In terms of the quasi-static approach, the value of K will vary between 0.5 and 1.0 and, within this range, will be a function of δ_S. For these purposes, K will be assumed to have one value up to the point of tire bottoming and another value above the bottoming, thus approximating a nonlinear curve by two straight lines. It must also be

57

assumed that the forward velocity does not change appreciably during the period under investigation.

Below the tire-bottoming load, p is approximately constant and w varies as $P_T^{1/2}$. Therefore,

$$D \cong K \sqrt{P_T} \cdot \delta_S \qquad \text{below tire bottoming} \qquad (12)$$

Above tire bottoming, w can be assumed constant, and

$$p = p_o + \frac{P_T - P_{TB}}{A} \qquad \text{(see page 56)} \qquad (13)$$

so that

$$D \cong K_1 \cdot p_o + K_2(P_{TB} - P_T)] \delta_S$$

$$= D_B + K_3(P_{TB} - P_T) \delta_S \qquad \text{above tire bottoming} \qquad (14)$$

where D_B = the drag which exists as the time of tire bottoming.

Values of ground coefficient of friction derived from test data are presented in Figure 39.

ROUGH-TERRAIN LANDINGS AND ROLLOUTS

The calculated loads obtained from the 8-foot-per-second landings and rollouts on rough portions of the Franklin and Camp Pickett sites are shown in Figures 40 through 44. The gear loads for the landing at the Franklin site are relatively moderate after the landing impact. Those for the Camp Pickett site are severe and are sufficient to cause failure of the nose gear during the rollout phase. During landing impact, bumps increased the maximum vertical load on the Franklin field landing from 12,000 to 14,000 pounds and on the Camp Pickett field landing from 12,000 to 32,500 pounds over that calculated for the 18 July landing, which was on a relatively smooth portion of the Franklin field.

58

Since the maximum permissible vertical load on the main gear is 37,000 pounds, it is evident that failure would have occurred at the Camp Pickett site during landing impact at 8 feet per second if the bump load shown in Figure 40 at t = 0.11 had occurred 0.05 second earlier, at which time it would have been superimposed on the load resulting from impact.

The gears were off the ground during a substantial portion of the Camp Pickett rollout. It appears that bouncing is unavoidable on a terrain as rough as this one.

Based on these calculations, it is concluded that the airplane has sufficient strength for a field with a roughness spectrum equal to or less than that of the Franklin field site. However, similar calculations for other airplanes have shown that there is a critical airplane speed for crossing ground roughness and that calculations should be made at other speeds before judgment is passed. The critical speed depends upon the natural frequency of the airplane in pitch and heave (while on the ground) and the frequency content of the ground roughness.

Ground roughness of the nature of the Camp Pickett site is too severe for the airplane as currently designed.
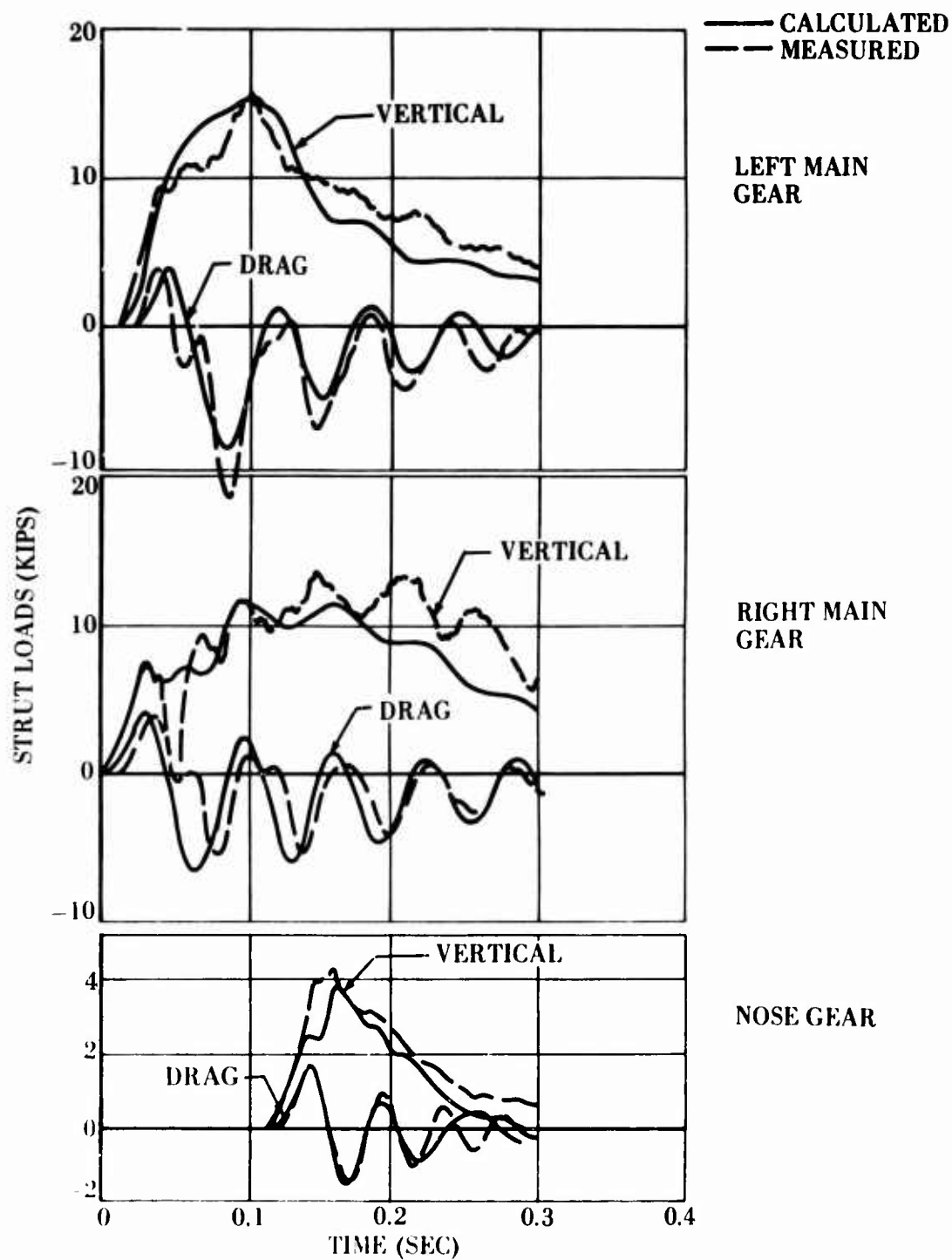
Figure 19. Comparison of Measured and Calculated Strut Loads for the 2 August Landing.
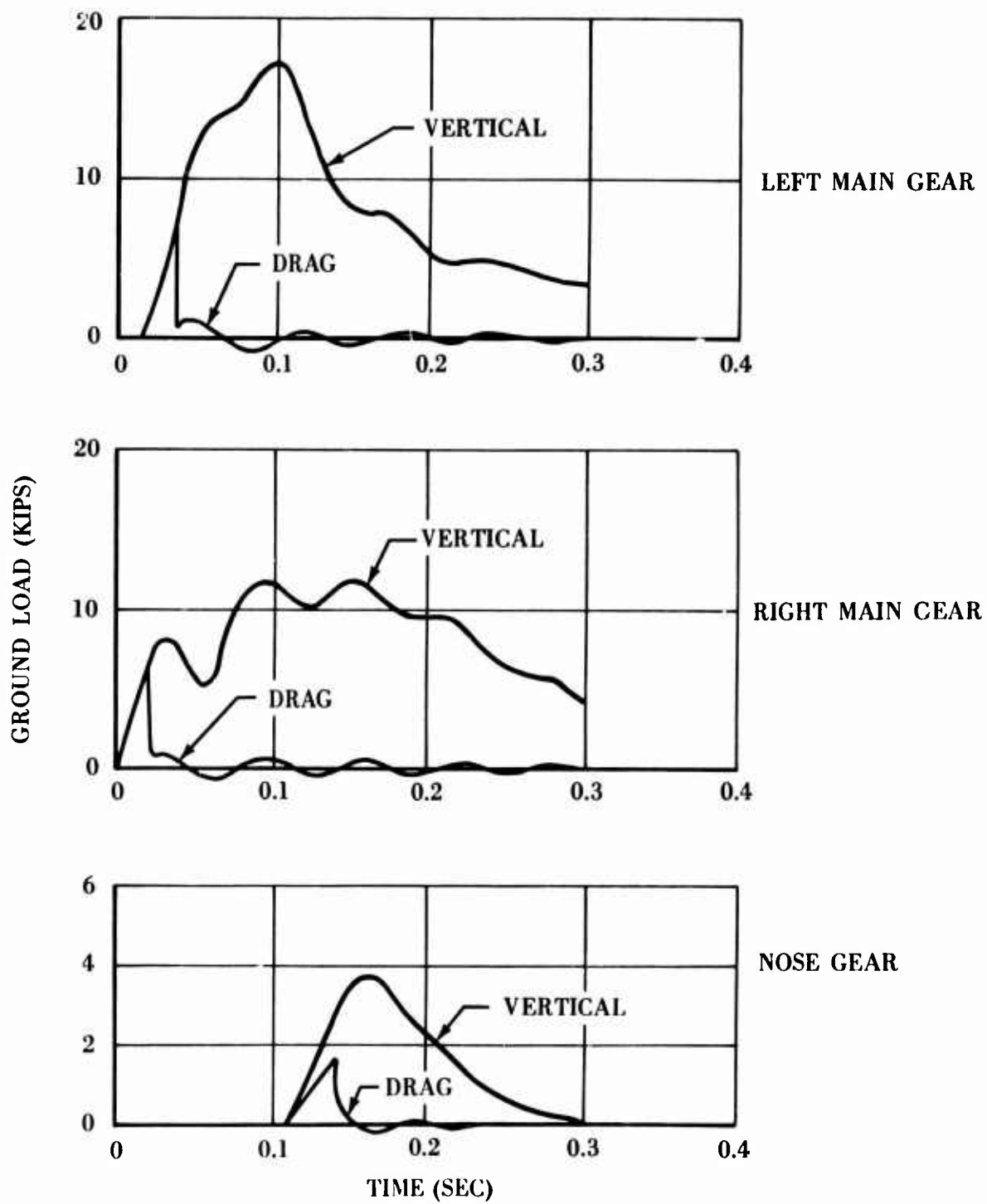
60

Figure 20. Calculated Ground Loads for the 2 August Landing.
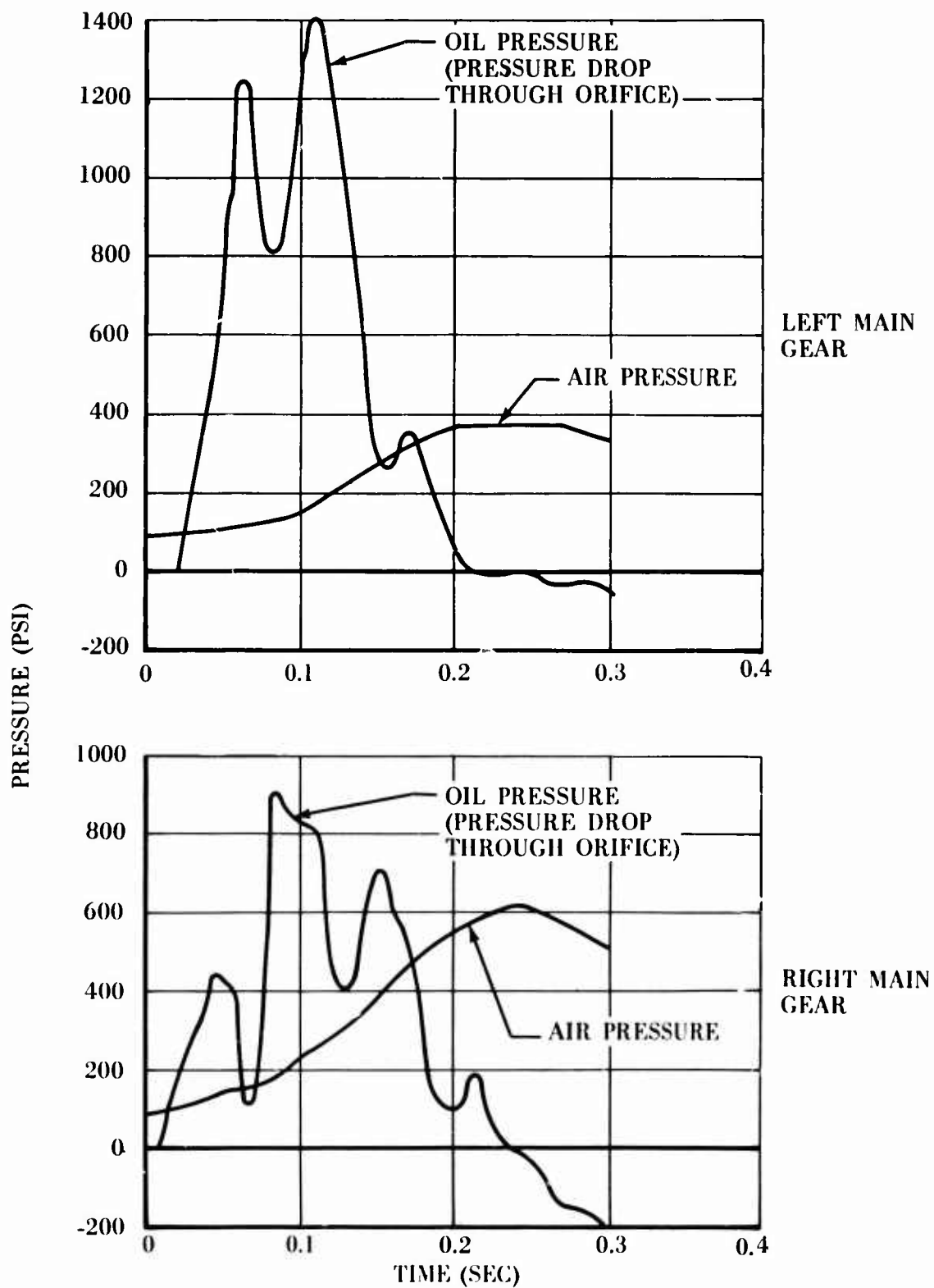
Figure 21. Calculated Strut Air and Oil Pressures for the
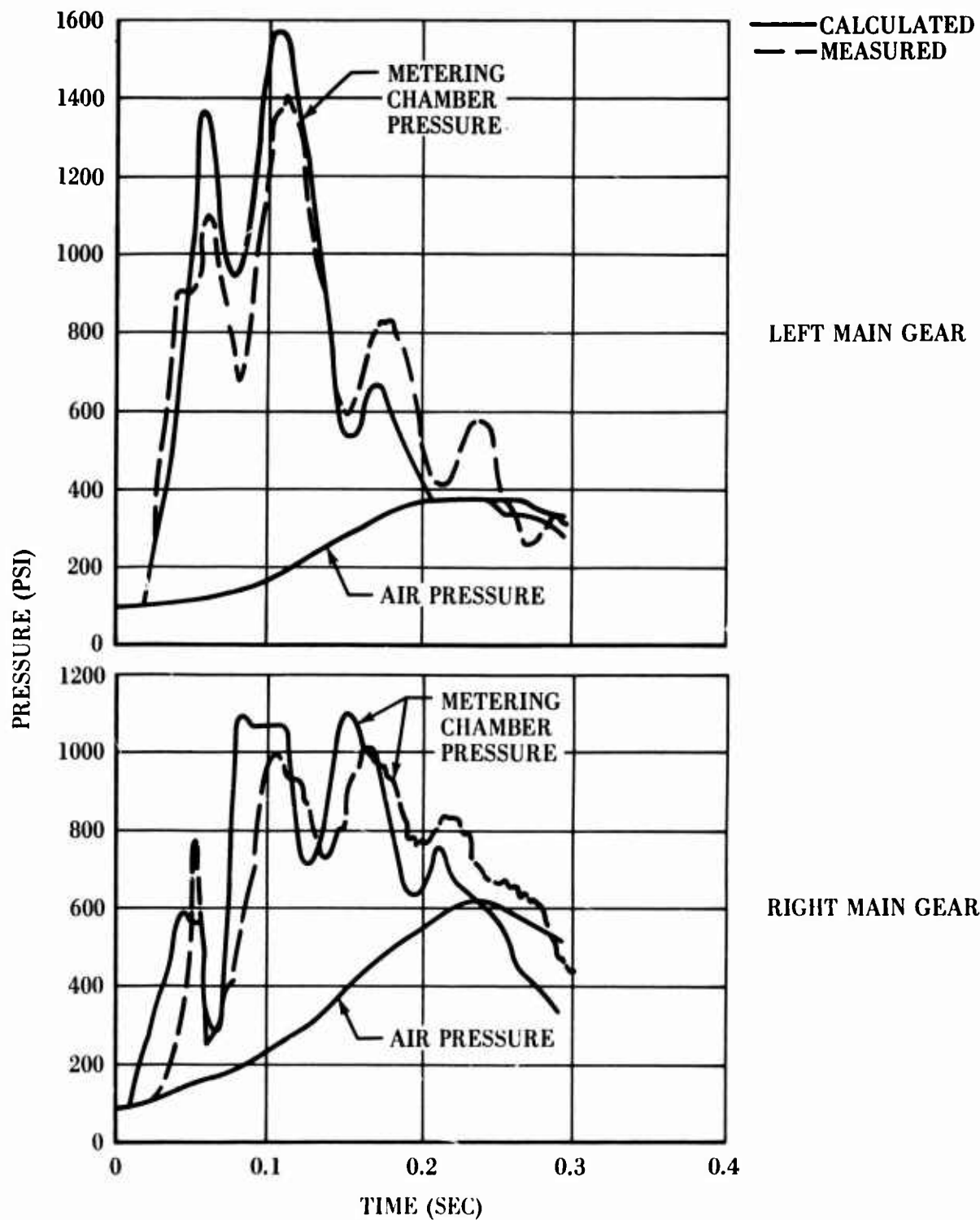2 August Landing.

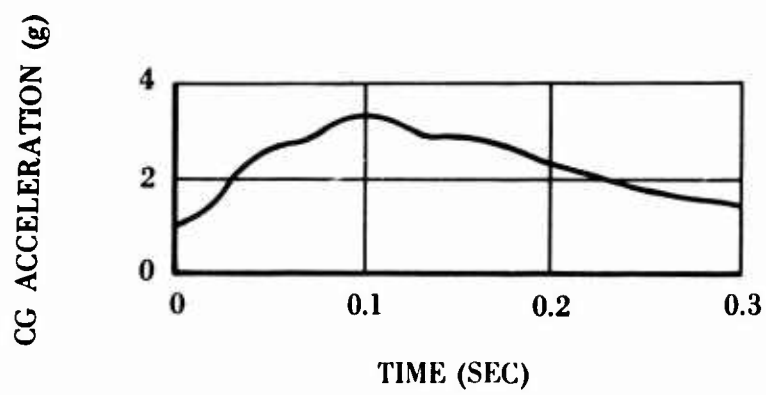Figure 22. Calculated and Measured Strut Pressures for the
2 August Landing.

63

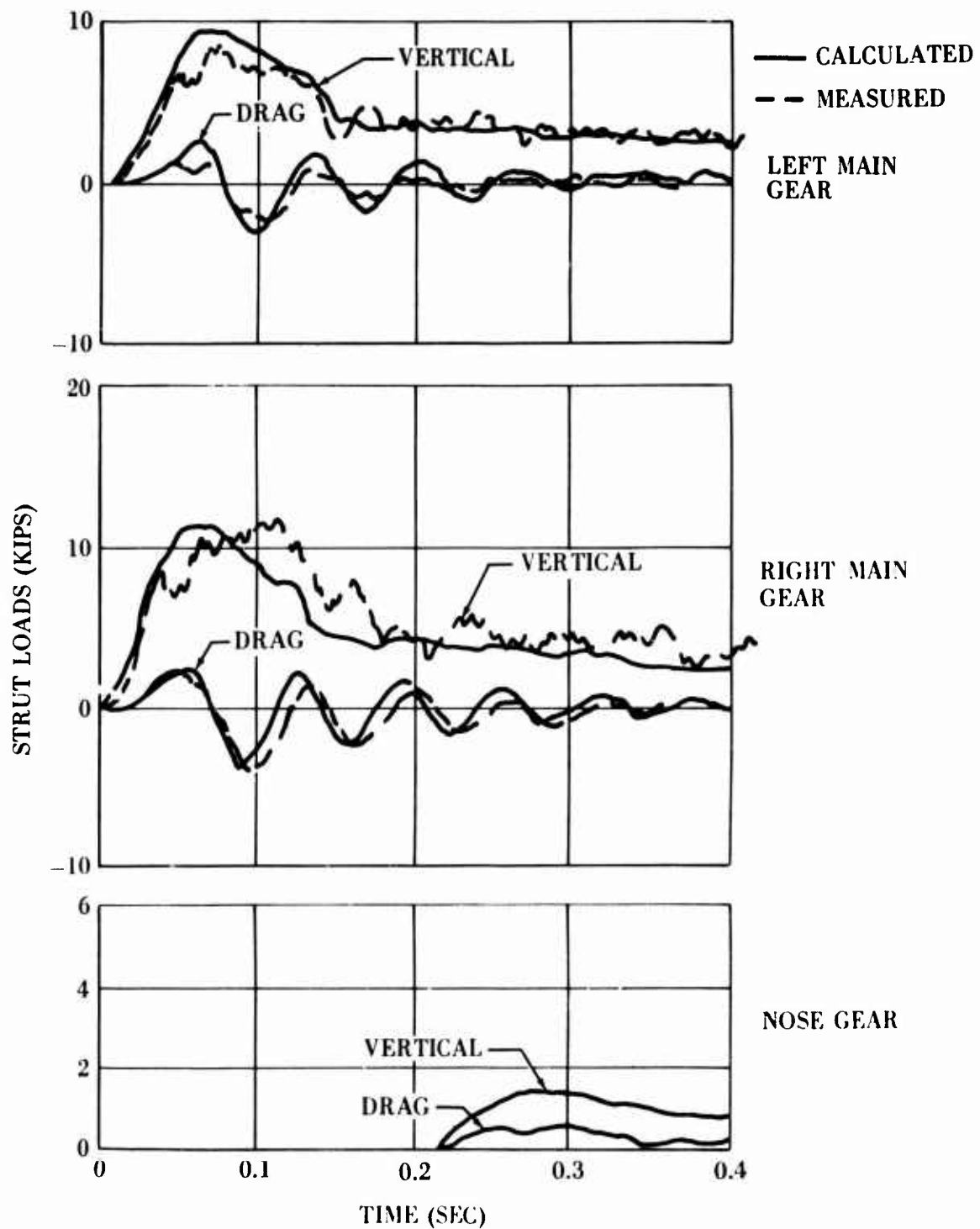Figure 23. Calculated CG Acceleration for the 2 August Landing.

Figure 24. Comparison of Measured and Calculated Strut Loads for the 18 July Landing.
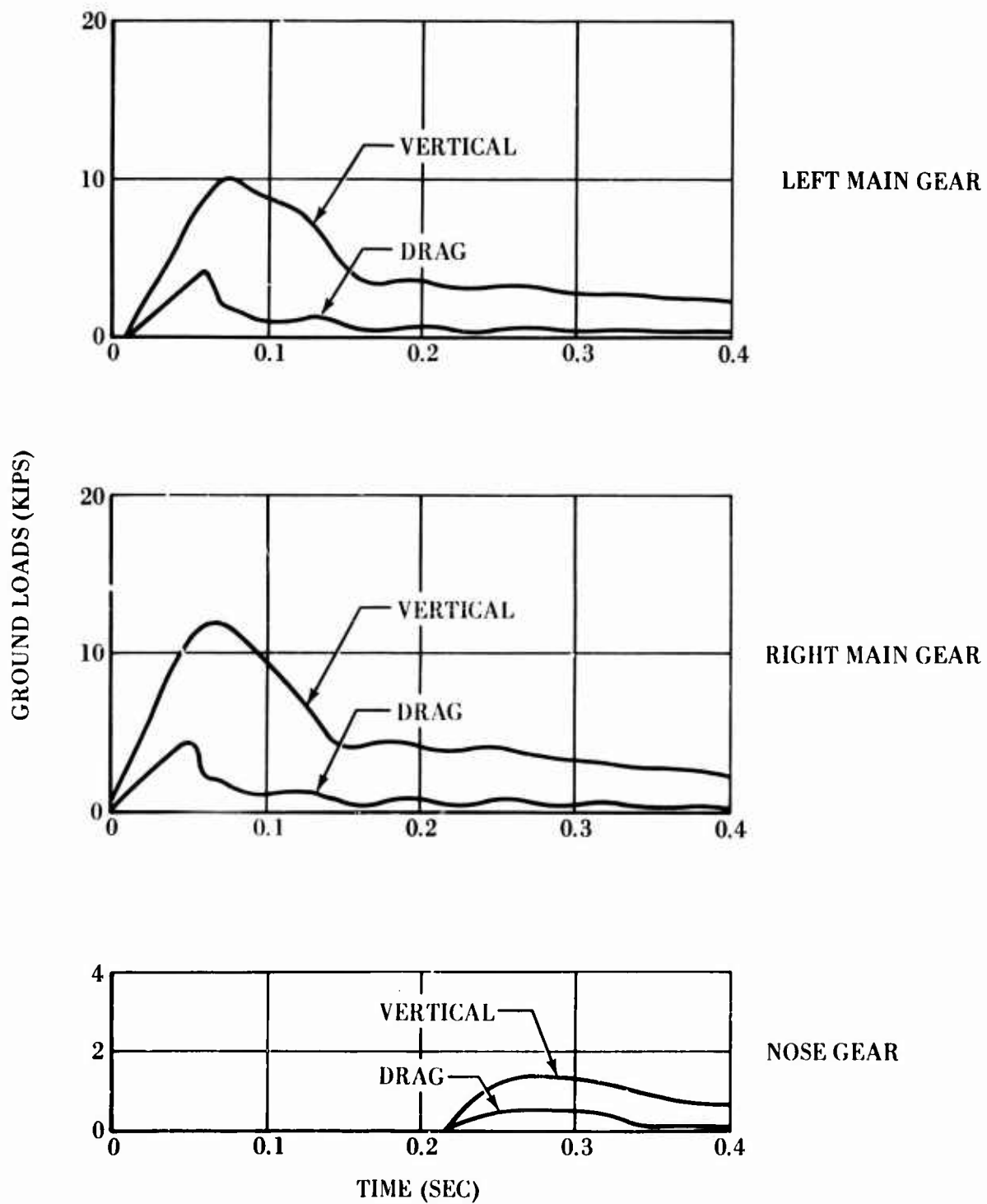
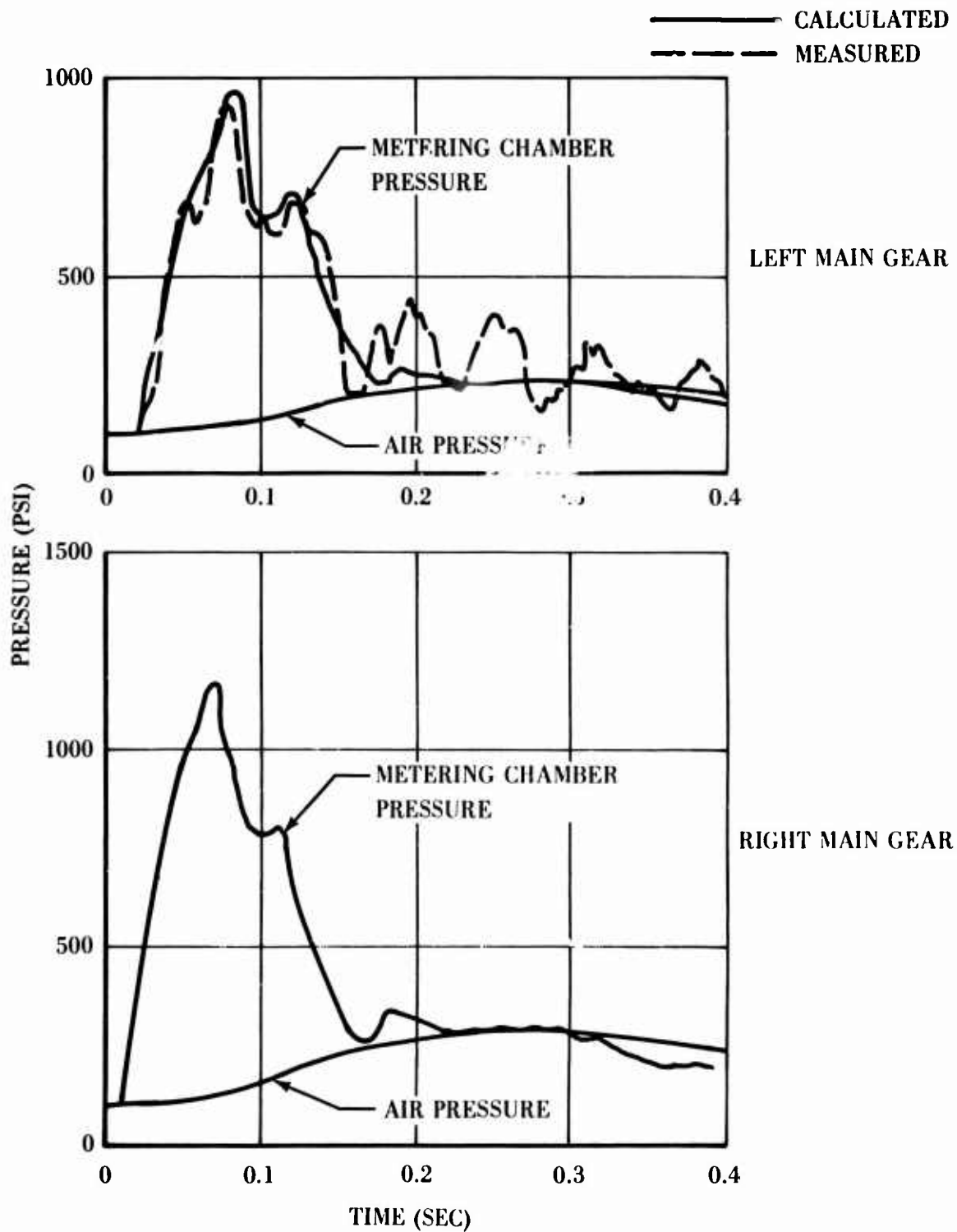Figure 25. Calculated Ground Loads for the 18 July Landing.

Figure 26. Calculated and Measured Strut Pressures
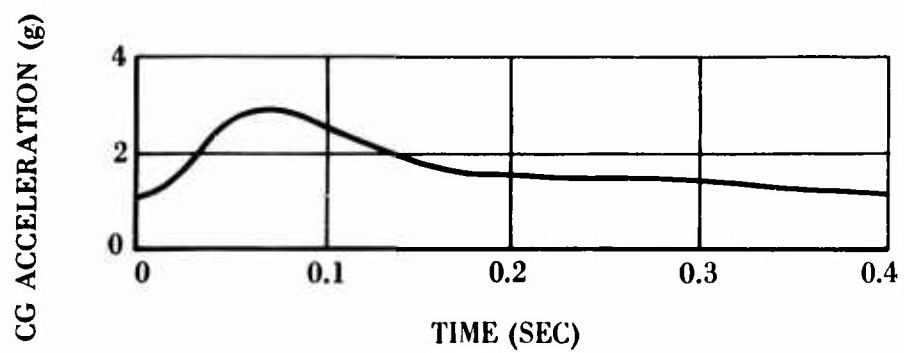for the 18 July Landing.

67

Figure 27. Calculated CG Accelerations During
the 18 July Landing.

Figure 28. Comparison of Measured and Calculated Strut Loads for the 3 August Landing.

69
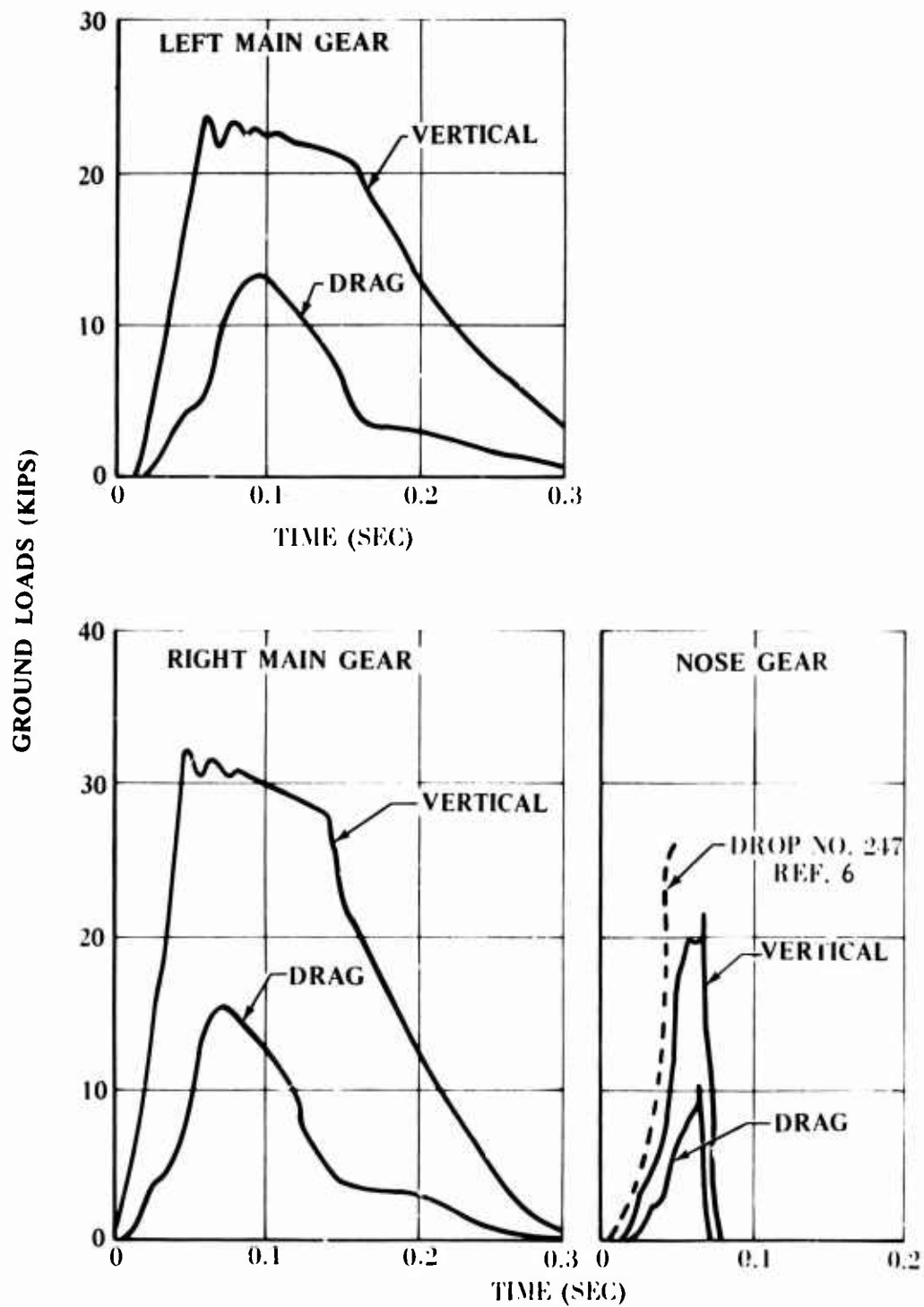
Figure 29. Calculated Ground Loads for the 3 August Landing.
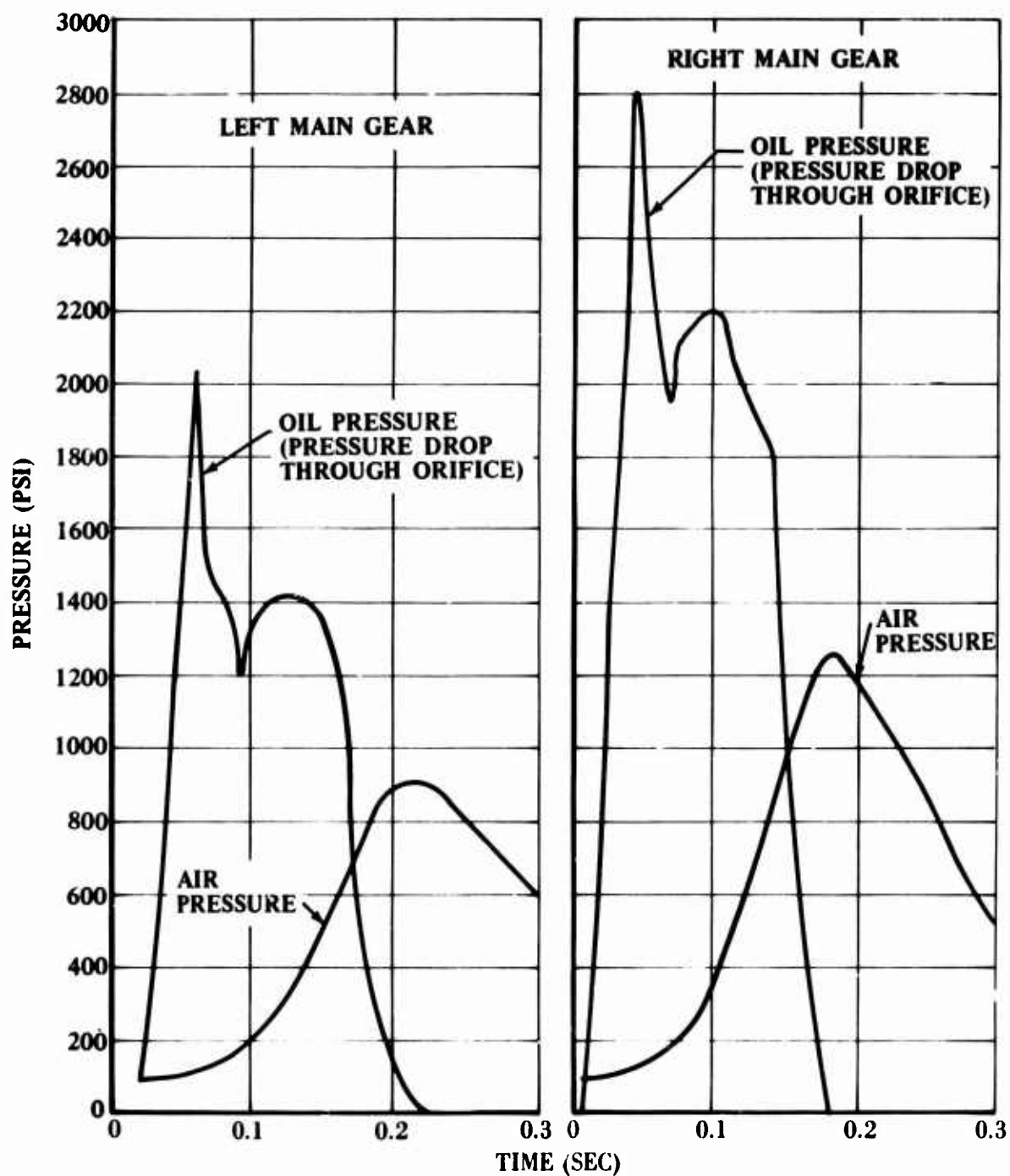
Figure 30.   Calculated Strut Air and Oil Pressures for the
3 August Landing.
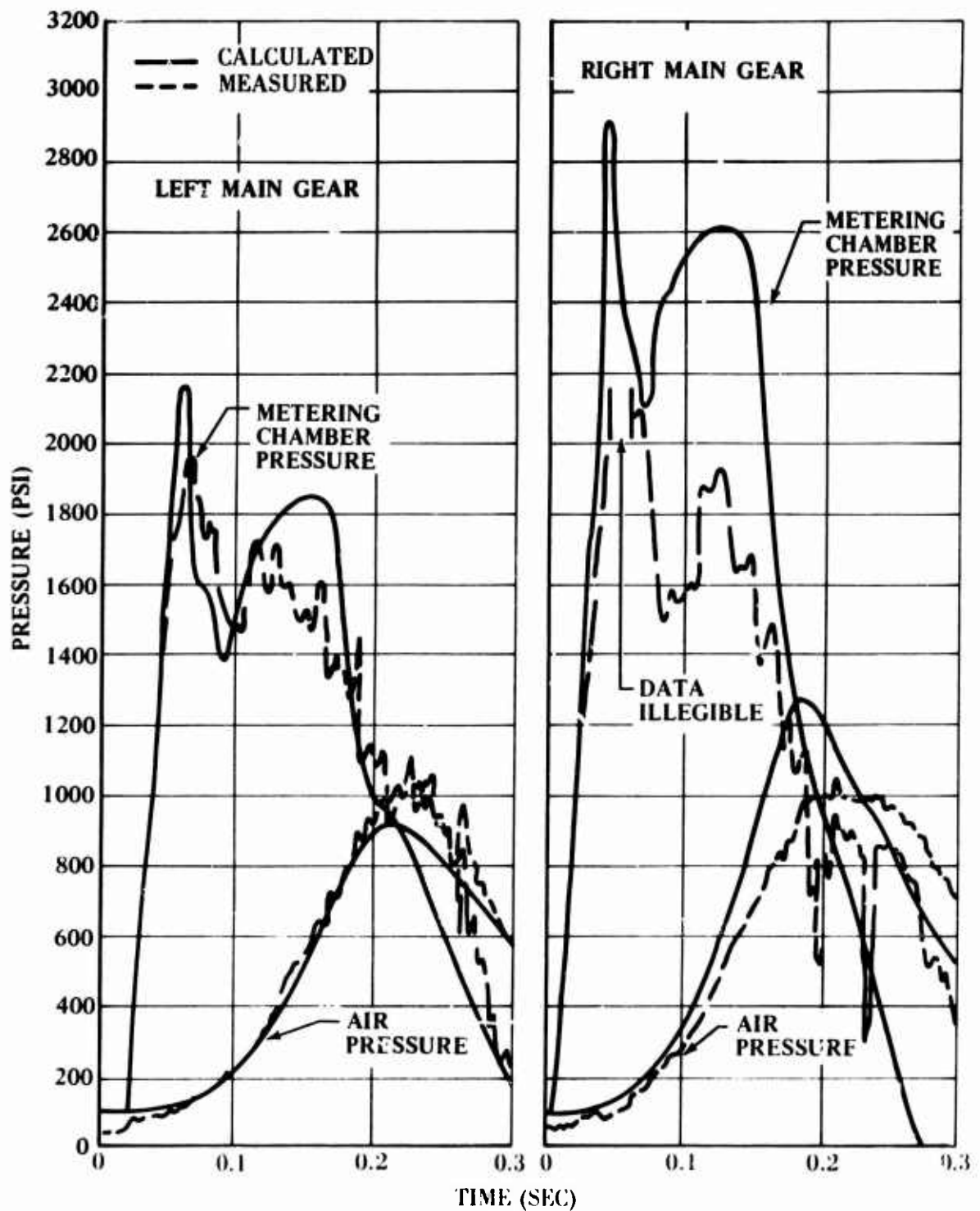
Figure 31. Calculated and Measured Strut Pressures for the 3 August Landing.

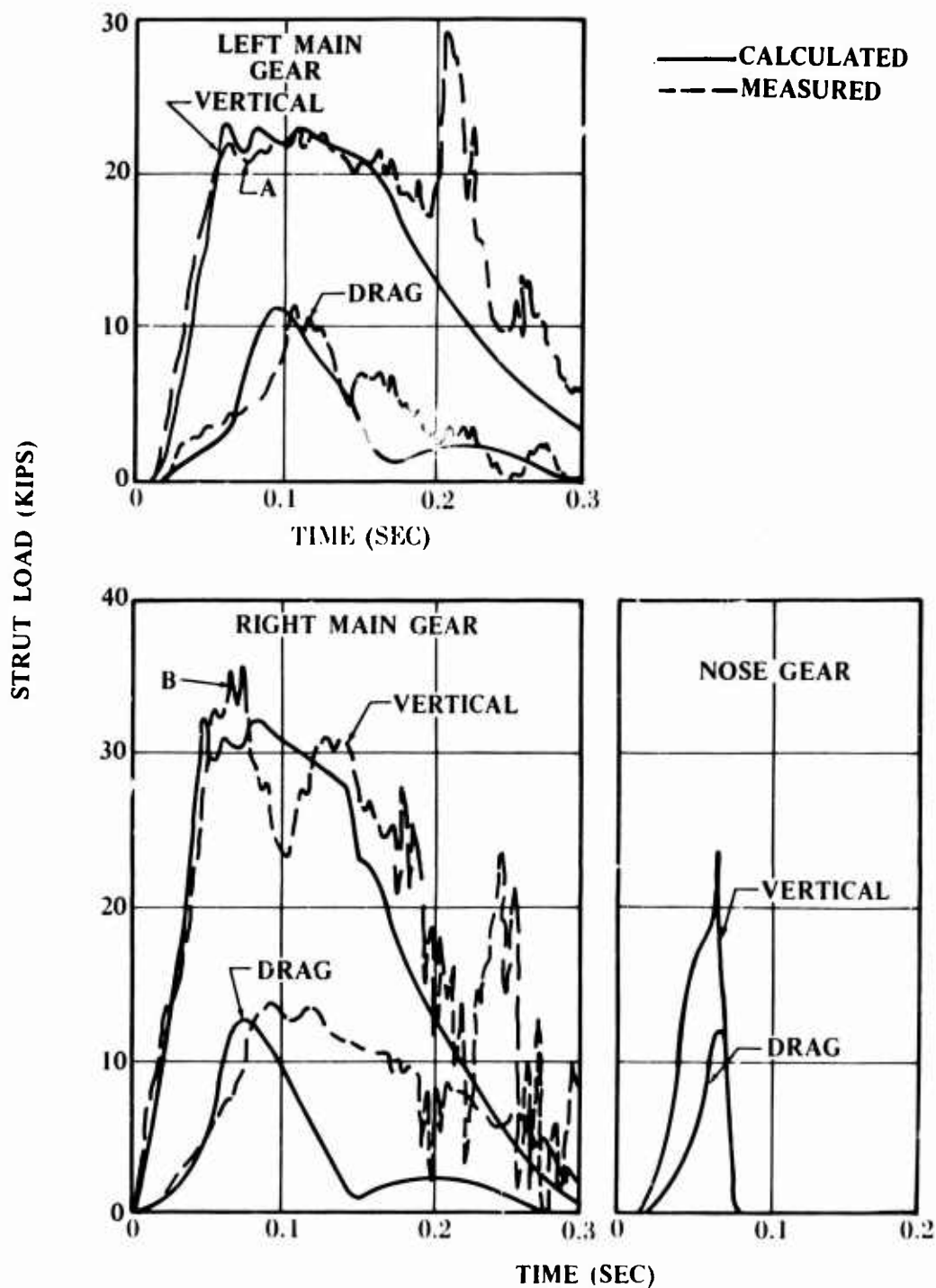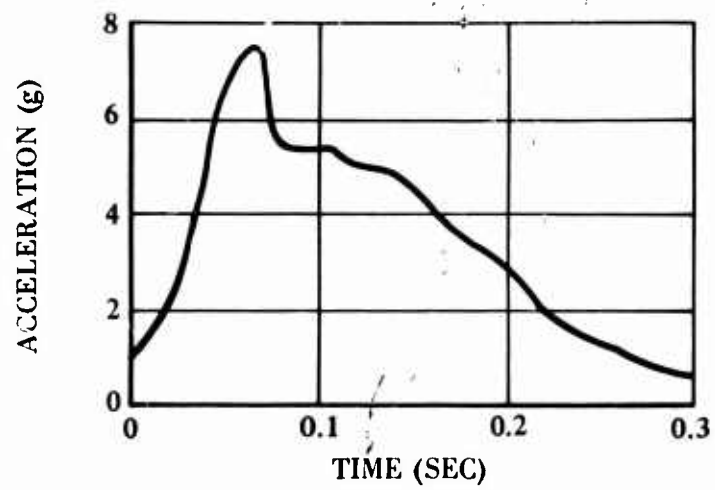Figure 32. Calculated CG Accelerations for the
3 August Landing.
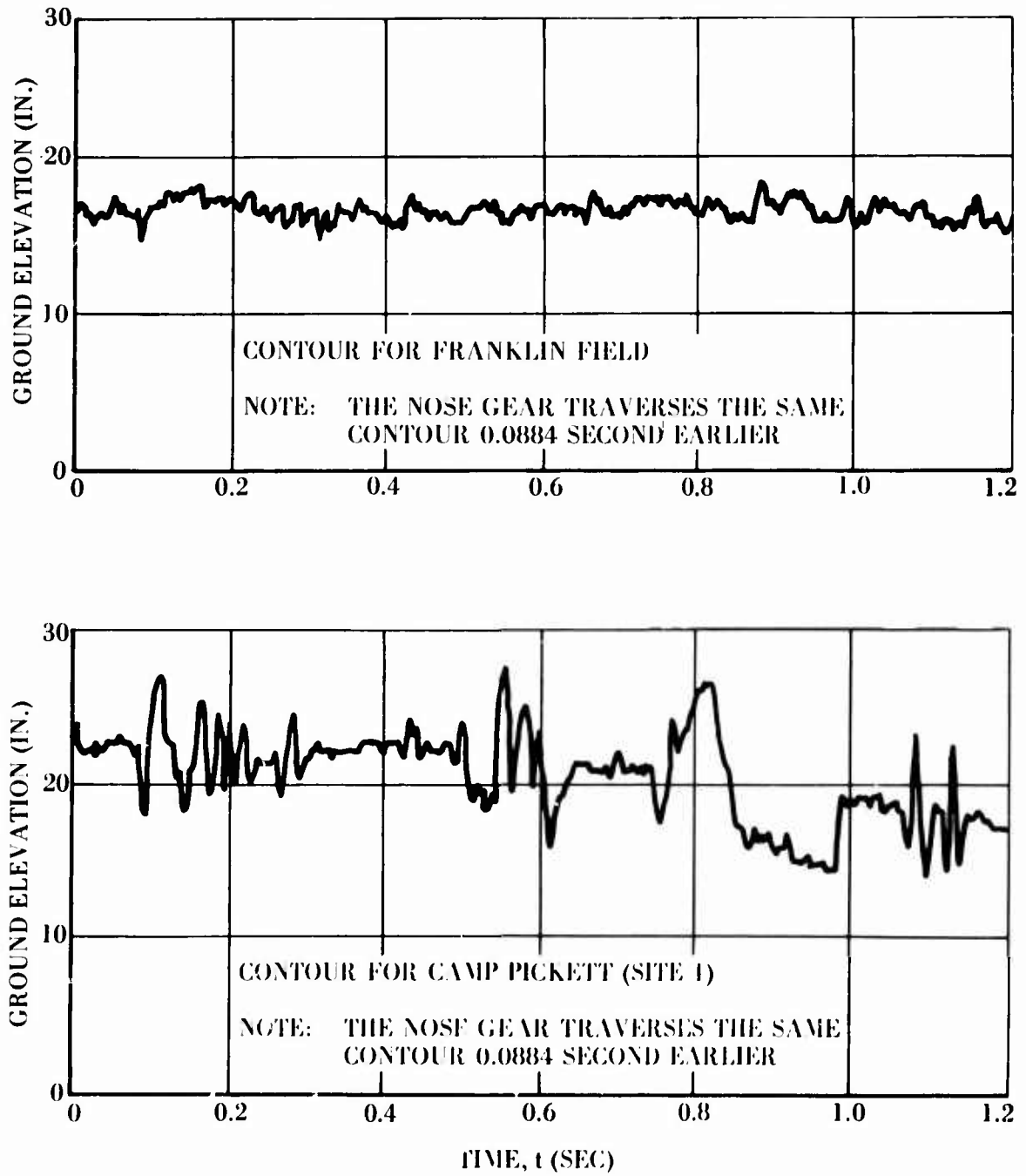
Figure 33.   Ground Elevation Encountered by Main Gear as a
Function of Time After Touchdown for Rough Field
Landings and Rollouts.

74

TRIAXIAL TESTS OF VICKSBURG LOESS SOIL (REF. 4)
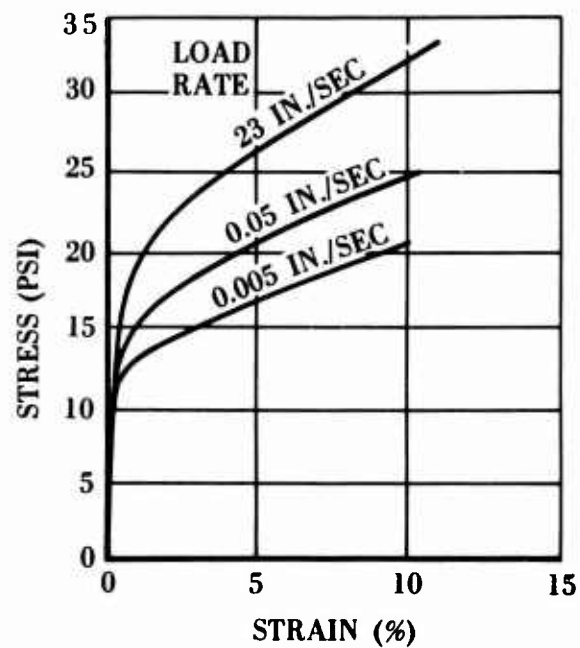
Figure 34.   Stress-Strain Curves for a Soil in Compression.

SOIL
PRESSURE
(p)

P_o

FOOTPRINT
AREA CONSTANT

TIRE BOTTOMING LOAD
P_{TB}
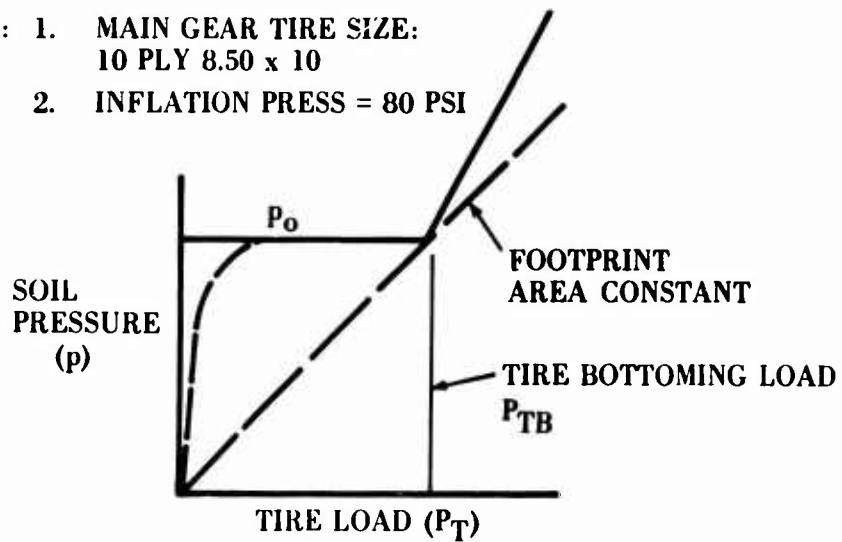
TIRE LOAD (P_T)

Figure 35. Soil Pressure Versus Tire Load.

p vs δ_S

p, P_T

P_{TB}

p vs δ_S

P_T vs δ_S

LEFT MAIN GEAR

δ_{SB}

δ_S

p vs δ_S

P_{TB}

P_T vs δ_S

RIGHT MAIN GEAR

δ_{SB}

δ_S
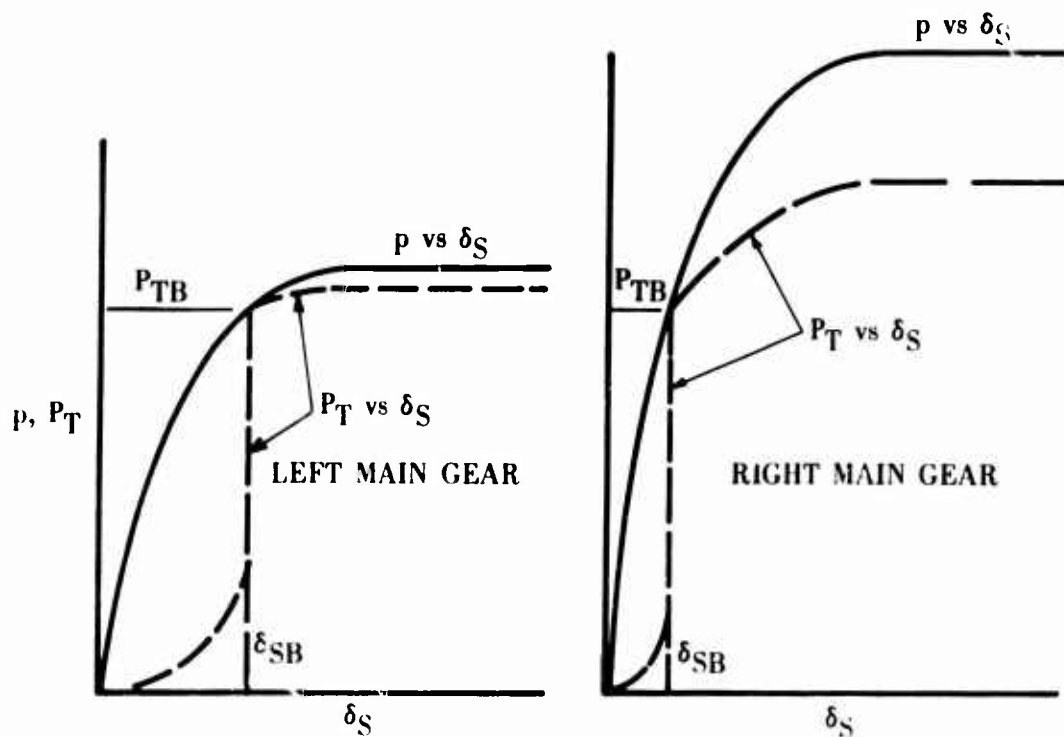
Figure 36. Tire and Soil Load-Deflection Relationships.

76
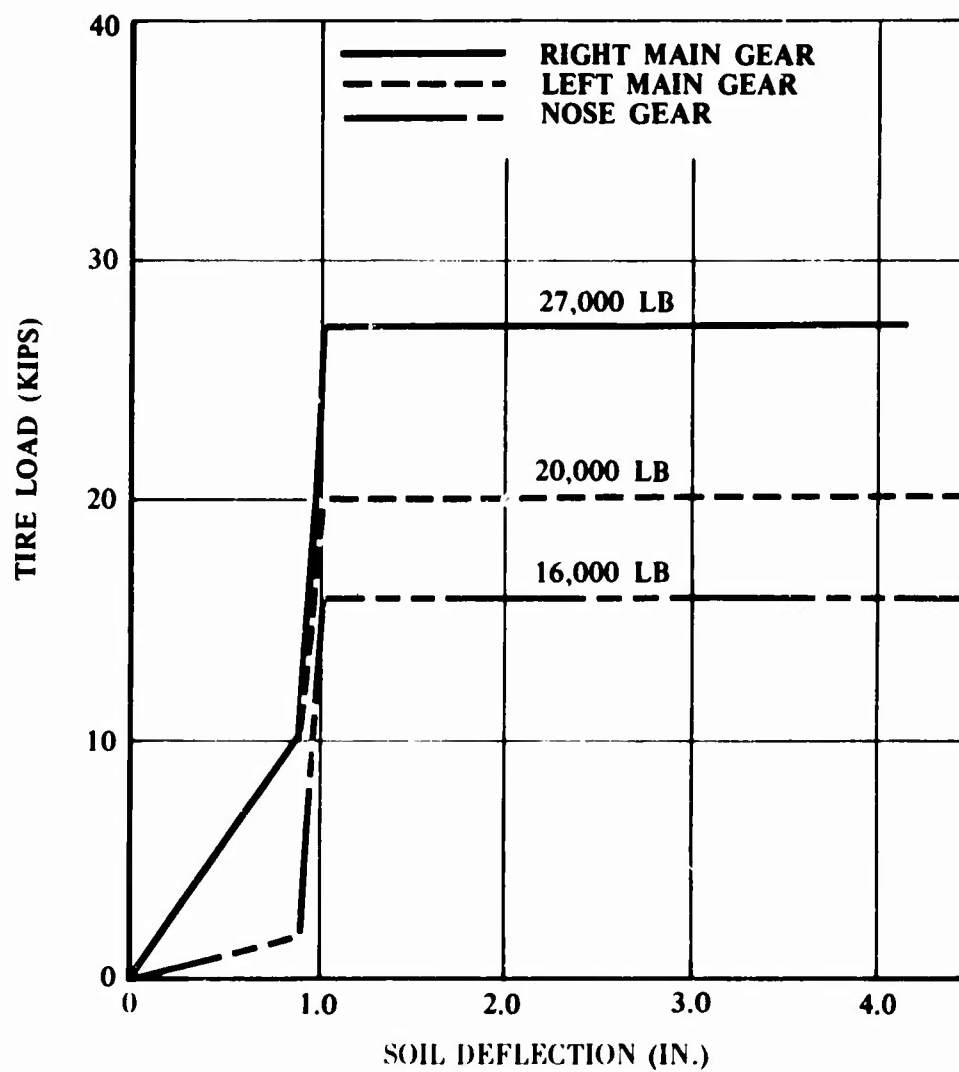
Figure 37. Assumed Relationship Between Tire Load and Soil Deflection.
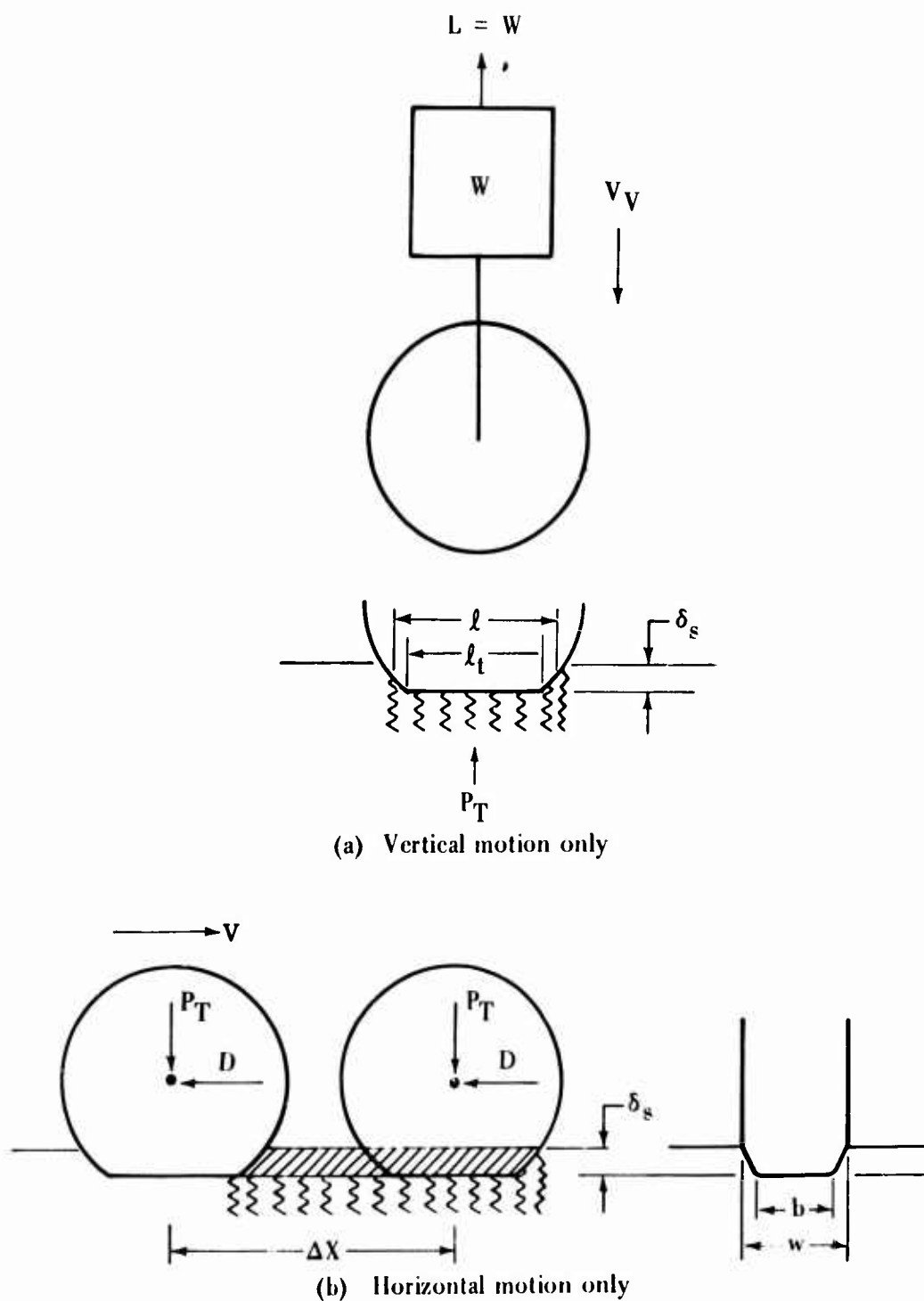
Figure 38.   Mechanical Analogy for Development of
Rolling Resistance in Soft Soil.

LEFT MAIN GEAR   RIGHT MAIN GEAR

18 JULY LANDING – SOD

2 AUGUST LANDING – CONCRETE

3 AUGUST LANDING – SOD
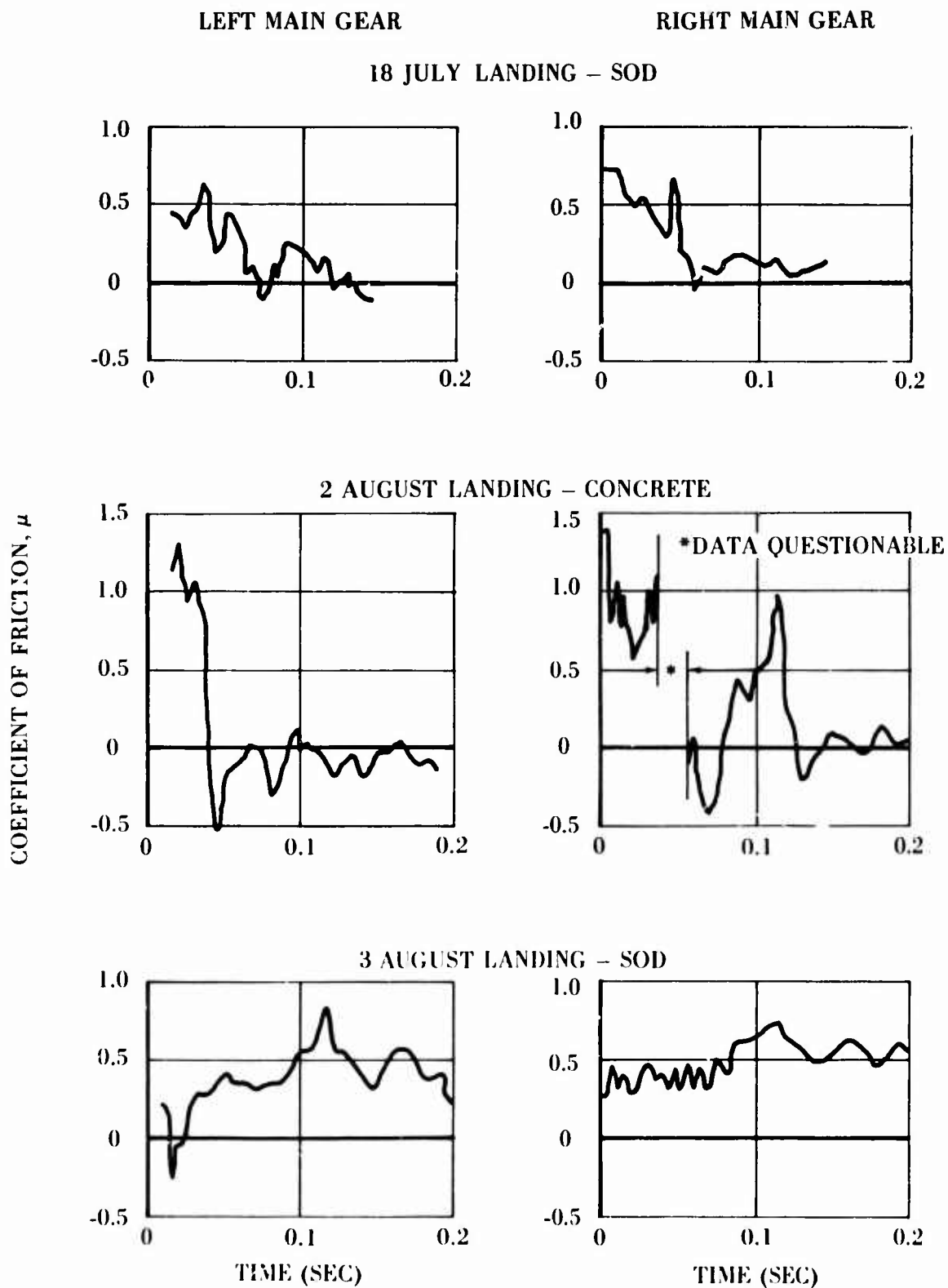
Figure 39.   Total Ground Coefficients of Friction Derived
From Test Data.
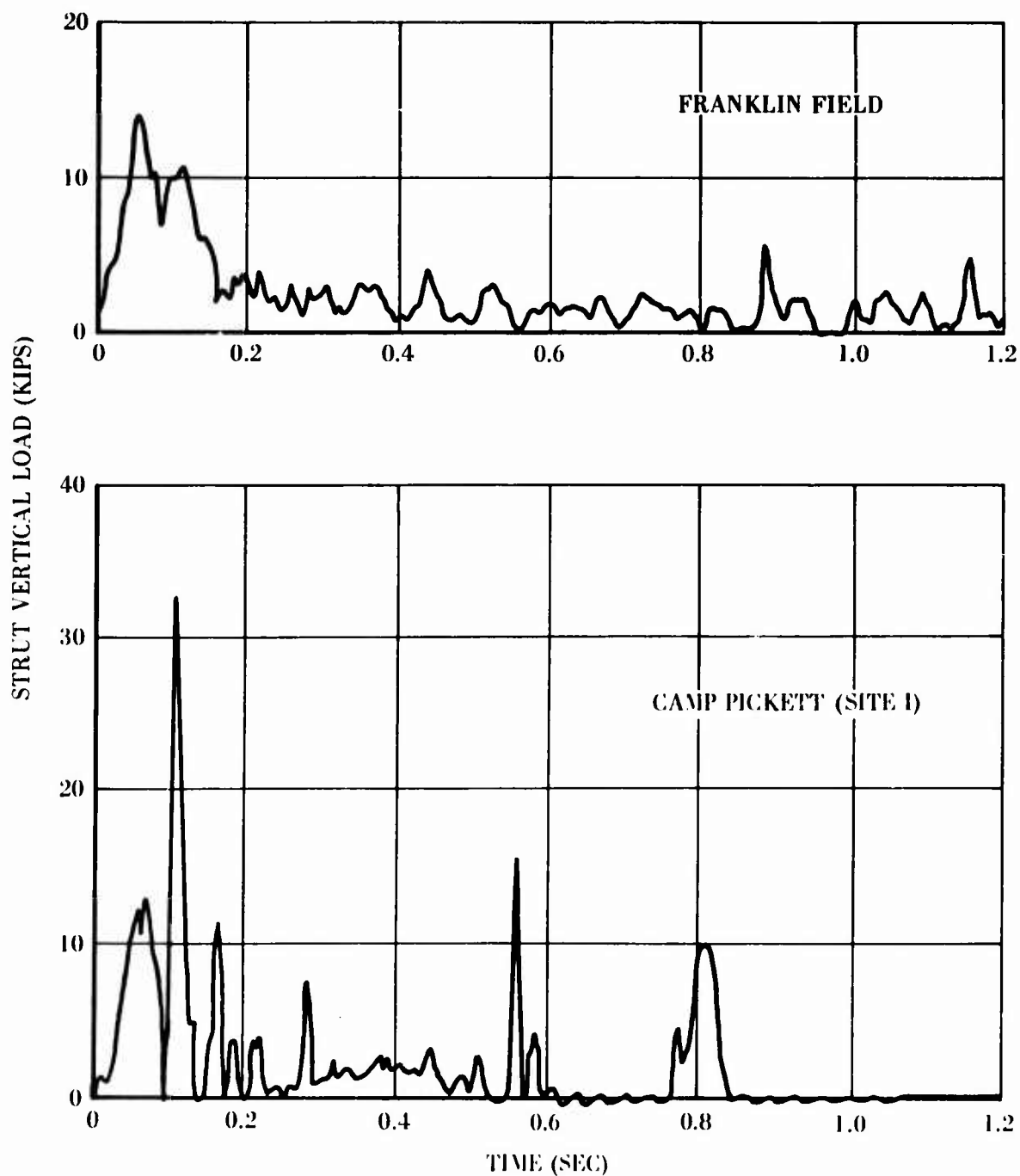
Figure 40. Calculated Main Gear Vertical Strut Loads for
Landings and Rollouts on Rough Terrain.

80
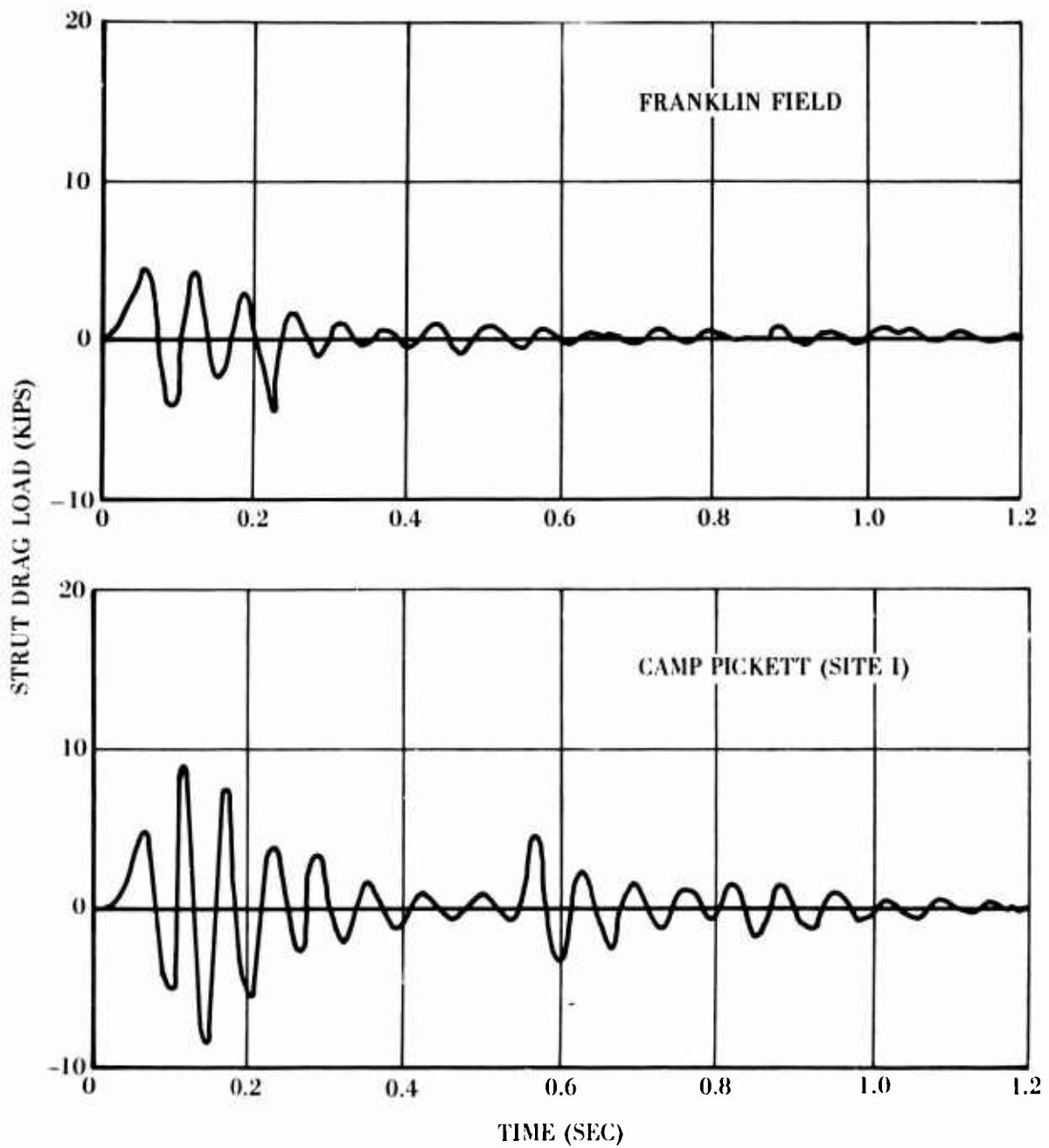
Figure 41.   Calculated Main Gear Strut Drag Loads for
Landings and Rollouts on Rough Terrain.
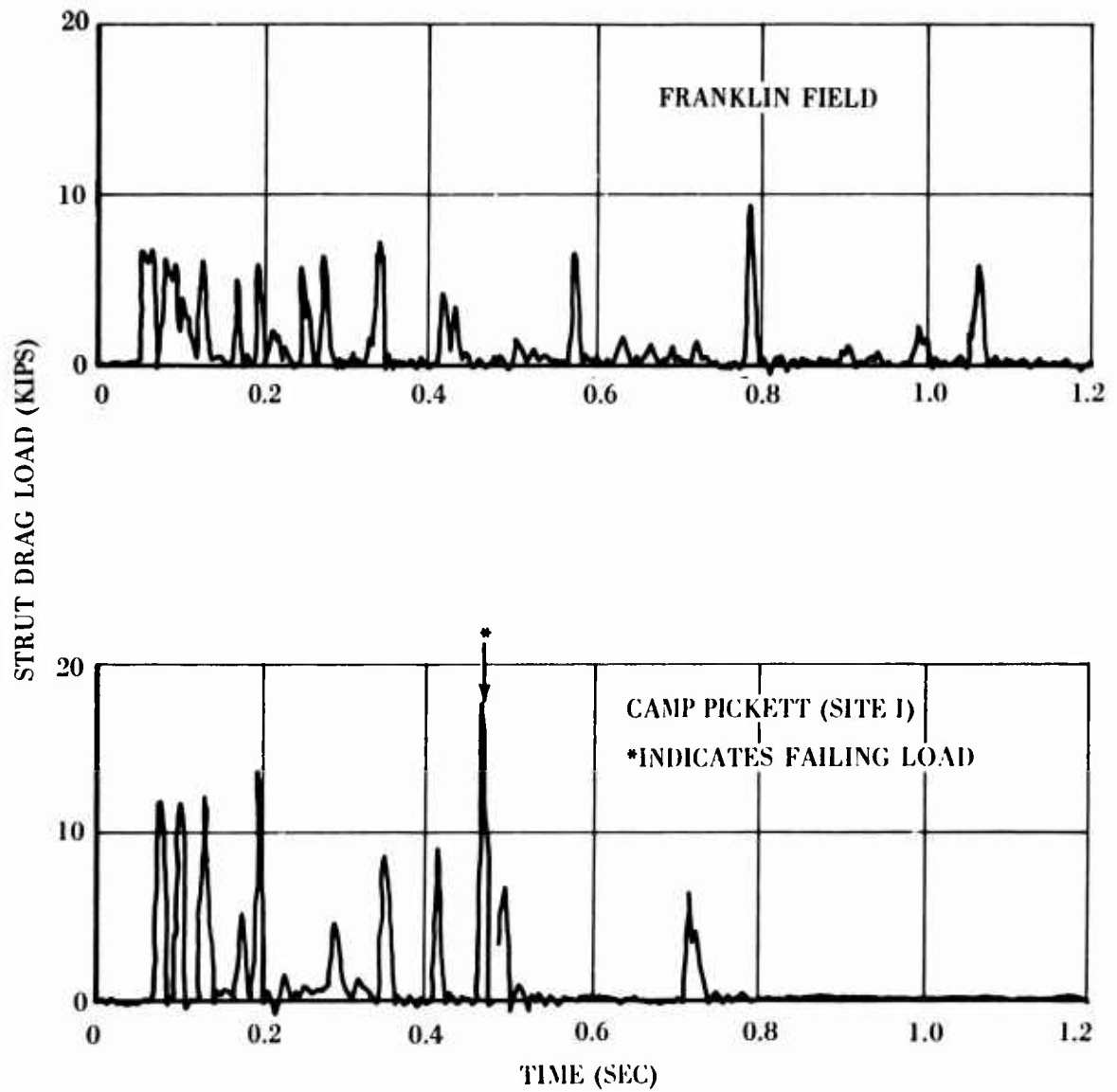
Figure 42. Calculated Nose Gear Vertical Loads for
Landings and Rollouts on Rough Terrain.
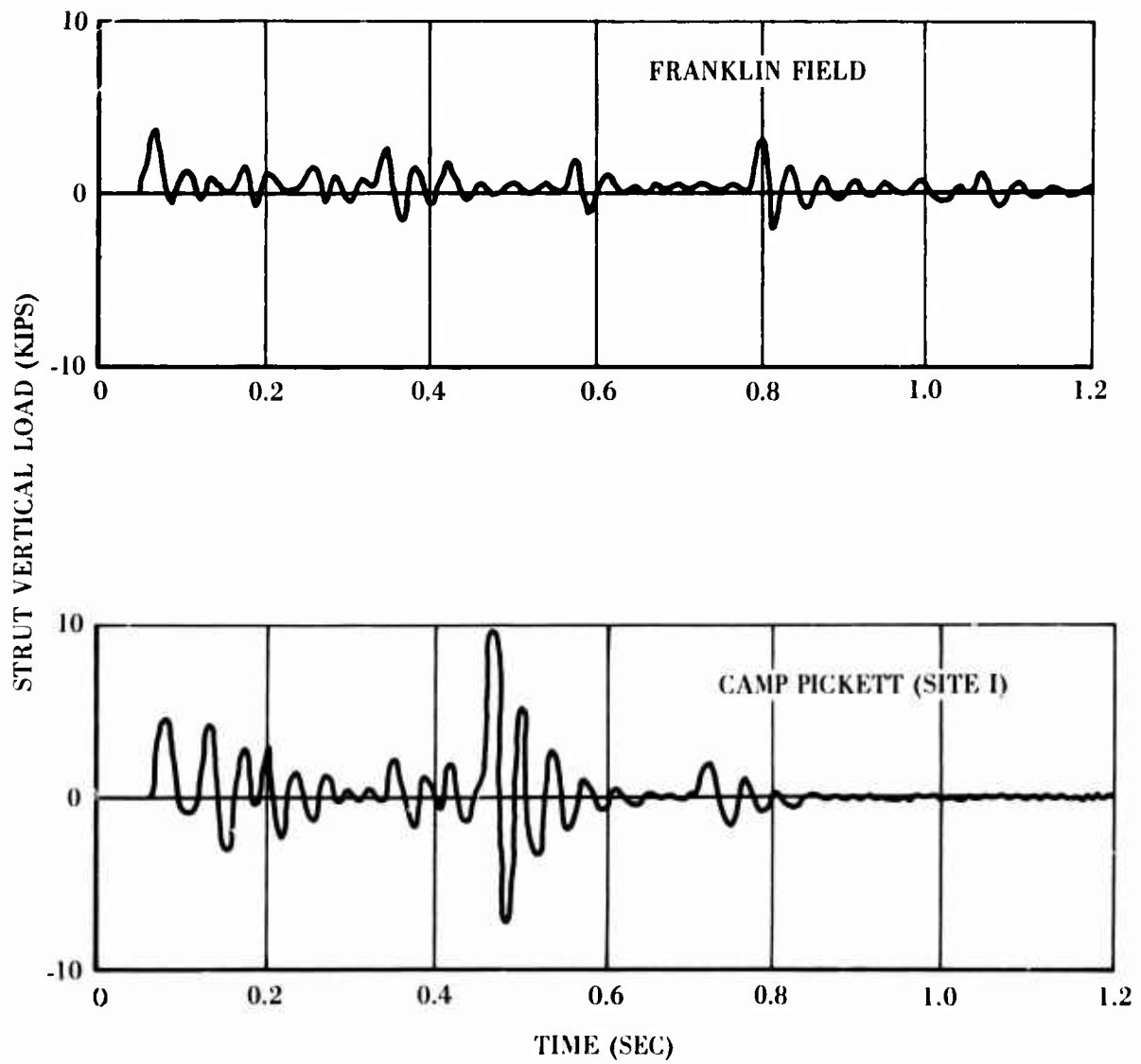
Figure 43.   Calculated Nose Gear Strut Drag Loads for Landings
and Rollouts on Rough Terrain.

83
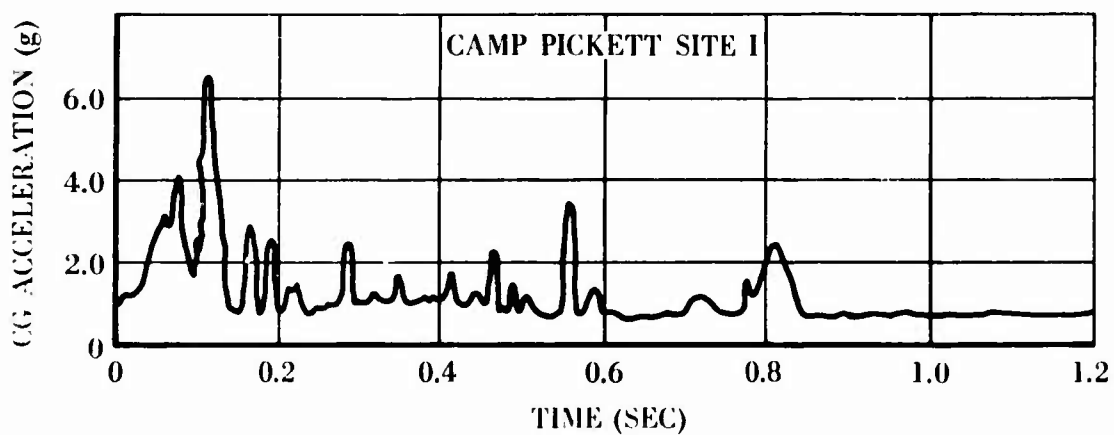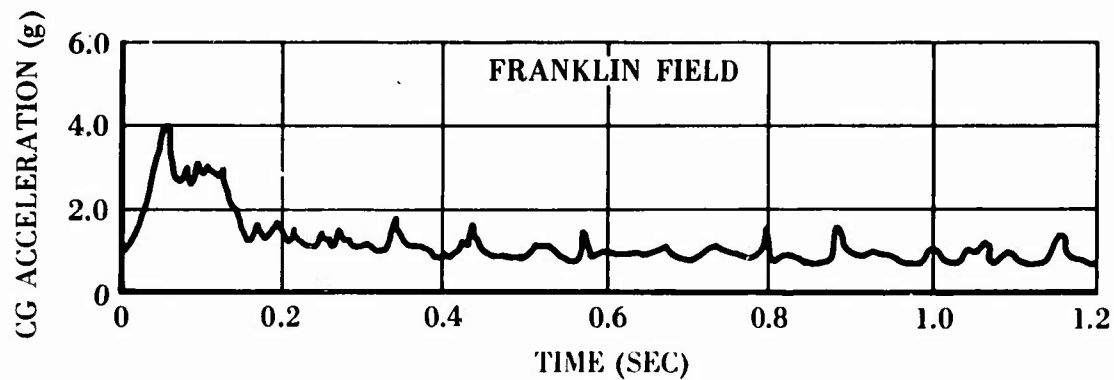
Figure 44. Rigid Body CG Accelerations for Landings
and Rollouts on Rough Fields.

84

COMPARISON OF CALCULATED AND MEASURED LOADS

2 August Landing (see Figures 19 through 23)

For the 2 August landing on concrete, the complexities induced by soil contour and deflection were not present. The behavior of the right gear has been discussed previously, and the correlation shown in Figure 6 is obtained by assuming that not all of the oil had returned below the orifice at the time of touchdown. The general shape of the vertical load curve and several details are similar. With more effort, it is believed that the correlation could have been improved greatly; however, the additional effort was not considered to be worthwhile in view of the untypical gear condition.

The drag load on the right gear was predicted reasonably well; however, there was a secondary frequency in this record and in the drag record of the left gear that was not predicted and that c. itributed to inaccuracy. The second mode is believed to come from   sion of the fork, since the fork is not symmetrical, but extensive efforts to include this motion did not produce the desired results.

Peak vertical loads on the left main gear and the nose gear and the drag load on the nose gear were predicted well.

18 July Landing (see Figures 24 through 27)

These loads were calculated on the basis that the ground was hard and smooth. Thus, a $\mu_S = 0.3$ and a $\mu_R = 0.2$ were used, but no soil deflection was computed. No permanent set or rutting of the soil was evident after this landing.

The right main gear peak load and the drag load were predicted with good accuracy. The secondary mode mentioned above did not appear in the right gear drag but did appear in the left.

The shape of the calculated vertical load curves does not agree well with the shape of the measured vertical load curves. It is believed that a significant portion of the discrepancy can be attributed to the terrain contour, which was not included and could not be included in the calculations.

The only test data available for the nose gear was the point of touchdown, which the calculations predicted satisfactorily. The nose gear loads are insignificant. The lack of test data probably resulted from insufficient amplitude (gain) on the nose gear load channels.

3 August Landing (see Figures 28 through 32)

The correlation between the calculated and measured left main gear loads shown in Figures 28 and 30 is remarkable in view of the complexities involved. The correlation for the right main gear was not nearly as successful, especially for the drag load. Lack of agreement on the right gear is considered to be caused by one or more of the following:

1. The right gear may have been operating in a nonstandard manner as in the 2 August landing (see page 55).

2. The model of the soil may be inadequate for landings in which the tire load far exceeds the bottoming load.

3. The rolling coefficient of friction of a tire that has far exceeded its bottoming load may be substantially greater than that for an unbottomed tire.

There are insufficient data to determine the exact cause of the discrepancy; however, work done in connection with the TA-4F airplane (Reference 5) lends support to the view that high rolling coefficients will be obtained for a tire that is subjected to a load far in excess of the bottoming load, even on concrete. In the present problem, the tire bottoms at about 20,000 pounds, and the load stays above this figure from t = 0.04 to 0.20. The left gear also exceeds the bottoming load, but only by a small amount.

The calculated nose gear loads are shown in Figure 28. The sudden drop in vertical load at t = 0.07 second is the simulated failure. The vertical nose gear loads measured in drop tests at 19.6 feet per second (Reference 6) are superimposed on Figure 29. The drop-test results confirm the extremely rapid rise in vertical load with time which was predicted by the computer.

Figure 45 shows the calculated strength diagram of the nose gear for strokes of 3 inches and 9 inches. With a stroke of 9 inches, the outer cylinder is more critical than the piston until a vertical load of more than 27,000 pounds is applied. At 3 inches of stroke, the piston is critical. The piston strength, together with the calculated loads, is replotted on Figure 46. This figure indicates that failing loads were applied at S = 2.0 inches. This is not consistent with the location of the fracture, which was at a position corresponding to a stroke of 9 inches. It is surmised that a small finite amount of time was required for the loads experienced at S $\cong$ 2 to produce deflections corresponding to failure

and that during that time, the gear continued to stroke. It should be re-membered that the strength diagram is a static strength diagram, and the deflections incorporated therein correspond to slowly applied loads.
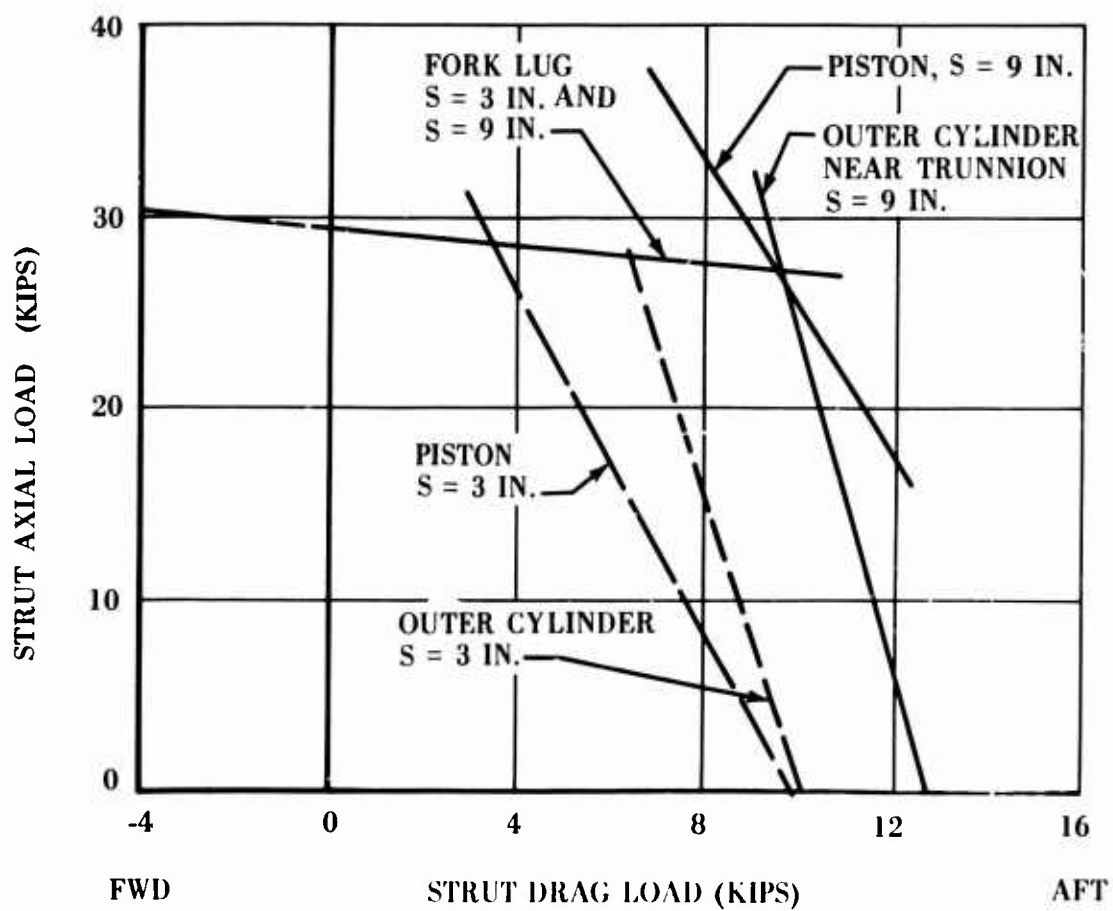
Figure 45. Calculated Nose Gear Strength Diagram.
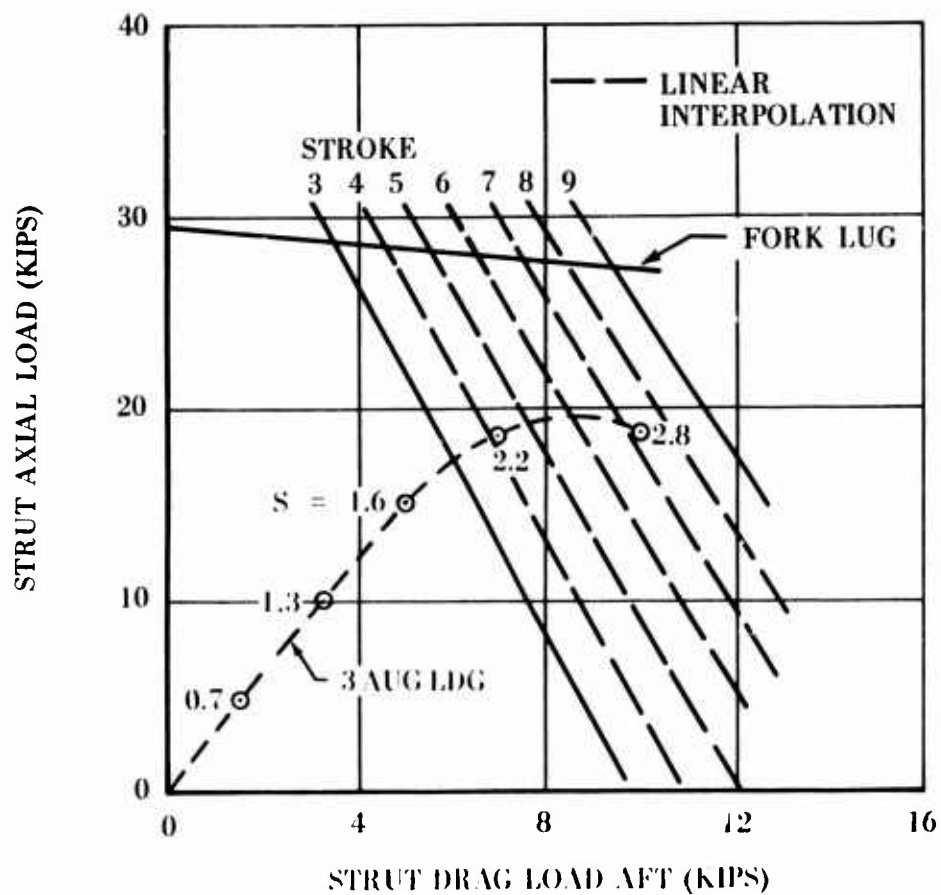
Figure 46. Calculated Nose Gear Piston Strength Diagram Showing Calculated Loads Experienced During 3 August Landing.

CONCLUSIONS

The dynamic loads computing program used in this investigation was able to predict the gear loads from flight-test landings with about the same accuracy demonstrated in an earlier investigation involving loads from moving drop tests (Reference 3). This accuracy is estimated to be within ±10 percent for the peak loads. Many, but not all, of the peculiarities of the shapes of the individual load curves were duplicated.

The differences between test and calculated loads illustrated herein are not all attributable to errors or inappropriate assumptions in the mathematical representation of the airplane. Differences also result from instrumentation errors, effects of ground roughness, and lack of precise knowledge regarding the initial conditions. The ability to obtain the noted accuracy with a test vehicle subjected to aerodynamic forces and having 6 degrees of freedom represents a considerable advancement over the previously used 2-degree-of-freedom procedures.

It is believed that the greater part of any errors attributable to the computing program still lies in the detailed dynamic representation of the gears and in the duplication of the ground-tire interaction. More precise knowledge of the internal bearing friction, the variation of orifice coefficients with Reynolds number, and the polytropic compression exponent for nitrogen is needed. Although a satisfactory correlation was made in the 3 August landing by assuming a soil load-deflection relationship, basic soil data and a theory from which such load-deflection relationships can be derived need to be developed.

Much remains to be done in the area of side load prediction and measurement. While the mathematical statement of the torsional motion of the strut and the ground-tire reaction to yaw has been well developed, experimental verification of the accuracy of the representation is restricted by difficulties encountered in the measurement of side loads. These difficulties arise from the fact that high vertical loads and strut bending and torsional deflections combine to induce side load components of appreciable magnitude. Because of the importance of deflections, a static calibration gives, at best, a first approximation of the loads existing in the dynamic situation. No satisfactory procedure has been developed to provide a dynamic calibration for side loads.

The calculations predicted a failure of the nose gear on the 3 August landing. While the calculated stroke at failure appears to be inconsistent with the observed facts, this is not a matter of great significance.

The maximum total ground coefficient of friction measured on the main gears during the 3 August landing was 0.85. It is believed that the use of a rolling coefficient of 0.85 in the design of the nose gear would have been sufficient to prevent failure. In Reference 2, a maximum rolling coefficient of 1.0 is recommended for design. In light of the present test results, the recommended value of 1.0 seems to be correct if it is intended that strength be incorporated for the case in which soil failure occurs. Otherwise, the value would be excessively conservative.

The 3 August landing was successfully simulated on the computer by applying some approximate relationships describing the tire-soil interaction. The analysis provided an explanation for the disastrous results of the 3 August landing and emphasized the dangers of exceeding the tire-bottoming load when landing on soft soil.

The computed loads developed in this study from landings and rollouts on rough terrain gave a measure of what constitutes "rough" terrain as far as the OV-1 airplane is concerned. The Camp Pickett site contained roughness that was in excess of the OV-1 gears' strength capabilities. The Franklin field roughness appeared to be within the gears' capabilities.

RECOMMENDATIONS

In order to calculate the dynamic loads more accurately, knowledge of the following fundamental interior gear phenomena and parameters is needed: (1) the bearing friction at high contact pressures, (2) the value of the polytropic exponent for nitrogen compression at different compressive speeds, (3) the effects on gear characteristics of the dissolving and mixing of nitrogen in oil, and (4) the orifice coefficients as a function of orifice shape and Reynolds number. While values for these parameters are known for average conditions, they are not adequately established for extreme conditions such as were encountered in the 19-foot-per-second landing investigated herein or in design drops for carrier-based aircraft. Therefore, it is recommended that research be conducted to obtain the necessary information.

The rolling coefficient of friction for fully compressed tires is not known and should be determined if calculations are to be made for limiting conditions.

The soil model used herein for correlation with the 3 August landing probably does not have general applicability because it has been over-simplified. It is recommended that further work be done to improve the soil model and to provide basic soil data necessary for application of the model in dynamic calculations.

It is recommended that rolling drop tests be conducted during which the OV-1 gear, or a similar gear, is dropped on soils of varying degrees of softness, and that attempts be made to compute the loads by means of a dynamic loads program that incorporates a soil model. It is also recommended that this same test program be extended to measure the loads developed on the gear when it traverses terrain with random roughness and that these loads be compared to computed loads.

It is recommended that mathematical models be made for several gear concepts having strong rough-terrain capability and that these gears be landed and taxied mathematically on typical rough terrain to determine their relative tolerance to ground roughness. On the basis of these results, it is recommended that a gear be built which incorporates the features of the best rough-terrain gear model, and that this gear be proved by rolling drop tests on soft soil and over rough contours.

91

LITERATURE CITED

1. INVESTIGATION OF TERRAIN ROUGHNESS, TRECOM Technical Report 64-19, U.S. Army Transportation Research Command,* Fort Eustis, Virginia, May 1964.

2. Allen, F. C., Mosby, L. B., and Rehder, D. M., A STUDY OF ROUGH-TERRAIN-INDUCED STRUCTURAL LANDING LOADS (PHASES I AND II), Douglas Aircraft Company; TRECOM Technical Report 63-68, U.S. Army Transportation Research Command,* Fort Eustis, Virginia, December 1963.

3. Allen, F. C., and Mosby, L. B., A STUDY OF ROUGH-TERRAIN-INDUCED STRUCTURAL LANDING LOADS (PHASE III), Douglas Aircraft Company; USAAML Technical Report 65-5, U.S. Army Aviation Materiel Laboratories,* Fort Eustis, Virginia, May 1965, AD 616734.

4. Healy, K. A., RESPONSE OF SOILS TO DYNAMIC LOADINGS - REPORT NO. 15, UNDRAINED STRENGTH OF SATURATED CLAYEY SILT, Research Report 63-19, Massachusetts Institute of Technology, Cambridge, Massachusetts, March 1963.

5. Allen, F. C., Heimbaugh, R. M., and Larson, D. H., DYNAMIC GROUND LOADS CORRELATION - MODEL TA-4F (VOLUME I), Report DAC-33248, Douglas Aircraft Company, Long Beach, California, December 1966.

6. Morrison, A., RESULTS OF NOSE GEAR DYNAMIC TESTS - MODEL YAO-1, Report 3934.23, Grumman Aircraft Engineering Corporation, Bethpage, Long Island, New York, December 1960, with Revisions through May 1961.

7. AUTOMATIC RUNWAY PROFILE MEASURING INSTRUMENTATION AND RUNWAY PROPERTIES, PART III - BASE SURVEYS, WADD-TR-60-470, Wright-Patterson Air Force Base, Ohio, July 1963.

8. SOD AND MATTED LANDING SURFACE ROUGHNESS CHARACTERISTICS, AFFDL Technical Memorandum FDDS-TM-64-32, Wright-Patterson Air Force Base, Ohio, December 1964.

*Now Eustis Directorate, U.S. Army Air Mobility Research and Development Laboratory.

APPENDIX I
EQUATIONS OF MOTION

LIST OF SYMBOLS

THEORY	FORTRAN		UNIT
A	A	pitch attitude of airplane	rad
a	AA	vertical motion of unsprung mass, measured along strut center line	in., sec.
A_{BRG}	ABRG	vertical distance from lower bearing to the unsprung mass cg when the strut is fully extended, measured along strut center line	in.
A_D	ADRAG	aerodynamic drag force at aerodynamic center	lb
$\{AIR\}$		column matrix of aerodynamic forces	
AIR_a		pitching aerodynamic moment about the airplane cg	lb-in.
AIR_θ		rolling aerodynamic moment about the airplane cg	lb-in.
AIR_f		longitudinal aerodynamic forces in airplane body axis system	lb
AIR_h		vertical aerodynamic force in airplane body axis system	lb
A_L	ALIFT	aerodynamic lift force at aerodynamic center	lb
A_a	APITCH	aerodynamic pitching moment about the aerodynamic center	lb-in.

93

THEORY	FORTRAN		UNIT
A_{nn}	ANN	annular distance between the metering pin and the orifice	in.
A_p	AP	sectional area of metering pin	in.^{2}
A_{POD}	APOD	sectional area of piston based on outside diameter at lower bearing	in.^{2}
[AM]		matrix of coefficients for calculating airplane accelerations from the aerodynamic forces	lb, in., sec
A_R	AR	sectional area of rebound chamber at the piston lower bearing	in.^{2}
A_S	AS	total cross-sectional area of rebound chamber orifices	in.^{2}
A_{SPL}	ASPL	sectional piston area at the upper bearing, including splines	in.^{2}
[AT]		matrix of coefficients for calculating airplane rigid body accelerations from gear forces	lb, in., sec
A_1	A1	sectional area of gear oil chamber without reduction for metering pin	in.^{2}
A_0	A0	orifice area without reduction for metering pin	in.^{2}
B_W	B	tire spring constant in side direction	lb/ft
b	BB	lateral motion of unsprung mass, measured perpendicular to strut center line	in., sec

THEORY	FORTRAN		UNIT
$\overline{b}$	BBAR	elastic motion of the unsprung mass relative to the gear attach point in the lateral direction, measured perpendicular to strut center line	in., sec
B_{BRG}	BBRG	vertical distance between upper and lower bearings when strut is fully extended, measured along strut center line	in.
C	CHORD	mean aerodynamic chord length of wing	in.
$\overline{C}$	CBAR	structural damping coefficient for strut in the drag direction	$\dfrac{\text{lb-sec}}{\text{in.}}$
C_β	CBETA	structural damping coefficient for strut twisting	lb-in., sec
C_D	CD	hydraulic fluid orifice coefficient during strut compression, for strut orifice	
C_{DEL}	CDEL	constant used in calculating soil deflection curve	
C_{D_B}	CDB	airplane aerodynamic drag coefficient	
$C_{D_{\delta e}}$	CDDE	change in aerodynamic drag coefficient of elevator per radian of elevator deflection	
$C_{D_{iH}}$	CDEIH	change in aerodynamic drag coefficient of horizontal tail per radian of tail deflection	
C_{EXP}	CEXP	increase in piston volume per unit pressure	$\dfrac{\text{in.}^3}{\text{psi}}$
C_F	CF	structural damping coefficient in the fork	lb/in./sec

THEORY	FORTRAN		UNIT
C_{FORK}	CFORK	structural damping coefficient in the gear fork	$\dfrac{lb\text{-}sec}{in.}$
C_G	GDAMP	damping coefficient used for flexible ground	lb, in., sec
C_{L_B}	CLB	airplane aerodynamic lift coefficient	
$C_{L_{\delta e}}$	CLDE	change in aerodynamic lift coefficient of the elevator per radian of elevator deflection	
$C_{L_{iH}}$	CLEIH	change in aerodynamic lift coefficient of the horizontal tail per radian of tail deflection	
C_{M_B}	CMB	airplane aerodynamic moment coefficient	
$C_{M_{\delta e}}$	CMDE	change in aerodynamic moment coefficient of the elevator per radian of elevator deflection	
$C_{M_{iH}}$		change in aerodynamic moment coefficient of the horizontal tail per radian of tail deflection	
C_{M_q}	CMQ	change in airplane aerodynamic pitching moment coefficient per rad/sec of pitching rate	
C_{M_R}	CMR	change in airplane coefficient of rolling moment per rad/sec of rolling rate	
C_S	CS	structural damping coefficient for the strut in the lateral direction	$\dfrac{lb\text{-}sec}{in.}$
C_T	CT	vertical tire deflection	in.
	CTN	maximum vertical tire deflection	in.

THEORY	FORTRAN		UNIT
d	DD	longitudinal motion of unsprung mass, measured perpendicular to strut center line	in., sec
$\bar{d}$	DBAR	elastic motion of the unsprung mass relative to the gear attach point in the longitudinal direction, measured perpendicular to strut center line	in., sec
D_{AMP}	DAMP	nonlinear stiffness coefficient for use in the fork equations of motion	$lb/in.^2$
D_{BTM}	DBTM	drag constant used after tire bottoming for flexible ground	
D_C	DCNST	drag coefficient used for flexible ground	
D_{EL}	DEL	total deflection of ground plus tire	
D_{FA}	DFA	elastic deformation of the strut in the longitudinal direction due to a vertical load	in.
D_{CG}	DCG	displacement of airplane cg perpendicular to the runway	in.
D_P	DP	metering pin diameter	in.
[DQ]		matrix of coefficients for calculating airplane modal accelerations from modal velocities	1/sec
E_B	EB	lateral distance from strut center line to cg of unsprung mass, measured perpendicular to strut center line, + outboard	in.

97

THEORY	FORTRAN		UNIT
E_D	ED	longitudinal distance from strut center line to cg of unsprung mass, measured perpendicular to strut center line, + forward	in.
E_L	EL	vertical distance from gear attach point to cg of the unsprung mass, strut fully extended; measured along strut center line	in.
E_R	ER	factor used to determine rolling radius of tire	
E_X	EX	lateral distance strut joggles around wheel away from strut center line	in.
e	EE	motion of a fork, perpendicular to the fork	in., sec
$\{F\}$		column matrix of gear forces acting on the airplane	
F	ANGF	angle fork makes with strut center line	rad
f	HATF	longitudinal motion of airplane cg, in airplane body axis system	in., sec
F_A	FA	vertical reaction force in the strut, acting along strut center line	lb
F_B	FB	lateral reaction force in the strut, acting perpendicular to strut center line	lb
F_D	FD	longitudinal reaction force in the strut, acting perpendicular to strut center line	lb

THEORY	FORTRAN		UNIT
F_E	FE	reaction force in fork acting perpendicular to the fork	lb
FEW	FEW	fraction of unsprung mass that is below knuckle of piston	
F_f	FHATF	longitudinal gear forces acting on the airplane, acting in airplane body axis system	lb
F_h	FHATF	vertical gear forces acting on airplane	lb
F_L	FANGS	reaction side bending in the strut	lb-in.
F_{TORQ}	FTORQE	normal bearing load applied at the splines	lb
F_x	FX	longitudinal ground forces, acting perpendicular to strut center line	lb
F_y	FY	lateral ground forces, acting perpendicular to strut center line	lb
F_z	FZ	vertical ground forces, acting parallel to strut center line	lb
F_α	FHATF	gear-induced pitching moment acting on the airplane	lb-in.
F_θ	FHATF	gear-induced rolling moment acting on the airplane	lb-in.
F_{1TOT}	F1TOT	total normal bearing force applied at the upper strut bearing	lb
F_{2TOT}	F2TOT	total normal bearing force applied at the lower strut bearing	lb

THEORY	FORTRAN		UNIT
g	386.088	acceleration due to gravity	in./sec^2
G_δ	GDEL	elastic motion of flexible ground	in.-sec
G_M	GMASS	mass used in the dynamic equations of flexible ground motion	lb-sec^2/in.
h	HATF	vertical motion of airplane cg, in airplane body axis system	in.,sec
I_β	IBETA	yawing moment of inertia of unsprung mass about strut center line	lb-sec^2-in.
I_R	IR	pitching moment of inertia of wheel	lb-sec^2-in.
K_β	KBETA	structural stiffness coefficient for strut twisting	in.-lb/rad
K_E	KE	structural stiffness of the fork	lb/in.
K_1	K1	longitudinal deflection of the strut due to a unit vertical load	in./in.-lb
K_{22}	K22	structural stiffness coefficient for strut in the lateral direction, strut fully extended	lb/in.
K_{23}	K23	change in stiffness coefficient of strut in the lateral direction per inch of vertical strut movement	$\frac{\text{lb/in.}}{\text{in.}}$
K_{32}	K32	structural stiffness coefficient of strut in the longitudinal direction, strut fully extended	lb/in.

THEORY	FORTRAN		UNIT
K_{33}	K33	change in stiffness coefficient of strut in the longitudinal direction per inch of vertical strut movement	$\dfrac{\text{lb/in.}}{\text{in.}}$
K_4	K4	lateral deflection of strut due to a unit vertical load	in./lb
L_{FORK}	FORKL	distance from fork junction to cg of unsprung mass	in.
m	N4	total number of airplane degrees of freedom, including flexible modes	
n_1	N1	polytropic exponent for strut airload before the rebound chamber is full	
n_2	N2	polytropic exponent for strut airload after the rebound chamber is full	
P_A	PA	airload induced in the strut	lb
P_E	PE	airload in strut when fully extended	lb
P_F	PF	vertical friction load induced in the strut	lb
	PINPOS	distance from strut orifice center to end of metering pin when strut is fully extended; negative if pin protrudes through the orifice	in.
P_O	PO	oil load induced in the strut	lb
P_r		tire pressure	psi
P_S	PS	lateral force acting on the tire, + outboard	lb

THEORY	FORTRAN		UNIT
P_T	PT	vertical force acting on the tire	lb
P_{TB}	PTB	tire bottoming load	lb
P_{ult}	PULT	ultimate load-carrying capability of ground	lb
Q	HATF	airplane motion, both rigid and flexible	in., sec
q	HATF	flexible motion of the airplane	in., sec
Q_o	QO	hydraulic fluid orifice coefficient, for rebound chamber orifices	
Q_M	QM	generalized masses of airplane flexible modes	$\dfrac{lb\text{-}sec^2}{in.}$
$\{R\}$	HATF	rigid body airplane motion	
R_{PTB}	RPTB	value used in calculating drag load at time of tire bottoming	
R_S	R_S	radius from strut center line to spline bearing surface	in.
R_T	RT	radius of undeflected tire	in.
S	S	motion of the strut stroke	in., sec
S_N	SN	maximum strut stroke	in.
$[SQ]$		matrix of coefficients for calculating airplane accelerations from airplane modal displacements	$1/sec^2$
SR	SR	slip ratio	
S_{TDF}	STDF	flexible motion of the gear attach point	in., sec

THEORY	FORTRAN		UNIT
S_W	SW	wing planform area	ft^2
T	THRUST	airplane thrust	lb
t	TIME	time	sec
TA_j	TA	coefficients for calculating pitching motion at the gear attach point from airplane accelerations	
T_β	TBETA	reaction twisting torque in the strut	lb-in.
TF_j	TF	coefficients for calculating longitudinal motion at the gear attach point from airplane accelerations	
TH_j	TH	coefficients for calculating vertical motion at the gear attach point from airplane accelerations	
TT_j	TT	coefficients for calculating rolling motion at the gear attach point from airplane accelerations	
U_{CG}	UCG	displacement of airplane cg parallel to the runway	in.
U_{CGO}	UCGO	location of cg down the runway at t = 0	in.
V_D	VD	drag constant used before tire bottoming for flexible ground	
V_E	VE	engaging speed, relative velocity between airplane and runway, measured parallel to the runway	fps

103

THEORY	FORTRAN		UNIT
V_{EA}	VEA	volume in strut air chamber when strut is fully extended	in.^{3}
V_0	V0	velocity of the flow of hydraulic fluid through the strut orifice	in./sec
V_W	VW	wind velocity, measured parallel to the runway; + headwind	fps
V_Y	VY	forward velocity of the airplane relative to the air, measured parallel to the runway	fps
V_Z	VZ	vertical velocity of the airplane, measured perpendicular to the runway	fps
W	W	airplane weight	lb
WL	WL	load factor, initial airplane acceleration = (1-WL) g	
W_U	WU	weight of unsprung mass	lb
X	X	lateral distance from airplane cg to gear attach point, measured in airplane body axis system	in.
X_A	XA	lateral distance from gear attach point to cg of unsprung mass, measured in airplane body axis system	in.
X_N	XN	cornering power, parameter used in tire side force calculations	lb
X_T	XT	total distance wheel has traveled parallel to the runway after initial contact	in.

THEORY	FORTRAN		UNIT
Y	Y	longitudinal distance from gear attach point to airplane cg, measured in airplane body axis system	in.
Y_A	YA	longitudinal distance from gear attach point to cg of unsprung mass, measured in airplane body axis system	in.
Y_{AC}	YAC	longitudinal location of the airplane aerodynamic center	in.
Y_{CG}	YCG	longitudinal location of the airplane cg	in.
Y_{EM}	YEM	longitudinal location of thrust action point	in.
Z	Z	vertical distance from gear attach point to airplane cg, measured in airplane body axis system	in.
Z_{AC}	ZAC	vertical location of airplane aerodynamic center	in.
Z_{CG}	ZCG	vertical location of airplane cg	in.
Z_{EM}	ZEM	vertical location of thrust action point	in.
Z_G	ZG	vertical height of ground directly beneath axle	in.
a	ALPHA	airplane angle of attack	deg
β	BETA	twist angle of strut, in a plane perpendicular to strut center line	rad, sec
δ_s	DEL,ANGS	angle of strut side bending	rad

THEORY	FORTRAN		UNIT
θ	THETA	roll motion of the airplane cg in airplane body axis system	rad, sec
μ_{B_1}	SLMU	coefficient of bearing friction at the upper bearing	
μ_{B_2}	SLMU	coefficient of bearing friction at the lower bearing	
μ	MUBAR	tire coefficient of sliding friction in the longitudinal direction	
μ_β	SLBMU	coefficient of bearing friction at the strut splines	
μ_ψ	PSIMU	tire coefficient of sliding friction in the lateral direction	
ρ	RHO	density of strut hydraulic fluid	$\dfrac{lb/sec^2}{in.^4}$
σ	SIGMA	roll angle the strut center line makes with the vertical axis of the airplane body axis system, + outboard	rad
ϕ	PHI	pitch angle the strut center line makes with the vertical axis of the airplane body axis system, + forward	rad
ψ_s	PSIS	tire yaw angle	rad
ω	OMEGA	wheel rotation about the wheel axle	rad, sec
ω_0	OMEGAO	wheel rotating rate about the wheel axle at time = 0.0	$\dfrac{1}{sec}$

LIST OF TABLES

BTAB	table of spline bearing friction coefficients versus strut stroke
CDTAB	table of oleo orifice coefficients of discharge versus a rate of fluid flow measured in in.^{2}/sec; argument used in this program is (V_o) (A_{nn})
CORTAB	table of tire turning power versus tire deflection
CTTAB	table of tire load versus tire deflection
GRTAB	table of ground deflection and tire deflection plus ground deflection versus ground load
LOWTAB	table of lower bearing friction coefficients versus strut stroke
QOTAB	table of rebound chamber orifice coefficients of discharge versus strut stroke
SLIP	table of ground sliding coefficients of friction versus slip ratio
UPTAB	table of upper bearing friction coefficients versus strut stroke
XYTABL	table of ground height versus distance down the runway

UNSPRUNG MASS EQUATIONS OF MOTION

Assumptions

1. No elastic rotation of the strut in the pitch direction

2. No nonlinear accelerations induced by wheel rotation

3. No elastic rotation of the strut in the roll direction

A. Before tire touches ground

$$\ddot{a} = \cos\sigma\,[\Sigma_1\cos\phi + \Sigma_2\sin\phi]$$

$$\ddot{b} = \Sigma_1\cos\phi\sin\sigma + \cos\phi\,(Z_A\cos\sigma - X_A\sin\sigma)\Sigma_3$$

$$\ddot{d} = [-\Sigma_1\sin\phi + \Sigma_2\cos\phi - (Y_A\sin\phi - Z_A\cos\phi)\Sigma_4]\cos\sigma$$

$$\ddot{\beta} = \frac{T_\beta + F_D\,E_B - F_B\,E_D}{I_\beta}$$

$$\ddot{S} = 0.0$$

$$\ddot{\bar{b}} = 0.0$$

$$\ddot{\bar{d}} = 0.0$$

$$\ddot{\omega} = 0.0$$

B. After tire touches ground

$$\ddot{a} = \cos\sigma[\Sigma_1\cos\phi + \Sigma_2\sin\phi] \quad \text{(before strut moves)}$$

$$= \Big[(W_u - P_T)\cos(\phi + A)\cos\sigma + F_A - (\mu P_T + P_S\sin\beta)\sin(\phi + A)\cos\sigma$$

$$-(\sin\sigma + \theta\cos\sigma\cos\phi)\cos\beta\,P_S + F_E\sin F\Big] \div \frac{W_u}{g} \quad \text{(after strut moves)}$$

$$
\begin{Bmatrix} \ddot{\beta} \\ \ddot{d} \\ \ddot{b} \end{Bmatrix}
=
\begin{bmatrix}
C_{11} & C_{12} & C_{13} \\
C_{21} & C_{22} & 0.0 \\
C_{31} & C_{32} & C_{33}
\end{bmatrix}^{-1}
\begin{Bmatrix} f_1 \\ f_2 \\ f_3 \end{Bmatrix}
$$

108

where

$$C_{11} = I_\beta$$

$$C_{12} = \left[(E_b + \bar{b}) \cos \beta - (E_d + \bar{d}) \sin \beta\right] \frac{W_u}{g}$$

$$C_{21} = C_{12}$$

$$C_{13} = -\left[(E_d + \bar{d}) \cos \beta + (E_b + \bar{b}) \sin \beta\right] \frac{W_u}{g}$$

$$C_{31} = C_{13}$$

$$C_{22} = \frac{W_u}{g}$$

$$C_{33} = \frac{W_u}{g}$$

$$f_1 = (E_b + \bar{b} + E_x) F_x - (E_d + \bar{d}) F_y + T_\beta$$

$$f_2 = F_x + F_D$$

$$f_3 = F_y + F_B$$

$$\ddot{S} = -\ddot{a} + \cos \sigma \left[\Sigma_1 \cos \phi + \Sigma_2 \sin \phi\right]$$

$$\ddot{b} = \ddot{b} - \Sigma_1 \cos \phi \sin$$

$$\ddot{d} = \ddot{d} + \cos \sigma \left[\Sigma_1 \sin \phi - \Sigma_2 \cos \phi - (E_L - S) \Sigma_4\right]$$

$$\ddot{\omega} = \frac{(\mu P_T - \Gamma_S \sin \beta)(R_T - C_T)}{E_R I_R}$$

where Σ_1, Σ_2, Σ_3, and Σ_4 are the vertical, fore and aft, roll, and pitch accelerations of the airplane at the strut attach point respectively.

GROUND FORCES

Assumptions

Small airplane roll attitude

$$F_x = -(\mu P_T + P_S \sin \beta) \cos (\phi + A) + P_T \sin (\phi + A)$$

$$F_y = -(\mu P_T + P_S \sin \beta)(\sin \sigma \sin (\phi + A) + \theta \sin \sigma \cos \sigma)$$
$$+ P_S \cos \sigma \cos \beta - P_T (\cos (\phi + A) \sin \sigma + \theta \cos A \cos \sigma)$$

$$F_z = (W_u - P_T) \cos (\phi + A) \cos \sigma - (\mu P_T + P_S \sin \beta) \sin (\phi + A) \cos \sigma$$
$$- P_S \cos \beta (\sin \sigma + \theta \cos \sigma \cos \phi)$$

TIRE FORCES

Assumptions

1. No restoring torque in tire

2. No bearing friction in wheel assembly

3. No tire inertia effects

4. No tire hysteresis effects

5. Centrifugal forces have no effect on tire vertical deflection

6. Constant side coefficient of friction

A. Tire deflection

$$C_T = R_T \cos \sigma - D + Z_G$$

$$D = D_{CG} - (Z_D \cos \theta + X_D \sin \theta) \cos A + Y_D \sin A + G_\delta$$

$$Z_D = Z + (E_L - S) \cos \phi \cos \sigma - \{\overline{d} + E_D \cos \beta + (E_B + E_X) \sin \beta\} \sin \phi$$
$$+ L_{FORK} \cos (F - \phi) + e \sin (F - \phi) + S_{TDF} - \delta_S E_B \cos \phi$$

$$X_D = X + (E_L - S) \cos \phi \sin \sigma + \{\overline{b} - E_D \sin \beta + (E_B + E_X) \cos \beta\} \cos \sigma$$
$$- E_D \delta_S \cos \phi \sin \sigma$$

110

$$Y_D = Y + (E_L - S) \sin \phi \cos \sigma + \left\{ \bar{d} + E_D \cos \beta + (E_B + E_X) \sin \beta \right\} \cos \phi$$

$$+ e \cos (F - \phi) - \delta_s E_B \sin \phi \cos \sigma$$

$$\ddot{G}_\delta = \frac{P_T - C_G \left[\dot{G}_\delta + \dfrac{12 \, V_E \, G_\delta}{XX1} \right] - XX1}{G_M}$$

$$XX1 = \sqrt{R_T^2 - (R_T - C_T - G_\delta)^2}$$

$$S_{TDF} = \sum_{j=5}^{m} TH_j \, Q_j$$

B. Slip ratio

$$SR = \left[12 \, V_E - \frac{R_T - C_T}{E_R} \, \dot{\omega} + \dot{\bar{d}} \cos (\sigma + \theta) \cos (\phi + A) \right.$$

$$\left. + \dot{A} \left(E_L - S + R_T - \frac{C_T}{E_R} \right) \cos \sigma + E_B \, \dot{\beta} \cos (\sigma + \theta) \cos (\phi + A) \right]$$

$$\div \left[12 \, V_E - R_T \, \dot{\omega}_o \right]$$

C. Vertical and drag forces

1. Smooth rigid ground

F_T = linear interpolation of CTTAB table using C_T (tire deflection) as argument

$XX2$ = 0.0

2. Flexible ground

F_T = linear interpolation of GRTAB table using C_T (tire deflection) as argument and determining ground load

D_{EL} = linear interpolation of GRTAB table using C_T (tire deflection) as argument and determining ground plus tire deflection

111

$$XX2 = \frac{D_C D_{EL}}{R_T}$$

Equation for calculating ground load-deflection

$$\delta_G = \frac{\log\left(\dfrac{P_{ult}}{P_{ult} - F_{KZ1}}\right)}{C_{DEL}}$$

F_{KZ1} = value of tire load from CTTAB table

3. Rough terrain (see Figure 47)

$$\delta_i = R_T - \sqrt{(U_K - X_i)^2 + (D_K - Y_i)^2} \qquad \text{where } i = 1 \ldots 5$$

$$D_{EFL} = \delta_i \theta_o/5$$

F_i = linear interpolation of CTTAB table using D_{EFL} as argument

$$F_T = \sum_{i=1}^{5} F_i \cos \gamma_i$$

$$XX2 = -\sum_{i=1}^{5} F_i \sin \gamma_i$$

4. P_T and μP_T

$$P_T = F_T \cos \epsilon - P_D \sin \epsilon$$

$$\mu P_T = F_T \sin \epsilon + P_D \cos \epsilon$$

$$P_D = \mu F_T + XX2 + D_{RAG}$$

$$D_{RAG} = V_D G_\delta \sqrt{F_T} \qquad \text{if} \quad P_{TB} \geqslant F_T$$

$$= V_D R_{PTB} + (F_T - P_{TB}) G_\delta D_{BTM} \qquad \text{if} \quad P_{TB} < F_T$$

112

D. Lateral force

$$P_S = \left[SR \frac{\psi_s}{|\psi_s|} + \left(\Phi - .14815 \, \Phi^3\right)(1 - SR) \right] \mu_\psi \, P_T \left(1 - e^{-BX_T}\right)$$

$$\psi_s = \tan^{-1}\left[\frac{-\dot{b} - (R_T - C_T) \, \dot{\delta}_s}{|12 \, V_E + \dot{d}|} \right] - \beta$$

$$\eta = \frac{X_N \, \psi_s}{\mu_\psi \, P_T}$$

$$\Phi = 1.5 \quad \text{for} \quad |\eta| \geqslant 1.5$$

$$= \eta \quad \text{otherwise}$$

$$X_N = \text{linear interpolation of CORTAB table using } C_T \text{ (tire deflection) as argument}$$

$$B = \left[SR \, |\sin \psi_s| + (1 - SR) \frac{\psi_s}{1.57} \right] \frac{B_W}{\mu_\psi \, P_T}$$

$$X_T = \frac{\sqrt{[\bar{b} + (R_T - C_T) \, \delta_s]^2 + [\bar{d} + U_{CG} - U_{CGO}]^2}}{12}$$

STRUT INTERNAL FORCES

Assumptions

1. Incompressible oil flow through one orifice

2. Constant torsional stiffness

3. Air compression in strut obeys general form of equation of state, $PV^n = \text{const}$

4. No damping of side bending moment

5. Sea level atmospheric pressure

113

A.   Vertical force

$$F_A = P_A + P_O + P_F$$

$$P_O = \frac{\rho (A_1 - A_p)^3 \dot{S} | \dot{S} |}{2 C_D^2 (A_O - A_p)^2}$$

$$C_D = \text{interpolation of CDTAB table using } V_O A_{nn} \text{ as argument}$$

$$V_O = \frac{A_1 S}{A_O - A_p}$$

$$A_{nn} = \frac{\sqrt{\dfrac{A_O}{\pi}} - \sqrt{\dfrac{A_p}{\pi}}}{2}$$

1.   No rebound chamber

$$P_A = (P_E + 14.7 A_{POD}) \frac{V_{EA}}{(V_{EA} - S A_{POD})^{n_1}} - 14.7 A_{POD}$$

2.   Rebound chamber

$$P_A = \left[\frac{P_E + 14.7 A_{POD}}{(1 + C_X)^n} - 14.7 A_{POD} \right] C_K$$

a.   Rebound chamber not filled with oil $E_Q \leqslant A_R S$

$$n = n_1$$

$$C_K = \frac{A_{SPL}}{A_{POD}}$$

114

$$C_X = \frac{(A_{SPL}\,S - E_Q)}{V_{EA}} + \frac{C_{EXP}\,(P_A - P_E)}{V_{EA}\,A_{POD}}$$

$$E_Q = A_S \sqrt{\frac{2}{\rho\,A_{SPL}}} \int_o^t Q_o \sqrt{P_A}\; dt \quad \text{(volume of oil in rebound chamber)}$$

$$Q_o = \text{interpolation of QOTAB table using S (stroke) as the argument}$$

b. Rebound chamber filled $E_Q > A_R S$

$$n = n_2$$

$$C_K = 1.0$$

$$C_X = \frac{(A_{SPL} - A_R)\,S + C_{EXP}\dfrac{P_A - P_E}{A_{POD}}}{V_{EA}}$$

$$P_F = \mu_{B1}\,F_{1TOT} + \mu_{B2}\,F_{2TOT} + \mu_{\beta}\,F_{TORQ}$$

$$F_{1TOT} = \sqrt{F_1{}^2 + F_{1S}{}^2}$$

$$F_1 = \Big[F_D\,(A_{BRG} - S) + L_{FORK}\,F_E + e\,(F_{AXD}\sin F - F_{AXS}\cos F)$$
$$- F_A\,(E_D \cos \beta + E_B \sin \beta + \bar{d})\Big] \div \Big[B_{BRG} + S\Big]$$

$$F_{1S} = \Big[F_B\,(A_{BRG} - S) + F_L \cos \beta - F_A\,(\bar{b} - E_D \sin \beta)\Big] \div \Big[B_{BRG} + S\Big]$$

$$F_{AXD} = F_D \cos \beta - F_B \sin \beta + \frac{T_\beta}{E_B}$$

$$F_{AXS} = F_D \sin \beta + F_B \cos \beta - \frac{T_\beta}{E_B}$$

$$F_{2TOT} = \sqrt{F_2{}^2 + F_{2S}{}^2}$$

115

$$F_2 = F_1 + F_D$$

$$F_{2S} = F_{1S} + F_B$$

$$F_{TORQ} = \frac{T_\beta}{R_S}$$

μ_{B1} = interpolation of UPTAB table using S as argument

μ_{B2} = interpolation of LOWTAB table using S as argument

μ_β = interpolation of BTAB table using S as argument

B. Drag force

$$F_D = -(\bar{d} - D_{FA} - E_X \beta)(K_{32} + S K_{33}) - \bar{C}(\dot{d} - E_X \dot{\beta})$$

$$D_{FA} = F_A K_1 (E_D - L_{FORK} \sin F + e \cos F)$$

C. Side force

$$F_B = -(\bar{b} + K_4 F_A)(K_{22} + S K_{23}) - C_S \dot{b}$$

D. Torsional moment

$$T_\beta = -K_\beta \beta - C_\beta \dot{\beta}$$

E. Force in fork

$$F_E = -(K_E + S D_{AMP}) e - C_F \dot{e}$$

AIRPLANE EQUATIONS OF MOTION (see Figure 48)

Assumptions

1. No airplane yaw

2. No airplane lateral motion

3. Maximum number of flexible modes is 10

4. Modal accelerations due to gravity and modal accelerations due to aerodynamic forces are neglected

$$\{\ddot{Q}\} = \begin{bmatrix} \{\ddot{R}\} \\ \overline{} \\ \{\ddot{q}\} \end{bmatrix} = \begin{bmatrix} \begin{Bmatrix} \ddot{h} \\ \ddot{A} \\ \ddot{\theta} \\ \ddot{f} \end{Bmatrix} \\ \overline{} \\ \{\ddot{q}\} \end{bmatrix}$$

All motions are in airplane body axis system

h   =   Rigid body vertical motion

A   =   Rigid body pitch

θ =   Rigid body roll

f   =   Rigid body longitudinal motion

q   =   Flexible modes of airplane

$$\{\ddot{R}\} = [AT]\{F\} + [AM]\{AIR\} + \begin{Bmatrix} g \cos A \\ 0 \\ 0 \\ g \sin A \end{Bmatrix}$$

$$\{\ddot{q}\} = [DQ]\{\dot{q}\} + [SQ]\{q\} + [QT]\{F\}$$

117

Gear forces

$$\{F\} = \begin{Bmatrix} F_h \\ F_a \\ F_\theta \\ F_f \end{Bmatrix}$$

$$F_h = -F_A \cos\sigma \cos\phi + F_D \cos\sigma \sin\phi + F_B \sin\sigma \cos\phi$$

$$F_a = -F_D \cos\sigma \, (E_L - S)$$

$$F_\theta = -F_B \, (E_L - S)$$

$$F_f = -F_A \cos\sigma \sin\phi - F_D \cos\sigma \cos\phi + F_B \sin\sigma \sin\phi$$

Aerodynamic forces

Assumptions

1. Variable airspeed

2. No yaw or lateral motion

3. Sea level altitude

4. Steady air flow

5. C_{L_q}, C_{L_a} and $C_{M_{\dot{a}}}$ are zero

$$\{AIR\} = \begin{Bmatrix} AIR_h \\ AIR_a \\ AIR_\theta \\ AIR_f \end{Bmatrix}$$

$$AIR_h = -A_L \cos a - A_D \sin a - T \sin \Omega_T$$

$$AIR_a = A_a + A_L \overline{Y}_{AC} - A_D \overline{Z}_{AC} + T (\overline{Y}_{EM} \sin \Omega_T + \overline{Z}_{EM} \cos \Omega_T)$$

$$AIR_\theta = Z_z \ C \ C_{MR} \ \dot{\theta}$$

$$AIR_f = A_L \sin a - A_D \cos a + T \cos \Omega_T$$

$$A_L = Z_z \left(C_{L_B} + C_{L_{iH}} i_H + C_{L_{\delta E}} \delta_E \right)$$

$$A_a = Z_z \ C \left(C_{M_B} + C_{M_{iH}} i_H + C_{M_{\delta E}} \delta_E + \frac{C_{M_q} \dot{A} \ C}{24.0 \ V_E} \right)$$

$$A_D = Z_z \left(C_{D_B} + C_{D_{iH}} |i_H| + C_{D_{\delta E}} |\delta_E| \right)$$

$$Z_z = \frac{S_W}{842} \left[V_Z^2 + (V_E + V_W)^2 \right]$$

$$a = A + \gamma$$

$$\gamma = \tan^{-1} \left(\frac{V_Z}{V_Y} \right)$$

$$\overline{Y}_{AC} = Y_{CG} - Y_{AC}$$

$$\overline{Z}_{AC} = Z_{CG} - Z_{AC}$$

$$\overline{Y}_{EM} = Y_{CG} - Y_{EM}$$
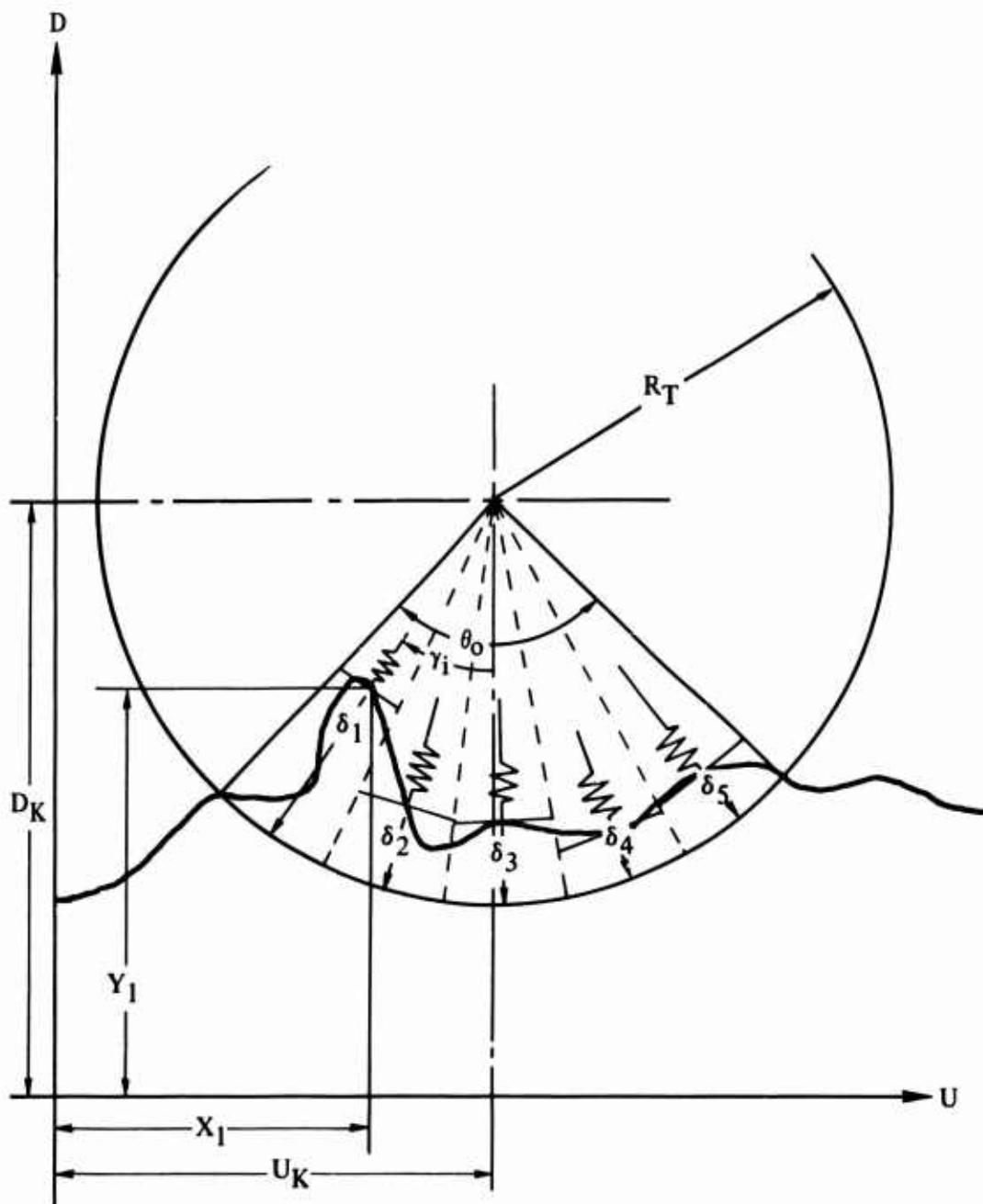
$$\overline{Z}_{EM} = Z_{CG} - Z_{EM}$$

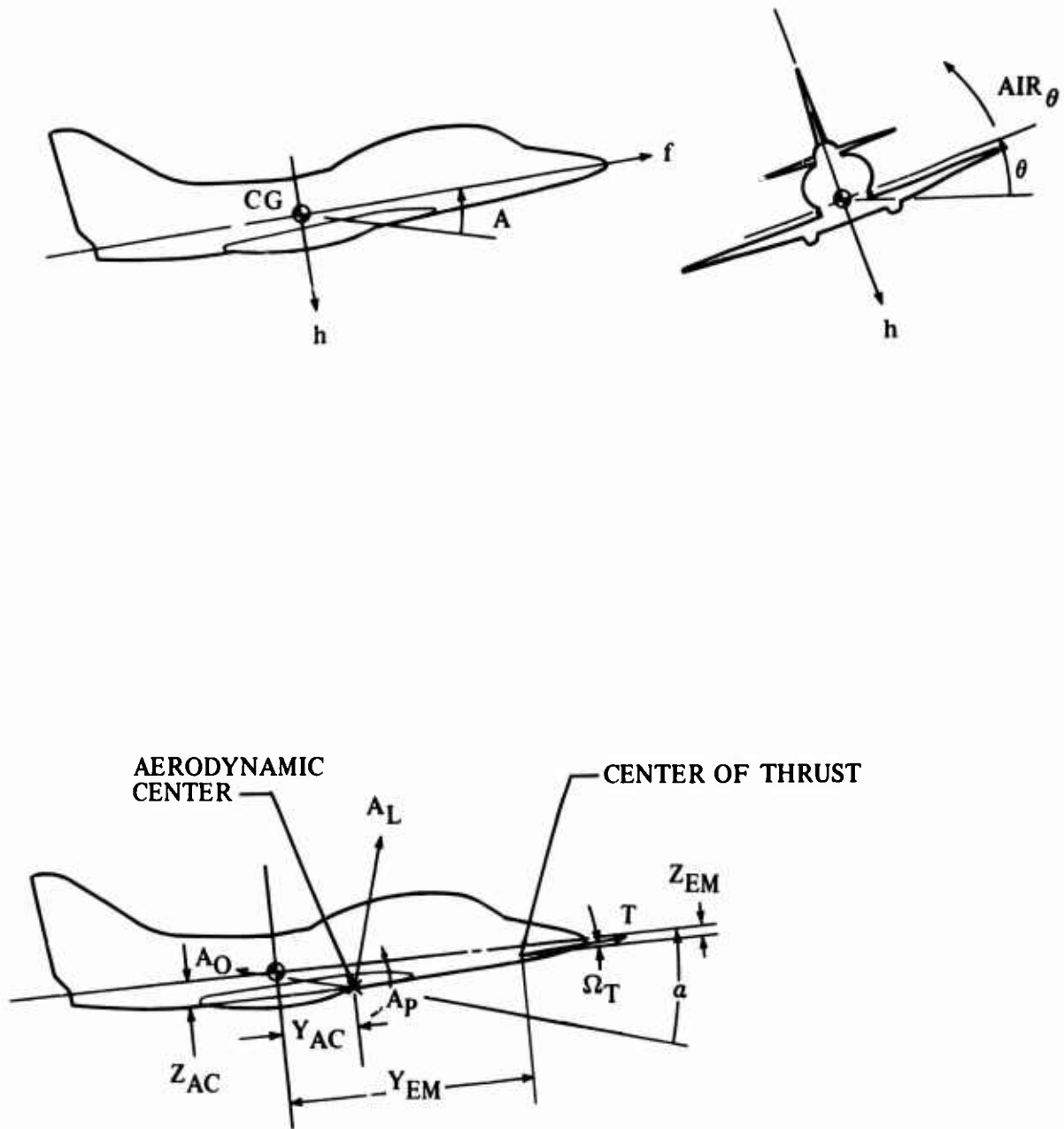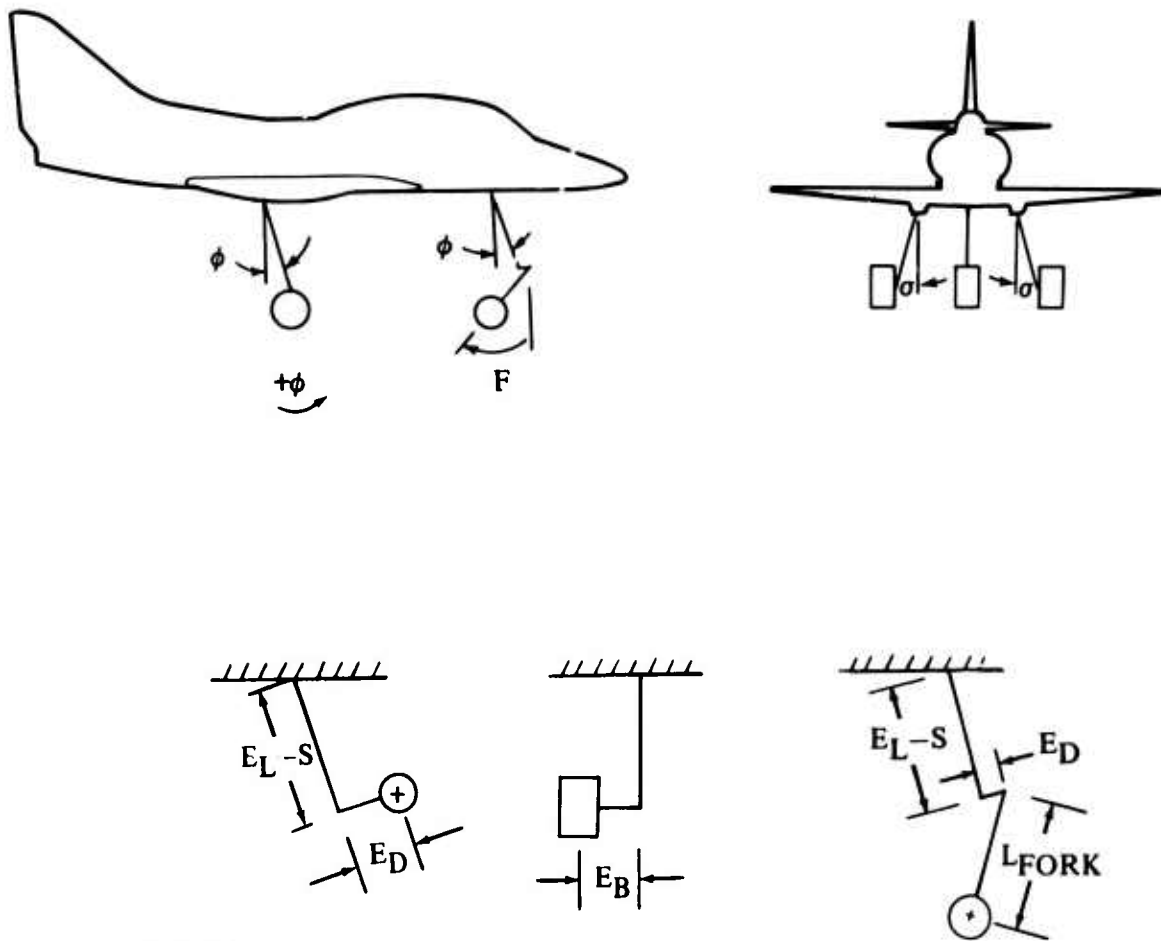Figure 47. Geometry for Rough-Terrain Tire.

120

Figure 48.   Sign Convention for Equations of Motion.

121

POSITIVE DIRECTION OF PARAMETERS IS ILLUSTRATED IN SKETCHES.

E_D + FORWARD

E_B + OUTBOARD

Figure 48. Continued.

122

POSITIVE DIRECTION OF PARAMETERS
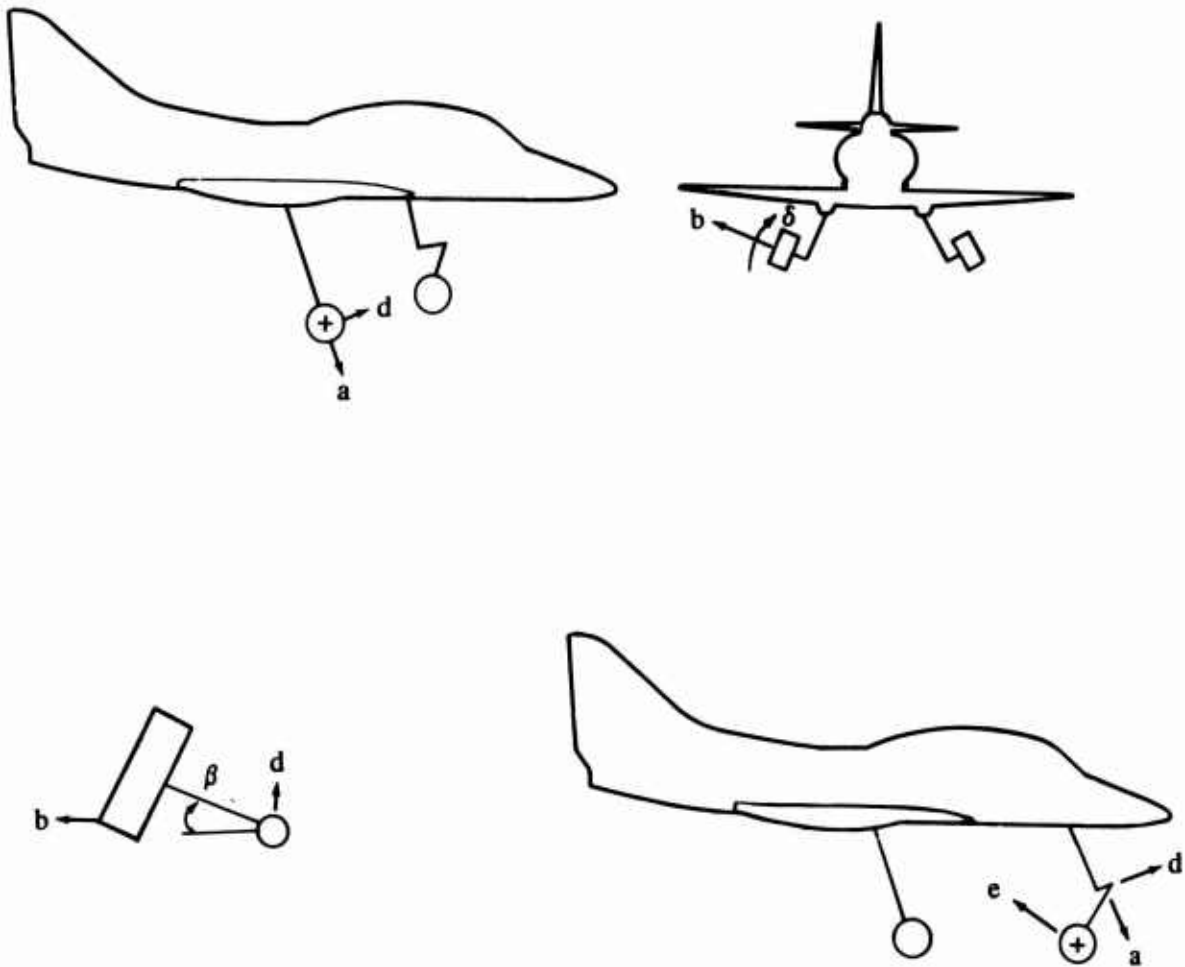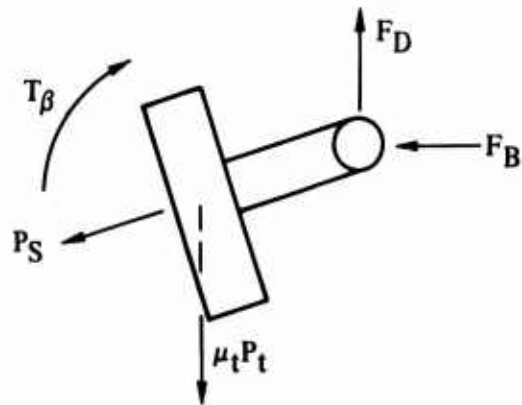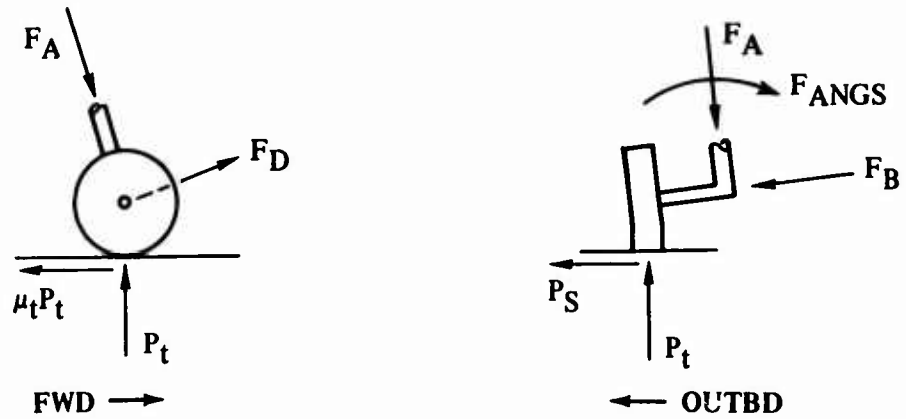IS ILLUSTRATED IN SKETCHES

Figure 48.   Continued.

MAIN GEAR
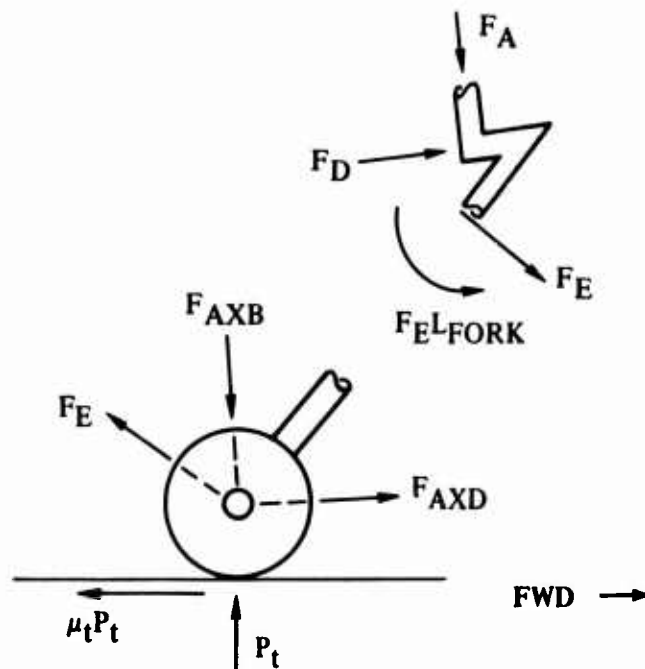

FWD →

← OUTBD

NOSE GEAR

FWD →

Figure 48. Continued.

POSITIVE DIRECTION OF PARAMETERS
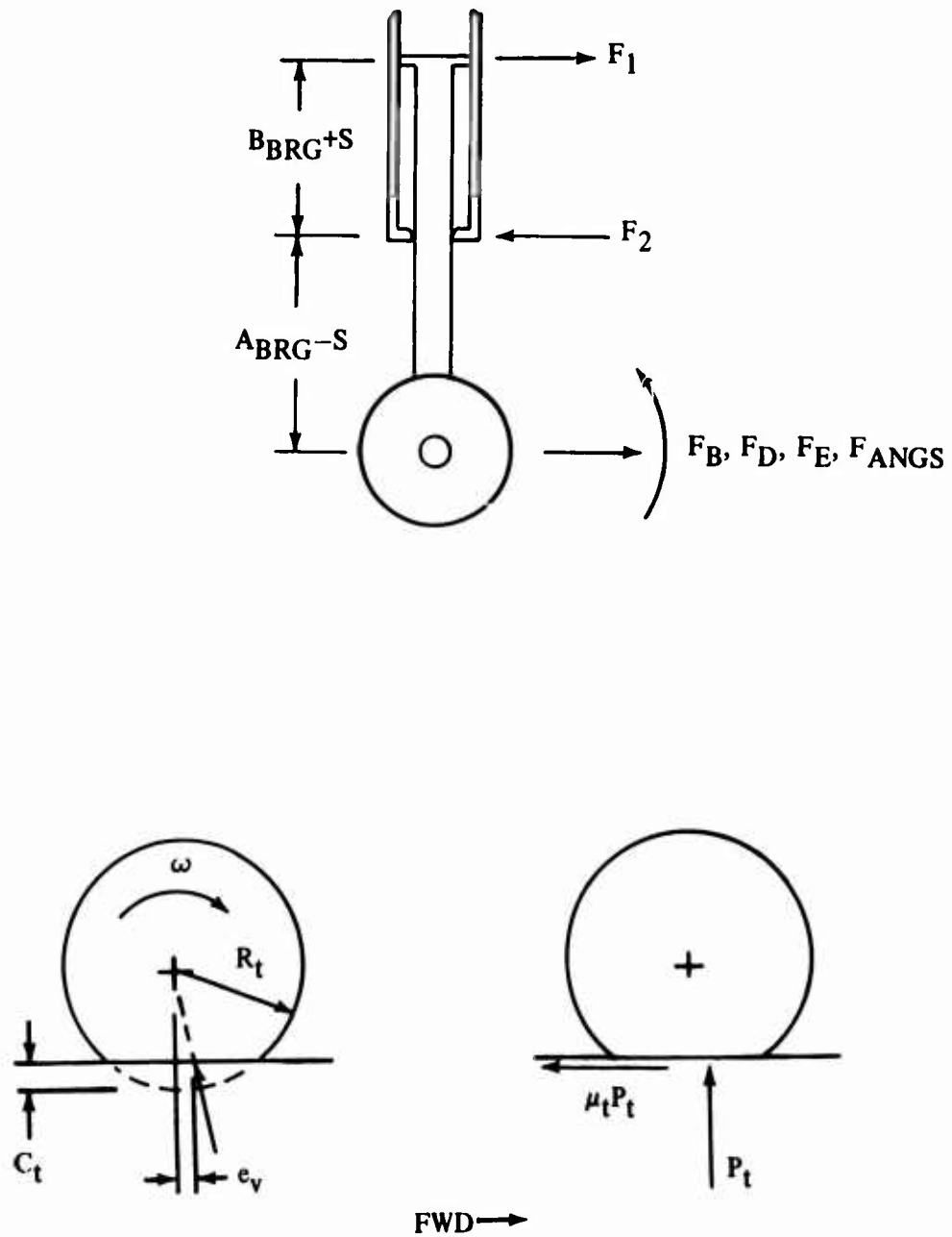IS ILLUSTRATED IN SKETCHES.

Figure 48. Concluded.

APPENDIX II
TEST REPORT
ON
POWER SPECTRAL DENSITY COMPARISONS OF TWO UNIMPROVED DIRT SURFACE RUNWAYS SELECTED BY THE ARMY FOR USE IN A DYNAMIC TAXI ANALYSIS PROGRAM

PURPOSE

The purposes of the report are to present the power spectral density (PSD) characteristics of two unimproved dirt runways and to compare these characteristics with available Air Force data on selected types of airfields. The two unimproved dirt runways are located at Franklin, Virginia (run number 05), and Camp Pickett, Virginia (run number 1A).

FACTUAL DATA

1. The United States Army Aviation Materiel Laboratories (USAAVLABS), Fort Eustis, Virginia, is jointly conducting dynamic taxi tests with the McDonnell-Douglas Corporation, Douglas Aircraft Company. An instrumented YOV-1A Mohawk is being used as the test aircraft. Six unimproved dirt fields were established as test sites.

2. Profile elevation data were gathered from the selected unimproved runways by USAAVLABS using a profilometer that sampled surface elevations every 1/2 foot. The length of each line of survey was 500 feet.

3. The data were to be used as a runway forcing function in a dynamic taxi analysis program. Results obtained theoretically are to be correlated with those results obtained from taxi tests on unimproved runway surfaces.

4. The U.S. Army Aviation Materiel Laboratories requested AF Flight Dynamics Laboratory (FDDS) to reduce the profile data gathered into profile and power spectral density curves. This request resulted from an initial request by Douglas Aircraft Company to have the data reduced into the same PSD form that the Air Force uses for similar programs.

126

FDDS DATA REDUCTION PROGRAM

Profile data have been reduced to power spectral density for the center line of two of the six sites from which profile data were gathered. The profile data were reduced to PSD form with a 7044-7094 direct coupled digital computer using a previously established program based on equations presented in Reference 7. Data conditioning (jumps due to setups, bad data points, etc.) is included in the program. This method incorporated the removal of the linear trend. To obtain a profile curve relative to a zero reference, the value of the first data point has been subtracted from each data point.

RESULTS

A comparison (Figure 49) of the PSD for the Franklin, Virginia, and Camp Pickett, Virginia, sites with the PSD for a multi-matted surface runway (curves obtained from Reference 8) shows that the power levels for both sites are above the multi-matted runway power level for all reduced frequencies.

The Franklin site has power factors ranging between 1.5 times and 3 times the power level of the multi-matted surface for a wavelength of 3.5 feet to 18 feet. This wavelength range was determined to be most important for the YOV-1A airplane. The Camp Pickett site has a power factor which is about 6 times the power level of the Franklin site for a wavelength range of 3.5 feet to 18 feet.

A comparison of the PSD of the above two sites was made with current Air Force unimproved airfield PSD data. The results show that both the Franklin and Camp Pickett, Virginia, sites are generally within the power band levels of the current Air Force data.
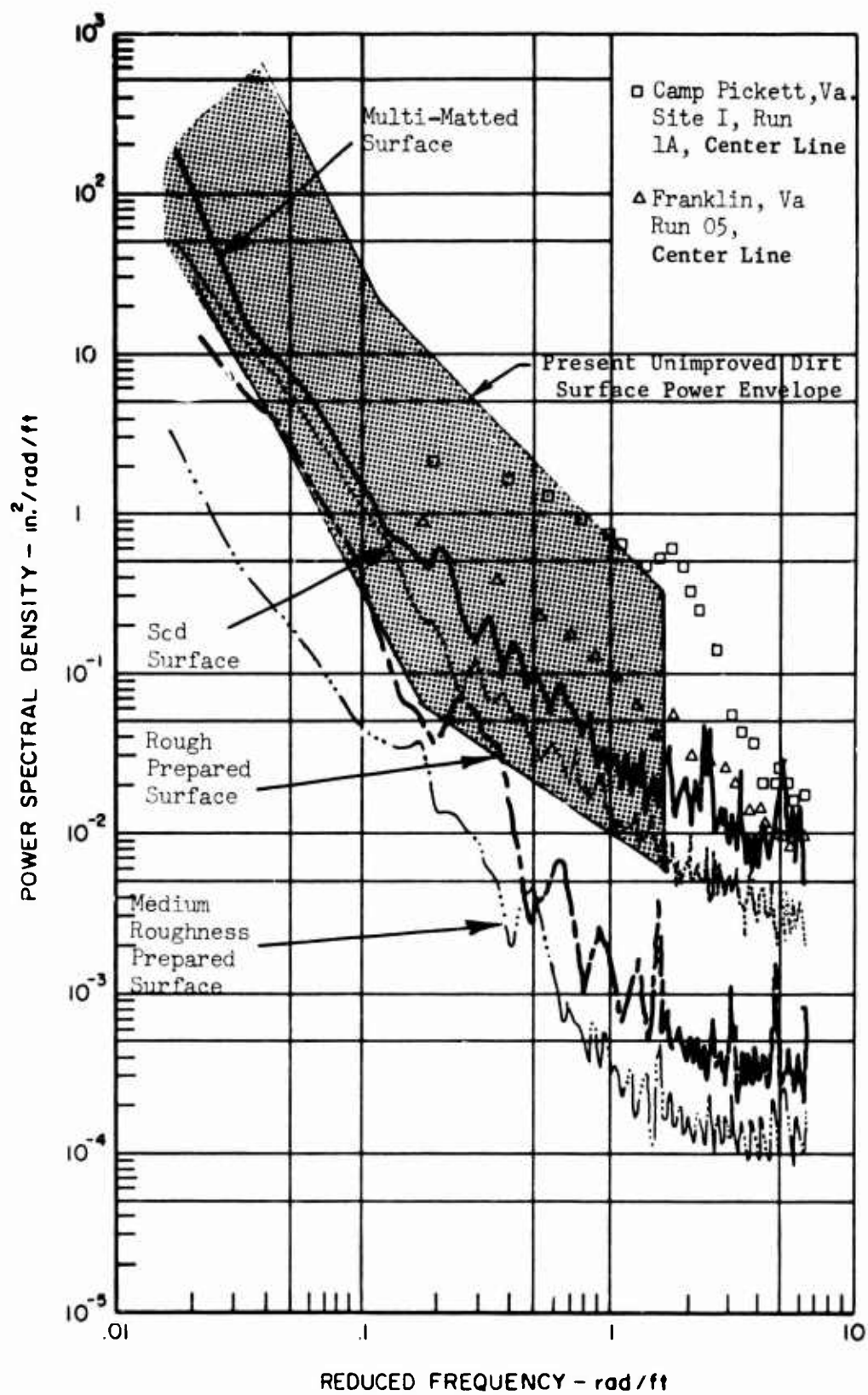
127

Figure 49. Landing Surface Power Spectral Density Comparisons.

APPENDIX III
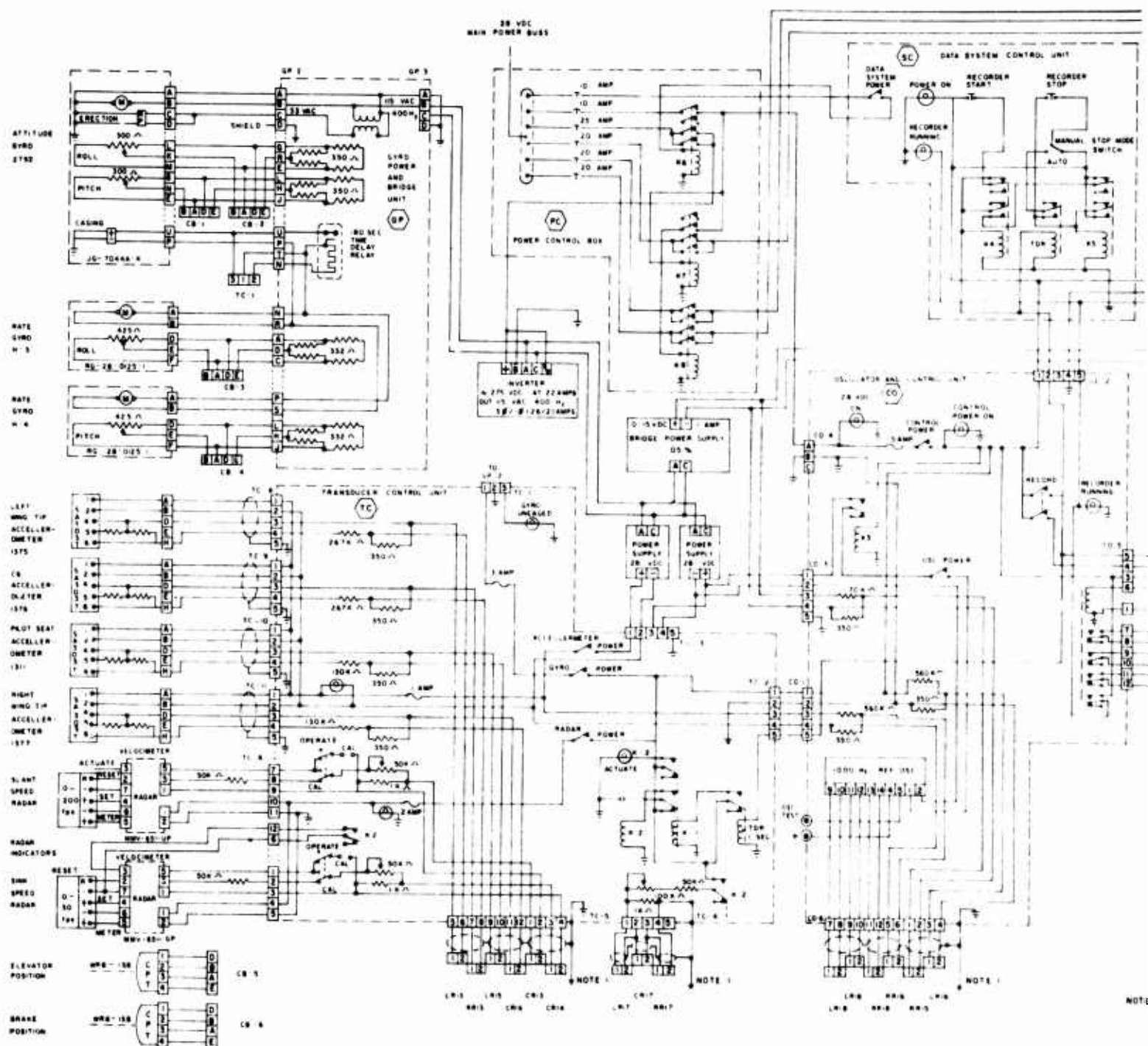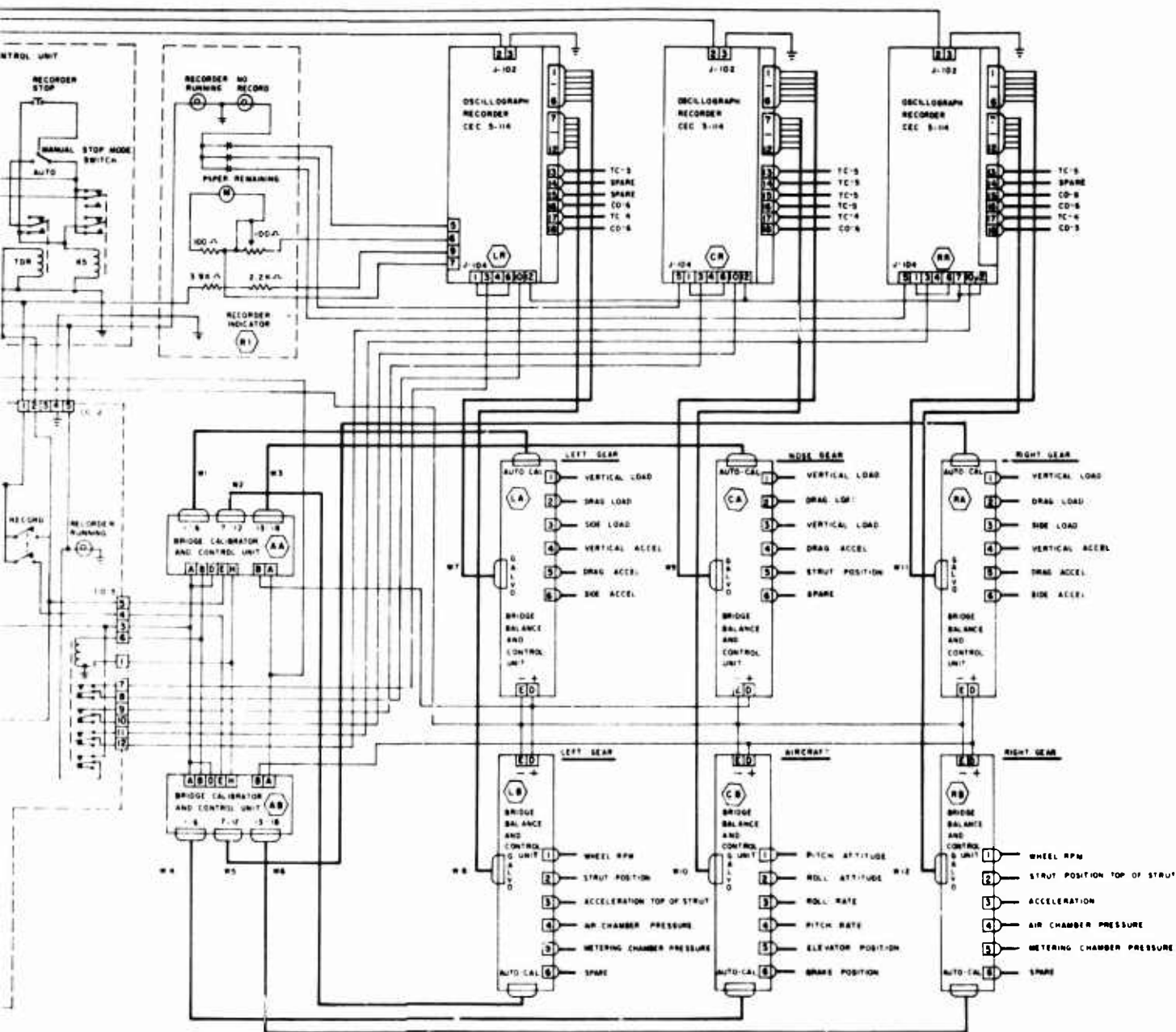## SCHEMATIC OF INSTRUMENTATION CIRCUITRY

Figure 50.   Schematic of Instrumentation Circuitry.

YOV-1 LANDING LOADS DATA SYSTEM
1966-1967

NOTE I   TO PIN 3 OF EACH CONNECTOR

129-B

APPENDIX IV
RADAR VELOCIMETER OPERATIONAL THEORY

The radar velocimeter operates on the doppler effect which causes an apparent shift in frequency when the source of oscillation moves with respect to a reflecting surface.

The doppler frequency shift can be calculated from

$$F_D = 2 V_V/\lambda \qquad (15)$$

where F_D = frequency shift, Hz

V_V = vertical velocity, fps

λ = wavelength, ft

Wavelength can be calculated from

$$\lambda = C/F_O \qquad (16)$$

where C = velocity of light

F_O = transmitter frequency

The frequency shift per fps of velocity can be calculated from

$$F_D/V_V = 2/\lambda \qquad (17)$$

The nominal transmitter frequency is 4,382 mHz. Substituting this in equation (17) yields 8.9 Hz/fps.

The radar velocimeter has a frequency to voltage converter that converts the doppler shift frequency to a voltage that is displayed in the cockpit meter as velocity in feet per second. The doppler shift frequency is recorded on the oscillograph recorder as a series of pulses. The frequency of these pulses can be determined by counting the number that occur per unit of time. The velocity can then be calculated by dividing this frequency by the factor obtained from equation (17). For example, if the doppler shift frequency is 89 Hz, the vertical velocity is 89/8.9 or 10 ft/sec.

When the velocimeter is moving toward a perfectly flat surface, the pulses recorded should be evenly spaced if the velocity is constant.

131

However, if the terrain has any roughness, the bumps will be sensed as a change in velocity and the pulses recorded will be unevenly spaced. If the general terrain is level but with some vertical waves, the average descent velocity can be obtained by choosing a long enough interval of time on the oscillograph record to compute the doppler shift frequency.

The accuracy of the velocity determined by data reduction of the oscillograph records is determined by the accuracy of the transmitted frequency and the type of terrain beneath the radar. For a perfectly flat terrain, the accuracy is ±0.25 percent or better. The accuracy over an uneven terrain is degraded somewhat. The amount of degradation is dependent upon the time interval selected to determine the doppler shift frequency and the characteristics of the terrain.

The cockpit meter displays vertical velocity on a 0-500 microampere meter which has a 0-30 fps scale with 0.05 fps increments. The reading accuracy of this meter is 1.5 percent of full scale, or about ±0.5 fps. The electronic accuracy of this reading is determined by the transmitting frequency and the transfer characteristic of the frequency to voltage converter. For a perfectly flat terrain, the accuracy is probably ±5 percent of full scale or better. Over uneven terrain, the accuracy would be degraded by an indeterminate amount, probably less than ±3 percent.

DISTRIBUTION

Director of Defense Research & Engineering	1
Assistant Secretary of the Army (R&D)	1
Assistant Chief of Staff for Force Development, DA	2
Deputy Chief of Staff for Logistics, DA	1
Third United States Army	2
Sixth United States Army	2
United States Army, Pacific	1
Chief of Research & Development, DA	3
Army Materiel Command	3
Army Aviation Systems Command	3
Hq, Army Air Mobility Research & Development Laboratory	2
Ames Directorate, Army Air Mobility R&D Laboratory	2
Eustis Directorate, Army Air Mobility R&D Laboratory	20
Langley Directorate, Army Air Mobility R&D Laboratory	2
Lewis Directorate, Army Air Mobility R&D Laboratory	2
Army Aviation Systems Test Activity	2
Army R&D Group (Europe)	2
Army Scientific & Technical Information Team (Europe)	1
Army Advanced Materiel Concepts Agency	1
Army Aeromedical Research Laboratory	2
Army Land Warfare Laboratory	1
Army Human Engineering Laboratories	2
Army Natick Laboratories	1
Army Ballistic Research Laboratory	1
Army Fuels & Lubricants Laboratory	1
Army Research Office - Durham	1
Army Materials & Mechanics Research Center	5
Army Plastics Technical Evaluation Center	1
Army Engineer Waterways Experiment Station	1
Army Test & Evaluation Command	1
Army Materiel Systems Analysis Agency	1
Army Electronics Command	4
USACDC Aviation Agency	4
USACDC Transportation Agency	1
Army Medical R&D Command	1
Army Weapons Command	1
Picatinny Arsenal	1
Edgewood Arsenal	1
Army Command & General Staff College	1
Army Transportation School	1
Army Aviation School	1
Army Transportation Center & Fort Eustis	4

Army Aviation Test Board	2
Army Arctic Test Center	1
Army Transportation Engineering Agency	1
Army Board for Aviation Accident Research	1
1st Cavalry Division (Airmobile)	1
Army Field Office, AFSC	1
Air Force Office of Scientific Research	1
Hq, USAF	2
Air Force Flight Test Center	1
San Antonio Air Materiel Area	1
Air Force Aero Propulsion Laboratory	1
Air Force Materials Laboratory	3
Air Force Flight Dynamics Laboratory	5
Aeronautical Systems Division, AFSC	3
Air Force Avionics Laboratory	1
Naval Air Systems Command	12
Chief of Naval Research	4
Naval Safety Center	2
Naval Air Rework Facility	1
Naval Air Station, Patuxent River	1
Naval Air Test Center	1
Naval Air Development Center	3
Naval Weapons Laboratory	2
Naval Ordnance Laboratory	1
Naval Ship Research & Development Center	3
Bureau of Medicine & Surgery, DN	1
Commandant of the Marine Corps	1
Marine Corps Liaison Officer, Army Transportation School	1
U.S. Coast Guard	1
Transportation Systems Center	1
NASA Headquarters	1
Ames Research Center, NASA	2
Langley Research Center, NASA	1
Lewis Research Center, NASA	1
Manned Spacecraft Center, NASA	1
Scientific & Technical Information Facility, NASA	2
National Aviation Facilities Experimental Center, FAA	1
Department of Transportation Library	2
Federal Aviation Administration, Jamaica	1
Federal Aviation Administration, Washington	4
Civil Aeromedical Institute, FAA	1
Bureau of Aviation Safety, National Transportation Safety Board	1
Patent Office	1
Government Printing Office	1
Defense Documentation Center	12